Annual Report April 1, 2016 - March 31, 2017

journal or publication title	University of Tsukuba Tandem Accelerator Complex (UTTAC) Annual Report
number	2016
year	2017
URL	http://hdl.handle.net/2241/00150836

UTTAC-86, 2017

UTTAC

ANNUAL REPORT 2016

TANDEM ACCELERATOR COMPLEX
Research Facility Center for Science and Technology
University of Tsukuba

http://www.tac.tsukuba.ac.jp/

UTTAC

ANNUAL REPORT 2016

April 1, 2016 – March 31, 2017

UTTAC-86, 2017

Editors : Tetsuaki Moriguchi, Kimikazu Sasa,Yoshihiro Yamato, Masumi Matsumura, Masao Sataka, Hiroshi Naramoto, and Hiroshi Kudo

---

UTTAC ANNUAL REPORT is a series of issues, which include annual reports of
Tandem Accelerator Complex, Research Facility Center
for Science and Technology, University of Tsukuba.

Tandem Accelerator Complex, Research Facility Center for Science and Technology,
University of Tsukuba
Tennodai 1-1-1, Tsukuba, Ibaraki 305-8577, Japan

annual@tac.tsukuba.ac.jp

PREFACE

This annual report covers researches carried out at University of Tsukuba Tandem Accelerator Complex (UTTAC) during the fiscal year 2016 (1 April 2016 ~ 31 March 2017). The topics include not only accelerator-based researches using the 6MV Pelletron, 1 MV Tandetron, and 1MV Cockcroft-Walton accelerators, but also radioisotope-based researches including positron annihilation spectroscopy and Mössbauer spectroscopy.

September 30, 2017
Editors

Long and dark years finally ended!

Construction of a new horizontal-type 6 MV Pelletron tandem accelerator was started immediately after the previous accelerator was lost suddenly by the 2011 earthquake. It was completed in 2014, however, it took two more years for legal procedures and the setup of experimental apparatus. Indeed, the experimental use of the accelerator was started in March 2016. The long and dark five years finally ended. Photos below were taken at the opening ceremony and the celebration party, 1 July 2016.

CONTENTS

5. BEAM IRRADIATION EFFECT

6. LIST OF PUBLICATIONS AND PRESENTATIONS

1.

ACCELERATOR AND RELATED FACILITIES

1.1 Accelerator operation 2016

K. Sasa, S. Ishii, H. Oshima, Y. Tajima, T. Takahashi, Y. Yamato, D. Sekiba, T. Moriguchi, A. Uedono

In the fiscal year (FY) 2016, we operated and maintained the 1 MV Tandetron accelerator, the 6 MV Pelletron tandem accelerator, and the apparatus utilizing radio-isotopes. The total service time of UTTAC in this FY was 174 days (4,176 hours).

1 MV Tandetron accelerator

The 1 MV Tandetron accelerator has two types of negative ion sources and four beam lines. In FY 2016, the operating time and the experimental beam time of the Tandetron were 594.3 and 262.1 hours, respectively. The Tandetron had 73 working days for beam experiments. Totally, 66 research programs were carried out and 538 researchers used the Tandetron. Figure 1 shows the percentage of accelerated ions. Figure 2 shows the percentage of research fields for the Tandetron.

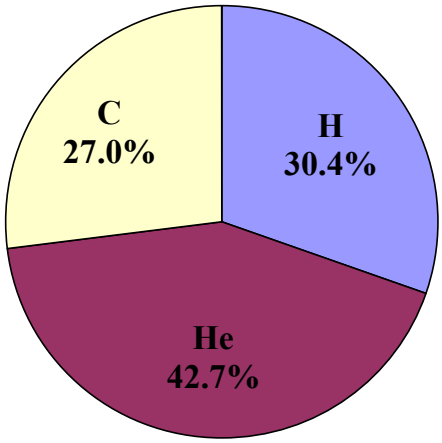

Fig. 1. Percentage of accelerated ions for the 1 MV Tandetron accelerator in FY 2016.

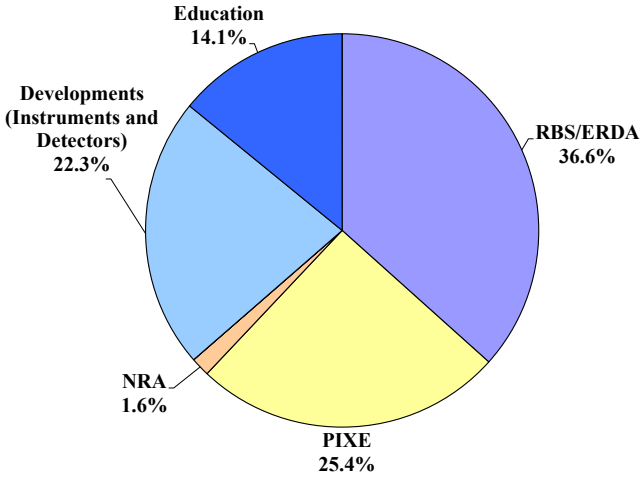

Fig. 2. Percentage of research fields for the 1 MV Tandetron accelerator in FY 2016.

6 MV Pelletron tandem accelerator

For the 6 MV Pelletron tandem accelerator, routine beam delivery and experiments were started on March 1 2016 [2]. We had no trouble in operating the accelerator until just before the end of 2016. At the end of 2016, however, a malfunction occurred in the foil changer which replaces carbon stripper-foils at the accelerator terminal. After urgent repair of the foil changer, the accelerator was back into good condition on January 2017.

In FY 2016, the operating time and the experimental beam time of the Pelletron were 1867 and 1496.4 hours, respectively. The Pelletron had 154 working days for beam experiments. Totally, 95 research programs were carried out and 614 researchers used the Pelletron. Figure 3 shows the beam time

histogram with respect to the terminal voltage. Figures 4 and 5 show the percentages of accelerated ions and of research fields, respectively, for the Pelletron. The operating time with the maximum terminal voltage of 6 MV occupied 37% of all the beam time. Two thirds of the beam time was used for AMS studies. In AMS, radionuclides of ^{14}C, ^{36}Cl, ^{41}Ca and ^{129}I were accelerated during most of the operating hours.

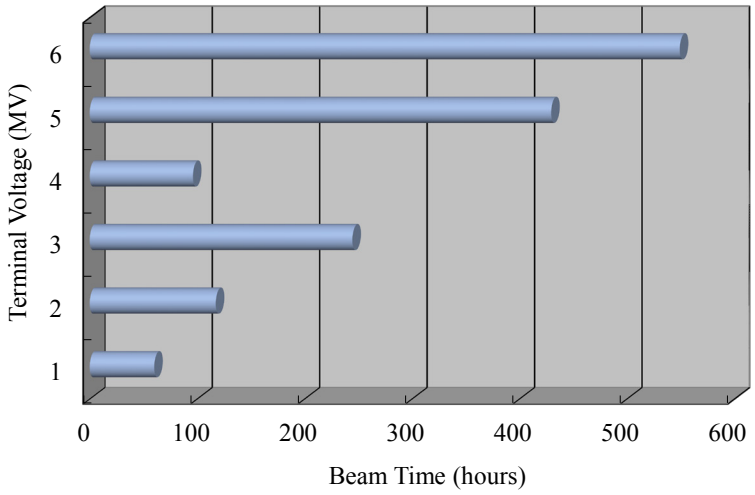

Fig. 3. Beam time histogram as a function of the terminal voltage for the 6 MV Pelletron tandem accelerator in FY 2016.

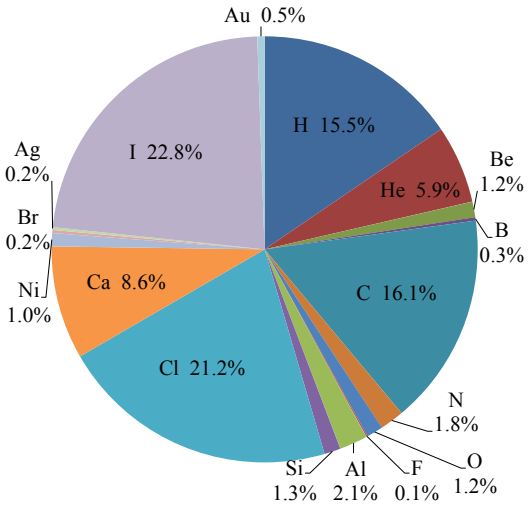

Fig. 4. Percentage of accelerated ions for the 6 MV Pelletron tandem accelerator in FY 2016.

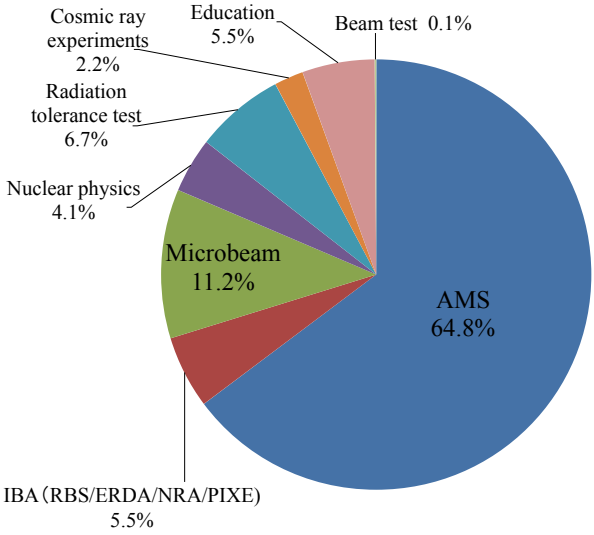

Fig. 5. Percentage of research fields for the 6 MV Pelletron tandem accelerator in FY 2016.

References

[1] K. Sasa et al., Nucl. Instr. Meth. B 361 (2015) 124.

[2] K. Sasa et al., UTTAC Annual Report 2015, UTTAC-85 (2016) 1.

1.2 Development of the Lamb-shift polarized ion source

T. Moriguchi, Y. Yamato, A. Ozawa, S. Suzuki, M. Amano, D. Kamioka

The reconstruction of the Lamb-shift polarized ion source (PIS), which was damaged seriously by the Great East Japan Earthquake, was mostly finished [1]. We therefore began to generate polarized beams. A spin filter (SF), which is one of the devices constituting PIS, is of significance for the nuclear polarization [2]. SF was designed to provide (1) a uniform magnetic field parallel to the beam axis, (2) a 1610 MHz radio-frequency (RF) electric field parallel to the beam, and (3) a static electric field perpendicular to the beam. In order to produce the polarized beam, it is necessary to adjust these parameters of SF properly. In this fiscal year, we tuned the magnetic field and the RF electric field of SF, and tried to generate polarized proton and deuteron beams.

Firstly, we measured the magnetic field parallel to the beam axis against electric current supplied for the electromagnet. Prior to the measurements, a Hall probe (DTM-151, Group3 Technology Ltd.) mounted on an axial holder was installed into the center of the beam axis inside SF after removing an argon gas chamber, which are located just downstream of SF. Figure 1 shows the results. The finite magnetic field seen at 0 A is induced by other coils for the correction of the fringing field. Except for this external field, the good linearity between the magnetic field and electric current is confirmed.

Next, we measured oscillation frequency for the RF electric field and a resonance frequency of SF. The oscillation frequency was measured using the spectrum analyzer (MS2721B, Anritsu) which was connected between the output of the power supply and the input of the RF electric field of SF. The oscillation frequency thus obtained is 1610 MHz, as is expected. The resonance frequency of SF was measured by a network analyzer (8753ET, Agilent). For stabilization of SF, the power supply was turned on 25 hours before this measurement. In order to investigate the shift of the resonance frequency due to change in the temperature of SF, we measured again in two hours after the power supply was turned off. The results are shown in Fig. 2. The resonance frequency of SF was 1609.475 MHz which is shifted from the oscillation frequency of 1610 MHz. After the power supply was turned off, the resonance frequency was shifted towards the oscillation frequency, possibly by self-cooling of SF.

Then, we performed a test for generating the polarized beam. In order to prevent the shift of the resonance frequency, two large-sized air fans were used to cool SF. The beam current was measured by the Faraday cup (FC-PIS) located downstream of PIS. Figure 3 shows the measured beam current as a function of the magnetic field of SF. Actually, the negative current was measured because negatively charged proton or deuteron were extracted from PIS. For proton, we found two resonance peaks around 540 and 605 G, which correspond to the nuclear spin magnetic quantum number m_I = +1/2 and −1/2, respectively. The polarization of m_I = +1/2 peak was about 80% by using a quenching method. For deuteron, we found three resonance peaks around 565, 575 and 585 G, which correspond to m_I = +1, 0 and −1, respectively. These resonance peaks for proton and deuteron were not observed without cooling of SF. For generation of the polarized beam from PIS, it is important to control the temperature of SF so as to adjust the resonance frequency of SF to the oscillation frequency of the power supply. As the next step, we

will improve the cooling system of SF and measure the polarization at the end of the experimental beam course by using a polarimeter via a nuclear reaction.

We acknowledge the technical support of Drs. Y. Tagishi and M. Tomizawa. We would like to thank NIHON KOSHUHA Co., Ltd. staff for measurements of the oscillation and resonance frequencies.

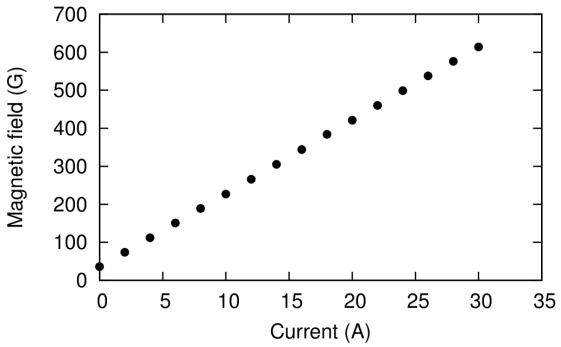

Fig. 1. Magnetic field of SF as a function of current from the power supply.

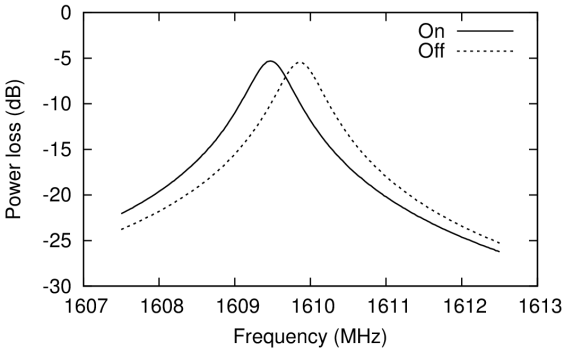

Fig. 2. Power loss of the RF electric field as a function of frequency. On and Off indicate “before” and “after” the power supply is turned off, respectively (see the text).

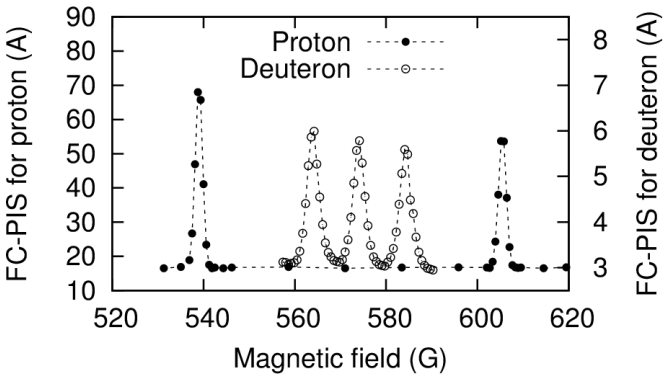

Fig. 3. Beam current measured by the Faraday cup (FC-PIS) as a function of the magnetic field.

References

[1] T. Moriguchi et al., UTTAC Annual Report 2014 (2015) 7.

[2] Y. Tagishi et al., Nucl. Instr. Meth. 164 (1979) 411.

1.3 Development of an ion microbeam scanning system in the 6 MV tandem accelerator facility

A. Yamazaki, K. Sasa, S. Ishii, M. Kurosawa, S. Tomita, H. Naramoto, M. Sataka, H. Kudo, A. Uedono

Light trace elements in structural materials sensitively affect materials' properties. Many researchers have paid much attention to microstructural analysis of the relevant elements. Ion beam can provide various elemental analyses in materials. Combining ion beam focusing and scanning techniques, we can obtain spatial distribution of elements.

The ion microbeam system has been constructed in 2016 at UTTAC [1]. Schematic view of the ion microbeam line is shown in Fig. 1. This system will be mainly used for analysis of light elements in structural materials, based on various interaction processes of incident ions with the elements.

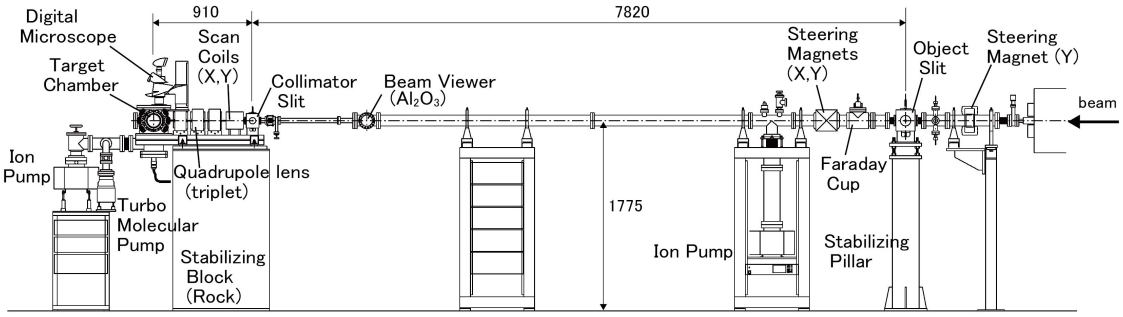

Fig. 1. Schematic view of the ion microbeam line of the 6 MV tandem accelerator facility (lengh is indicated in mm). A new large target chamber is shown at the end of the microbeam line.

Particle induced X-ray emission (PIXE) has been widely used for analysis of trace elements. For X-ray measurements, a silicon drift detector (SDD) with a thin front window has been installed, and a superconducting tunnel junction (STJ) array detector [2, 3] will be installed for sensitive PIXE analyses of light elements.

Analysis of hydrogen in materials is of both academic and practical importance because hydrogen plays an important role for determining the mechanical properties of materials. The PIXE method is not applicable to hydrogen analysis because of no characteristic X-ray emission from hydrogen. Hydrogen can be detected using ion beams by applying nuclear reaction analysis (NRA) or elastic recoil detection analysis (ERDA). To support these techniques, a large target chamber has been installed. This is designed for multi-purpose analysis; to utilize not only SDD and STJ detector but also a BGO detector for NRA. Furthermore, a silicon surface barrier detector was set up for elastic recoil detection analysis (ERDA) .

Figure 2 shows a top view of the new chamber. It is 240 mm in inner diameter and 228 mm in height. The SDD and STJ detector are placed at 135° and at −90° relative to the beam direction, respectively. A PIN photodiode which is used for estimating the diameter of a focused ion beam by scattering transmission ion microscopy (STIM) is installed at 0° port with a Faraday cup. BGO detector for NRA can be installed at the same port in replace of the photodiode and Faraday cup assembly. Silicon surface barrier detectors for ERDA and RBS can also be installed in the chamber.

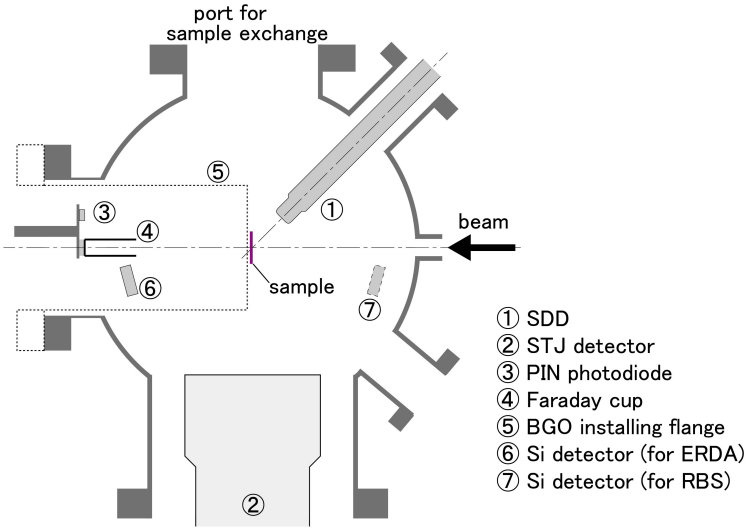

Fig. 2. Top view of the new target chamber and arrangement of the detectors.

Samples are fixed on the three-dimensional positioning stage. The horizontal and vertical positioning ranges are 15 mm and 50 mm, respectively. It can also move along the beam axis within 10 mm to set the surface of the sample at the center of the chamber. A digital microscope is fixed on the chamber to view the sample normally through a mirror which is positioned on the beam axis and is held obliquely at 45°.

Ion beam transport and focusing were carried out mainly with 6 MeV protons. Figure 3 shows an example of STIM images of a copper fine grid (1000 lines per inch, 6 μm grid width) which was obtained by scanning of focused protons. The estimated beam diameter is 2 μm.

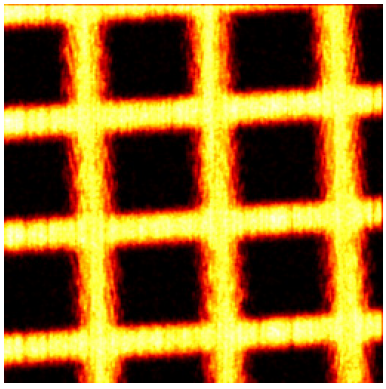

Fig. 3. STIM image of the copper fine grid (1000 lines per inch) using a 6 MeV proton beam.

References

[1] A. Yamazaki et al., Nucl. Instrum. Methods B 404 (2017) 92.

[2] M. Ukibe et al., X-ray Spectrom. 40 (2011) 297.

[3] S. Shiki et al., J. Low Temp. Phys. 167 (2012) 748.

1.4 Characteristics of irradiation-test chamber for semiconductor devices

M. Sataka, K. Sasa, H. Naramoto, H. Kudo

Single-event phenomena in microelectronics devices are caused in the space environment by high energy particles which impinge on the sensitive regions of the devices [1,2]. In recent years, there has been increasing attention in the possible use of commercial electronic devices for space applications. It is also noted that even on the ground the microelectronic devices are susceptible from secondary cosmic rays that are induced by primary neutrons, and from alpha emitters such as U and Th contaminants within chip packaging materials.

The new irradiation-test chamber dedicated for semiconductor devices was installed in a beam course of the 6 MeV tandem accelerator at UTTAC in 2015. This chamber consists of main and sub chambers which are differentially evacuated by two turbo molecular pumps. The base pressures are 2×10^{-5} Pa and 1×10^{-6} Pa, respectively. The overview of the irradiation-test chamber is shown in Fig. 1. On the upstream side, installed is the beam handling sub chamber containing slits, aperture, foils, and a Faraday cup. The main chamber is about 1000 mm in diameter and about 750 mm in height. In the beam shutter system, two linear motion feedthroughs and the target stage are built together. The liner motion feedthrough covers a distance of 150mm with the resolution of 0.01mm. The target stage, on which a sample holder up to so called A5 size (140mm×210mm) can be mounted, enables four different movements (two independent translations and two independent rotations). These are controlled by the driver-handling system implemented in the LabVIEW environment.

Fig. 1. Overall view of the irradiation-test chamber for semiconductor devices.

The details of sample setting are shown in Fig. 2. The specification of target stage is summarized in Table 1. This test chamber will be also useful for various kind of ion irradiation on materials since the basic mechanisms required for the controlled irradiation experiments are already built in this chamber. We have also introduced an ion beam scanning system for uniform irradiation with various intensity levels from faint to intense ion beam.

Fig. 2. Inside view of the main chamber, showing the target stage and the goniometer system.

Table 1. Specification of the goniometer system for target stage control.

x-travel	±74 mm
y-travel	±105mm
θ-rotation	+30 ~ –90 degree
φ-rotation	±90 degree

References

[1] M. Komatsu et al., this annual report 5.1 (2017).

[2] A. Maru et al., this annual report 5.2 (2017).

1.5 Approach to possible maximum energies of high *Z* ions accelerated by the 6 MV tandem accelerator

M. Sataka, K. Sasa, H. Naramoto, T. Takahashi, H. Kudo

A tandem-type accelerator can provide many kinds of ion species with wide energy ranges, compared with a single-stage electrostatic accelerator. Because of such wide variety of ion beams, tandem accelerators have been used for comprehensive studies of electronic excitation processes in materials. Furthermore, tandem accelerators allow irradiation-tolerance tests under wide experimental parameters of electronic devices to be operated in space. At the present stage of the irradiation-test experiments at UTTAC, we need a systematic data base concerning the maximum energies of high *Z* elements which are obtained from the 6 MV tandem accelerator.

We have measured the beam current distribution of accelerated ions as a function of ion charge, employing Ar gas as the charge stripper. Figure 1 shows the beam current distribution of iodine ions at the terminal voltage of 6 MV. The beam current is maximal at the ion charge of 6, and it decreases drastically as the ion charge increases. In a critical use of the 6 MV tandem accelerator, an I^{14+} beam of the highest energy 90 MeV is available[1]. Similar data were obtained for He, O, F, Si, Cl, Ni, Br, Ag, and Au.

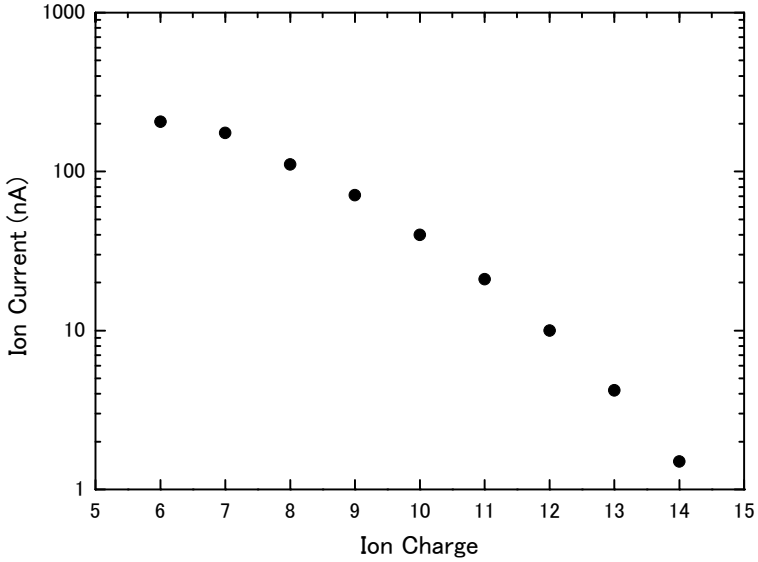

Fig. 1. Beam current distribution of iodine ions accelerated by the 6 MV tandem accelerator at the terminal voltage of 6 MV.

Table 1 summarizes the availability of tested ion species. In this table, ion charge, ion energy and ion current range are listed. There appear some uncertainties in the data for acceleration of highly charged ions of Br, Ag and Au. This is mainly due to electron loading, however it can be fixed after some improvement. Similar data base for B and C will be complemented soon, and the tests for medium heavy ions such as Cl, Ni, and Br will be easily performed using a foil stripper at the high voltage terminal of the accelerator.

[1] Calculated as (14+1)×6=90 (MeV).

Table 1. Availability of the ion species at the terminal voltage of 6 MV: ○:≥1nA, △: ≤1nA.

Charge	Energy	Ion Species									
state	(MeV)	He	O	F	Si	Cl	Ni	Br	Ag	I	Au
14	90								△	○	△
13	84							△	△	○	△
12	78						△	○	○	○	○
11	72						○	○	○	○	○
10	66						○	○	○	○	○
9	60						○	○	○	○	○
8	54				○	△	○	○	○	○	○
7	48				○	○	○	○	○	○	
6	42		○	○	○	○	○	○	○		
5	36		○	○	○	○	○	○	○		
4	30			○	○	○	○	○			
3	24			○	○		○				
2	18	○		○							
1	12	○									

2.

NUCLEAR AND ATOMIC PHYSICS

2.1 Production of unstable nuclei by proton-capture reactions with a Si target

A. Ozawa, T. Moriguchi, M. Amano, D. Kamioka, S. Suzuki

We are attempting to produce polarized unstable nuclei by proton-capture reactions with polarized proton beams in the aim of measuring nuclear moments of unstable nuclei. Up to now we have tried to produce unstable nuclei by proton-capture reactions using Mg and Si targets in 1 MV Tandetron [1]. From the γ ray measurement with the Ge detector, it was confirmed that unstable nuclei ^{25}Al ($T_{1/2}$ = 7.1 s) and ^{30}P ($T_{1/2}$ = 150 s) could be produced for each target [1]. In FY2016, we shifted to 6MV tandem accelerator, which began to operate in March 2016, and started an experiment there.

In FY2016 we performed an experiment using a non-polarized proton beam. The proton beam accelerated to 3 MeV by a 6 MV tandem accelerator was irradiated on a 0.5 mm thick Si target placed in a chamber located in the A6 course. The proton beam induces the proton-capture reactions including resonant reactions until it stops in the Si target. Natural Si has three stable isotopes (^{28}Si: 92.2%, ^{29}Si: 4.7%, ^{30}Si: 3.1%). Among ^{29}P, ^{30}P, and ^{31}P, that can be produced by the proton-capture reactions in the Si target, ^{29}P ($T_{1/2}$ = 4.1 s) and ^{30}P are unstable nuclei with β decays. In order to measure β rays associated with the β decays, two plastic scintillators were located on top of the target (plastic thicknesses 1 mm and 2 mm, respectively). We identified the coincidence signals of the two scintillators as the β rays. Figure 1 shows the time spectrum of β rays observed after irradiation of the proton beam (its intensity about 50 nA) for 100 seconds. Fast and slow components of the β decay were observed. The fitting results assuming half-lives of ^{29}P and ^{30}P are shown by a solid line in Fig. 1. The β ray amounts of ^{29}P and ^{30}P evaluated from the fitting results were ~0.12 cps/nA and ~0.30 cps/nA, respectively. In the future, we will use the polarized proton beam to measure the nuclear polarization of the produced unstable nuclei (^{29}P, ^{30}P and so on), and furthermore perform experiments with the target containing Mg to evaluate the production amount of ^{25}Al and its nuclear polarization. If significant nuclear polarization is observed, nuclear moment measurements for ^{30}P and ^{25}A1 will be carried out.

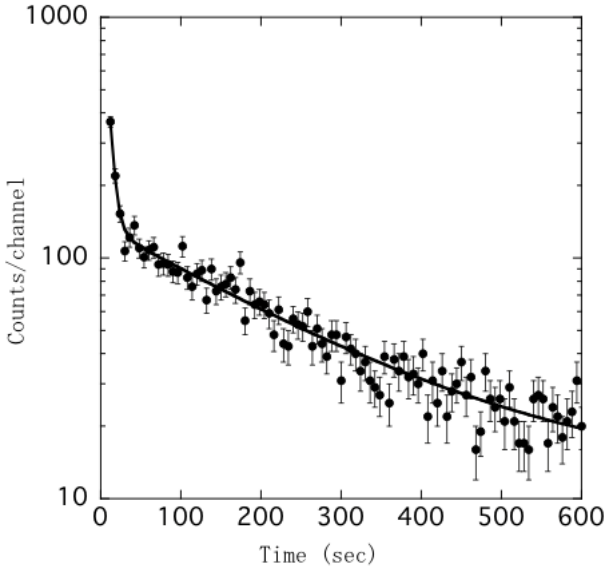

Fig. 1 Time spectrum of β rays in 3 MeV proton beam with a Si target. The solid line is the fitting result assuming half-life of ^{29}P and ^{30}P.

Reference

[1] T. Matsumoto et al., UTTAC Annual Report 2015 (2016) 11.

2.2 The qualification test of sulfur targets for intense beam irradiation

S. Kimura, A. Ozawa, T. Moriguchi, H. Miyatake[1], Y. Hirayama[1], Y.X. Watanabe[1], M. Mukai, M. Oyaizu[1]

Nuclear masses in the vicinity of the $N = Z$ line are crucial to determine the rapid-proton capture process (rp-process) pathway, which drives an explosive astronomical phenomenon called type I X-ray burst. Unfortunately, the masses of key nuclei in the rp-process have not been measured experimentally yet with the required precision, in particular the mass evaluation of ^{66}Se has been highly desired.

The mass measurement of ^{66}Se by using the SHE-mass facility, which consists of a multireflection time-of-flight mass spectrograph [1] coupled with a gas-filled recoil ion separator GARIS-II [2] has been planned. In order to produce ^{66}Se, a fusion-evaporation reaction ^{32}S(^{36}Ar, 2n)^{66}Se will be employed. A production cross-section of ^{66}Se via this reaction is estimated to be $\sim$ 70 nb, therefore sulfur targets that are applicable to intense ^{36}Ar beam irradiation are required. The MoS_2 targets prepared by a spray coating technique [3] on Ti backing foils are adopted as the sulfur targets. MoS_2 has large sulfur composition ratio and is chemically stable, but its stability to intense beam irradiation is still unclear. Thus there is a need to confirm an irradiation tolerance of the MoS_2 targets.

A 40.6 MeV $^{35}Cl^{6+}$ beam, with average intensity of 20 pnA, was provided by the 6 MV tandem electrostatic accelerator at University of Tsukuba. The experimental setup in the scattering chamber of A7 course is shown in Fig. 1. A Mo$^{nat}S_2$ target on 3 μm Ti backing foil was mounted on a target ladder. A target thickness was 0.8 mg/cm^2. A Si detector and an ^{241}Am α-source were installed diagonally across the target ladder.

Measurements were performed by repeating the following procedure: irradiation of the $^{35}Cl^{6+}$ beam is carried out in a certain period of time and, subsequently, the thickness of Mo$^{nat}S_2$ target is measured via an energy spectrum of α-particles fed from the ^{241}Am source. Figure 2 shows the measured peak energy

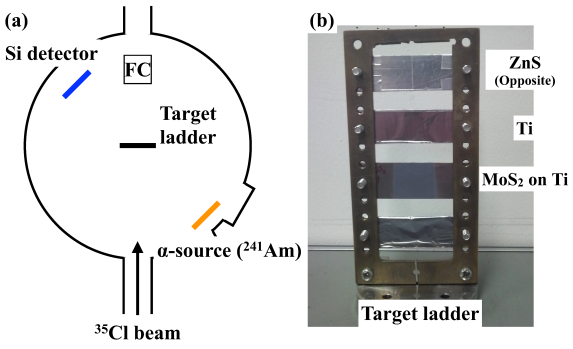

Fig. 1. (a) Schematic view of the experimental setup. (b) Photograph of the target ladder.

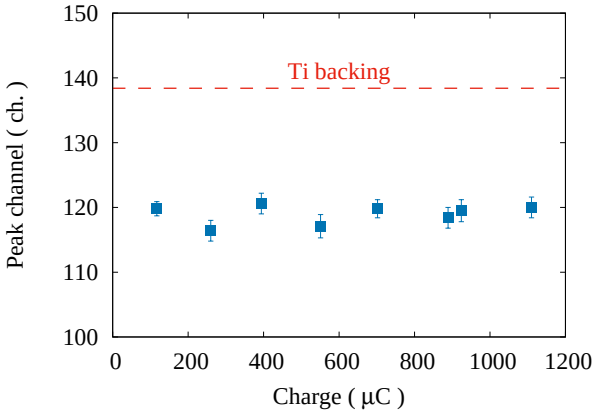

Fig. 2. Peak energy shift of the α-particles. Red dashed line shows the peak position of the α-particles passed only through the Ti backing foil.

[1]Wako Nuclear Science Center (WNSC), Institute of Particle and Nuclear Study (IPNS), High Energy Accelerator Organization (KEK), Wako 351-0198, Japan

shift of the α-particle which passed through the $Mo^{nat}S_2$ target. In Fig. 2, no significant peak shift is observed for the beam irradiation up to $\sim$ 1200 μC; it indicates that the beam irradiation does not affect the stability of the $Mo^{nat}S_2$ target. Total measurement time was calculated to be 3 hr and a 30 cm diameter rotating target wheel [4] will be used in the SHE-mass facility. The present test corresponds to a 28 hr irradiation with 1 pμA beam.

Thus we confirmed that there is no problem in the stability of MoS_2 targets under the intense beam irradiation.

References

[1] P. Schury et al., Nucl. Instr. Meth. Phys. Res. B 335 (2014) 39.

[2] D. Kaji et al., Nucl. Instr. Meth. Phys. Res. B 317 (2013) 311.

[3] J. P. Greene and C. J. Lister, Nucl. Instr. Meth. Phys. Res. A 480 (2002) 79.

[4] D. Kaji and K. Morimoto, Nucl. Instr. Meth. Phys. Res. A 792 (2015) 11.

2.3 Test experiment for the isotope analysis of sulfuric acids generated in atmospheric air by proton irradiation

Y. Nakai[1], Y. Shiina, N. Yamamoto, K. Sasa, S. Tomita

Gas-phase particle formation following irradiation of ionizing particles is one of major processes in a gas involving chemical species, such as water, sulfuric acid, volatile organic compound, which can be condensed depending on atmospheric pressure and temperature. Especially, it has been known that sulfuric acid enhances generation of small droplets by ionizing radiation [1, 2]. In this case, sulfuric acid is considered to be formed mainly through an oxidation of SO_2. However, the detailed mechanism of SO_2 oxidation by irradiation of ionizing particles has not been identified yet although some indications have been proposed [3].

To investigate the mechanism of SO_2 oxidation, Ishino et al. [4] performed isotope analysis of oxygen and sulfur in sulfuric acid and sulfate mainly contained in nano-droplets generated in humidified gases irradiated with a 1.8 MeV proton beam. Measured $\Delta^{17}O$ values were roughly consistent with the mechanism for SO_2 oxidation suggested in previous studies [3, 5]. On the other hand, the values of $\Delta^{34}S$ in this study are quite different from those of already-known major reactions for atmospheric sulfate production [3, 6]. This discrepancy has not been resolved yet. One of possible reasons is that the protons lost all the kinetic energies and were fully stopped in the target gases. Just before being stopped in the gas, the electronic stopping power for the protons is increased. Thus, high ion density and different proportion of excited products might induce more complex chemical reactions.

We plan to perform oxygen and sulfur isotope analysis of sulfuric acid (and sulfate) produced in irradiation of a 12 MeV proton beam using 6 MV Pelletron tandem accelerator at UTTAC. Since 12 MeV protons have the range of 1.57 m in the atmosphere of 1 atm, use of an irradiation chamber of 25 cm in length allows us to avoid complexity caused by the stopping of the beam within the gas. As the first step in this year, we performed measurements of SO_2 consumptions as functions of an SO_2 mixing ratio and a beam current to find suitable experimental conditions for isotope analysis of sulfuric acid. Figure 1 shows the setup for the test experiment, which consists of a humidified sample-gas generator, an irradiation chamber, a monitor of the sample gas pressure, and a monitor of the SO_2 concentration. A wet air was generated by bubbling pure air in ultra-pure water. The sample gas was produced by mixing the wet air with a dry air of the same purity. The total flow rate of the sample gas was maintained at 2 SLM (Standard Liters per Minute) using mass flow controllers. A part of gas flow downstream of the irradiation chamber was introduced to the SO_2 concentration meter.

In this test experiment, we found that the SO_2 consumptions increase with not only higher SO_2 mixing ratio, but also higher beam current. For high beam current, the SO_2 consumptions are saturated and the saturation beam current becomes higher for higher SO_2 mixing ratio.

[1] RIKEN Nishina Center

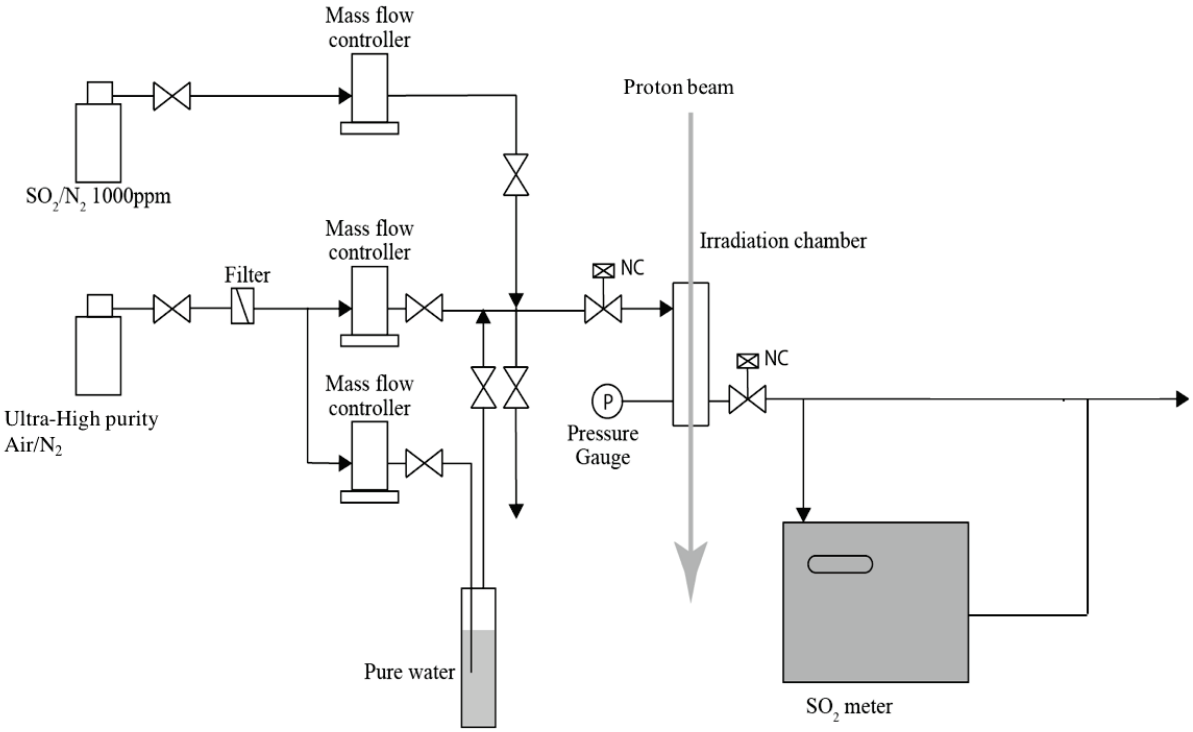

Fig. 1. Schematic drawing of the experimental setup.

References

[1] J. H. Seinfeld and S. N. Pandis, Atmospheric Chemistry and Physics: From Air Pollution to Climate Change (Wiley-Interscience, 2006), 2nd ed.

[2] S. Tomita et al., Nucl. Instr. Meth. Phys. Res. B 365 (2015) 616.

[3] M. B. Enghoff et al., Atmos. Chem. Phys. 12 (2012) 5319.

[4] S. Ishino et al., UTTAC Annual Reports 2014, p36 (2015).

[5] N. Bork et al., Atmos. Chem. Phys. 13 (2013) 3695.

[6] E. Harris et al., Environ. Sci. Technol. 47 (2013) 12174.

3.

ACCELERATOR MASS SPECTROMETRY

3.1 Operation of the Tsukuba 6 MV multi-nuclide AMS system for the year 2016

K. Sasa, T. Takahashi, T. Matsunaka, S. Hosoya, M. Matsumura, H. Shen, M. Honda, Y. Ota, K. Matsuo, A. Sakaguchi, K. Sueki

A new horizontal-type 6 MV Pelletron tandem accelerator (model 18SDH-2 Pelletron, NEC, USA) was installed at the University of Tsukuba in March 2014 [1]. After 2 years of construction and preparation, the first test on multi-nuclide AMS has been performed in March 2016. The rare particle detection system on the 6 MV Pelletron tandem accelerator (Tsukuba 6 MV multi-nuclide AMS system) was designed and constructed for high-sensitivity detections of ^{10}Be, ^{14}C, ^{26}Al, ^{36}Cl, ^{41}Ca, and ^{129}I, and was also expected to measure other radioisotopes of ^{32}Si and ^{90}Sr. The background of the system for ^{14}C measurements using the 4+ charge state and the terminal voltage V_T = 5.0 MV was reached down to $^{14}C/^{12}C = 2.4 \times 10^{-16}$. In addition, we successfully detected ^{10}Be, ^{26}Al, ^{36}Cl, ^{41}Ca, and ^{129}I by the multi-nuclide AMS system in 2016. In the case of ^{10}Be AMS, $^{10}BeO^-$ was extracted from the MC-SNICS and then accelerated with V_T = 6.0

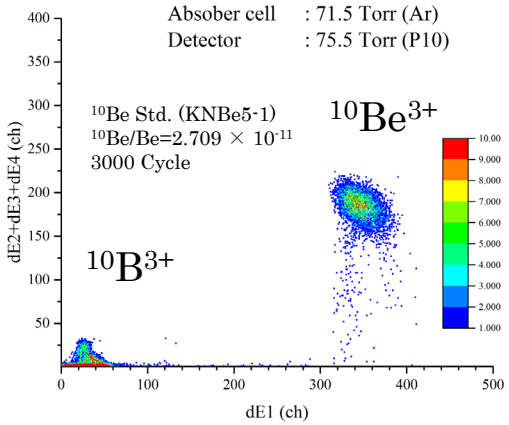

Fig. 1. Two-dimensional spectrum of ^{10}Be AMS measured with the five-anode ΔE–E gas ionization detector.

Table 1. Performance of rare particle detections by the multi-nuclide AMS system.

Isotopes	**^{10}Be**	**^{14}C**	**^{26}Al**	**^{36}Cl**	**^{41}Ca**	**^{129}I**
Half-life (yr)	1.36×10^6	5,730	7.17×10^5	3.01×10^5	1.03×10^5	1.57×10^7
Stable isotopes	^{9}Be	^{12}C, ^{13}C	^{27}Al	^{35}Cl, ^{37}Cl	^{40}Ca, ^{42}Ca, ^{43}Ca, ^{44}Ca	^{127}I
Isobars	^{10}B	$^7Li_2$, $^{12}CH_2$, ^{13}CH, ^{14}N	^{26}Mg	^{36}Ar, ^{36}S	^{41}K	^{129}Xe
Chemical form	BeO	Graphite, CO_2	Al_2O_3	AgCl	CaF_2	AgI
Sample size (mg)	0.5	0.1 - 1	2	1	10	2
Injected ion	BeO^-	C^-	Al^-	Cl^-	CaF_3^-	I^-
Typical ion current (μA)	5 ($^9BeO^-$)	10 - 50 ($^{12}C^-$)	0.2 ($^{27}Al^-$)	10 ($^{35}Cl^-$)	0.5 ($^{40}CaF_3^-$)	5 ($^{127}I^-$)
Terminal Voltage (MV)	6.0	5.0	6.0	6.0	6.0	5.0
Detected ion (Stripper)	$^{10}Be^{3+}$ (gas)	$^{14}C^{4+}$ (gas)	$^{26}Al^{5+}$ (gas)	$^{36}Cl^{8+}$ (foil)	$^{41}Ca^{5+}$ (foil)	$^{129}I^{5+}$ (gas)
Beam Energy (MeV)	20.3	25.0	36.0	54.0	32.5	30.0
Transmission (%)	15	40	25	10	8	10
Measure/Known (%)	80	–	75	70	50	90
Precision (%)	2	0.2 (Graphite) 0.4 (CO_2)	2	2	3	1
Background (atom ratio)	$< 2 \times 10^{-15}$	$< 2 \times 10^{-16}$ (Graphite) $< 5 \times 10^{-15}$ (CO_2)	$< 1 \times 10^{-16}$	$< 3 \times 10^{-15}$	$< 3 \times 10^{-15}$	$< 2 \times 10^{-14}$

MV. As a result, 20.3 MeV Be^{3+} was detected by a five-anode ΔE–E gas ionization detector. Isobaric interference of ^{10}B was eliminated by an absorber cell in front of the detector. Figure 1 shows a two dimensional spectrum of ^{10}Be AMS for a standard of $^{10}Be/Be = 2.709 \times 10^{-11}$. The background of ^{10}Be AMS is lower than 2×10^{-15}. Table 1 summarizes the performance of rare particle detections by the multi-nuclide AMS system.

We measured 1,120 samples in total by the multi-nuclide AMS system in the period from March 2016 to March 2017. Figure 2 shows a breakdown by types of measured nuclides. Figure 3 shows monthly-measured nuclides from March 2016 to March 2017. ^{129}I was measured most frequently in the fiscal year 2016 in order to investigate the radiative contamination of ^{131}I from the Fukushima Daiichi Nuclear Power Plant accident.

Nuclides	Number
^{10}Be	13
^{14}C	321
^{26}Al	30
^{36}Cl	184
^{41}Ca	88
^{129}I	484
Total	1120

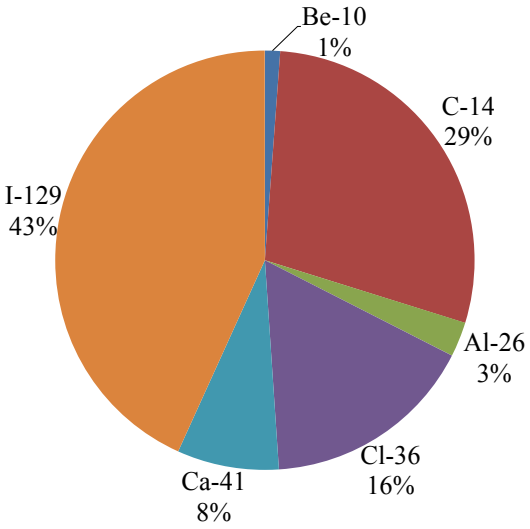

Fig. 2. Breakdown of measured nuclides by the multi-nuclide AMS system in the fiscal year 2016.

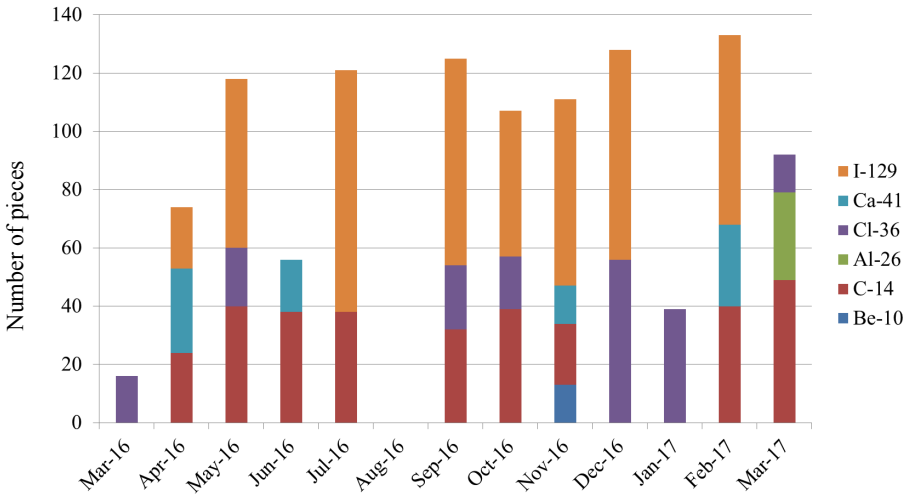

Fig. 3. Breakdown of monthly-measured nuclides by the multi-nuclide AMS system from March 2016 to March 2017.

Reference

[1] K. Sasa et al., Nucl. Instr. Meth. B 361 (2015) 124.

3.2 ^{36}Cl AMS measurements with the 6 MV tandem accelerator

S. Hosoya, K. Sasa, T. Takahashi, T. Matsunaka, M. Matsumura, H. Shen, K. Sueki

^{36}Cl ($t_{1/2}$ = 3.0 × 10^5 yr) is a long-lived radionuclide and mainly used to determine the exposure age of meteorites and to study the land-forming process. In addition, it has been used as an environmental tracer in groundwater [1] and ice core studies [2]. However, ^{36}Cl AMS measurement is interfered by an isobar ^{36}S. In AMS, ^{36}Cl is separated from other ions using mass analyzing magnets and electrostatic energy analyzer. However, the isobar ^{36}S has the same analyzing trajectory as for ^{36}Cl because both of them have the same mass and energy. This causes the interference noted above. Therefore, it is necessary to separate these isobars by the difference of energy loss in the gas ionization detector. Also, in order to achieve highly sensitive AMS measurements sulfur contents must be minimized in sample materials. We try several methods to reduce the influence of ^{36}S and achieve the low-background AMS system.

The sulfur ions are mainly generated within the ion source if Cs beams irradiate the metal surface of the sample holder on which an AMS sample is fixed. Therefore, the amount of sulfur ion depends on material and dimension of the sample holder. We investigated the relation between various sample holders and the amount of sulfur ion. Figure 1 shows comparison of sulfur counts for various conditions of two sample holders S-1 and S-2, which are made of Cu. The diameters of the surfaces of S-1 and S-2 are 3 and 7 mm, respectively. Ta and AgBr are used as backing materials which cover the surfaces of the holders. The results show that the smaller-sized S-1 generates larger amount of sulfur ions, probably because the metal surface is more exposed to the Cs beam. From this result, it is concluded that the sample holder S-2 + AgBr backing is the most suitable choice for ^{36}Cl AMS measurements. Probably, the reason why sulfur decreases for AgBr backing is that sulfur is removed during the purification process of producing AgBr.

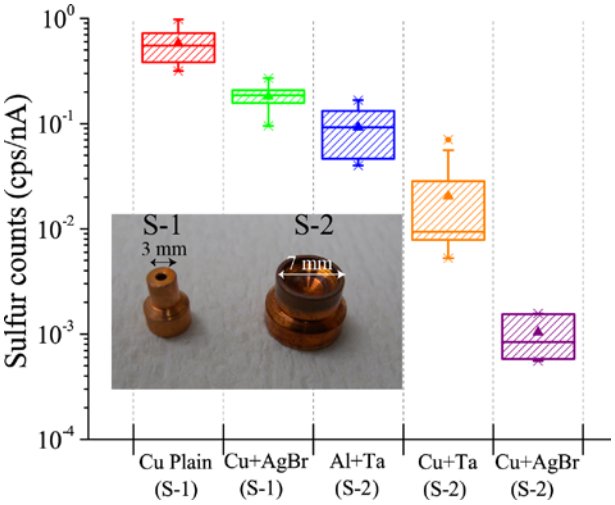

Fig.1. Comparison of sulfur counts due to differences with sample holder materials. Sulfur counts normalized with ^{35}Cl beam current.

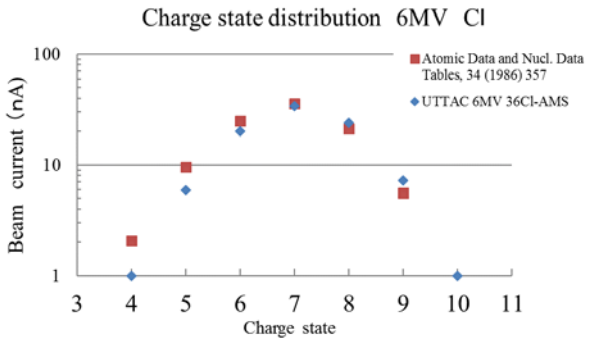

Fig.2. Charge state distribution of Cl at 6 MeV. Carbon foil of 4.8 μg/cm^2 is used as a stripper foil.

For Cl/S isobar separation at the 6 MV terminal voltage, we determined optimum conditions of the five-anode gas ΔE-E detector [3], using the Monte Carlo simulation code [4]. We also considered chlorine charge state distribution at 6 MeV energy, which is shown in. Fig. 2. While Cl^{7+} has the highest beam current, we selected Cl^{8+} because the

spectrum separation becomes greater than for Cl^{7+}, as will be discussed later. Indeed, the beam current is not an important factor under the present conditions of ^{35}Cl ~ 15 – 20 μA. The Cl/S isobar separation is represented by the separation ability *M'* [3]. The values of *M'* for Cl^{7+} and Cl^{8+} separation, listed in Table 1, clearly show better Cl/S isobar separation for Cl^{8+} than for Cl^{7+}. Figure 3 shows the histogram of $^{36}Cl^{8+}$ obtained from the AMS measurement. Since at dE3 the $^{36}Cl^{8+}$ spectrum still overlaps with the $^{36}S^{8+}$ spectrum., we gated on 2σ using dE3 signal.

Table 1. Separation ability *M'* for Cl^{7+} and Cl^{8+}.

	dE1 + dE2	dE4 + dE5
Cl^{7+} meas.	1.249	0.580
Cl^{8+} meas.	1.421	0.675

After such attempts, the detection sensitivity of $^{36}Cl/Cl$ reached as low as ~ 3×10^{-15}. This value is the highest performance in Japanese AMS facilities. Further refinement of the AMS system is needed to achieve higher sensitivity realized so far by several foreign facilities.

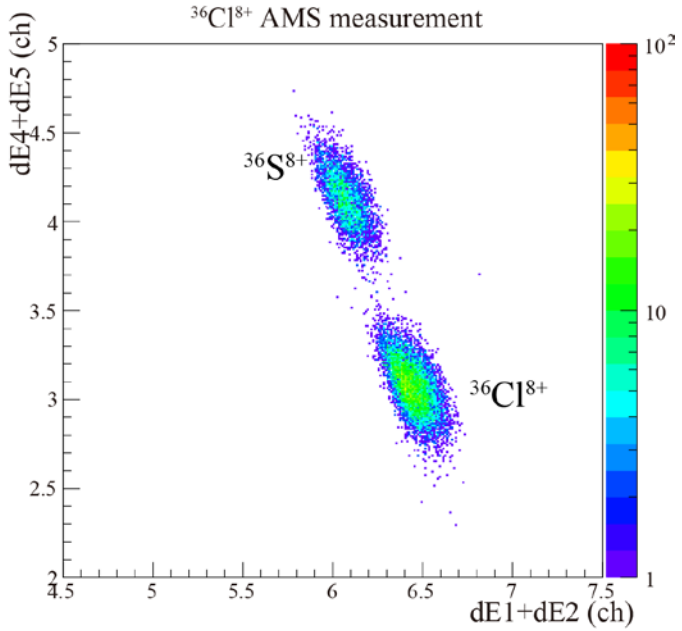

Fig.3. dE1 + dE2 vs. dE4 +dE5 spectrum after gating dE3 signal on the gas ionization detector for the sample with $^{36}Cl/Cl$ ratio of 1.000×10^{-11}.

References

[1] Y. Tosaki et al., J. Environ. Radioact., 106 (2012) 73.

[2] K. Sasa et al., Nucl. Instr. Meth. B, 268 (2010) 1193.

[3] S. Hosoya et al., UTTAC Annual Report, 2015 (2016) 17.

[4] T. Sato et al., J. Nucl. Sci. Technol., 50 (2013) 913.

3.3 $^{36}Cl/Cl$ and ^{36}Cl inventory in surface soils near the Fukushima Dai-ichi Nuclear Power Plant

Y. Ohta, K. Sueki, K. Sasa, T. Takahashi, S. Hosoya, M. Matsumura

On March 11, 2011, the Great East Japan Earthquake caused the Fukushima Dai-ichi Nuclear Power Plant (FDNPP) accident. In consequence, a large amount of radionuclides were released into environment. Most of the radionuclides released in this accident were from ^{235}U in the nuclear fuels. On the other hand, radioisotopes that had their origins in coolant or nuclear reactor materials were also discharged. One of them is ^{36}Cl.

^{36}Cl in this case is generated by ^{35}Cl (n, γ) ^{36}Cl, where ^{35}Cl is contained in the coolant as impurities. At the time of the accident, therefore, ^{36}Cl surely existed in the coolant. However, there is one published article only which reports on the emission of ^{36}Cl in FDNPP accident. This is probably because ^{36}Cl in environmental samples can only be measured by accelerator mass spectrometry (AMS) which is usually interfered with ^{36}S, an isobar of ^{36}Cl. For this reason, ^{36}Cl AMS requires a lot of chemical treatments.

In Japan, there are two AMS facilities that can measure ^{36}Cl; University of Tsukuba Tandem Accelerator Complex (UTTAC) and Micro Analysis Laboratory, Tandem Accelerator, The University of Tokyo (MALT). Miyake et al. measured ^{36}Cl in surface soils around FDNPP by AMS system in MALT and relatively high $^{36}Cl/Cl$ ratios were detected [1]. However, their results have large errors of ±20–59% and only 10 samples have been measured so far. Accordingly, measurements of more samples with smaller errors are necessary to discuss the release of ^{36}Cl in detail.

For samples in the present study, surface soils with a thickness of 5 cm were collected at 10 locations to the northwest of FDNPP from June 12 to August 1, 2013. The sample preparation scheme was designed by referring to Tamari [2], Amano [3], and Bastviken et al. [4]. The soil samples were dried at 60°C, sieved through 2 mm mesh and grinded using a mortar and pestle. The 20–40 g soil in 50 mL centrifuge tubes were subsequently frozen at −18°C and thawed at 60°C to destruct microbial cells. Adding 0.01 M HNO_3 (3 times the amount of soil) to 50 ml centrifuge tubes, the tubes were sonicated for 3 hours, centrifuged at 2000 rpm for 15 minutes and then the supernatants were pipetted to plastic bottles. Same extraction was repeated four times and all extracts were mixed. Activated carbon of 1–2 g was added to the extracts in order to remove organic sulfur and also extractable organic chlorine (Cl_{orgex}). Meanwhile, non-extractable organic chlorine (Cl_{org}) and chlorine in mineral (Cl_{min}) remained in the soil. In the extracts, only inorganic chlorine (Cl_{inorg}) existed. After shaking over 3 hours, the extracts were filtered through a 0.2 μm filter. After 10 mL aliquot was transferred to plastic bottles in order to measure stable chlorine with ion chromatography, 0-200 μL carrier prepared from halite ($^{36}Cl/Cl = 3.52\times10^{-14}$) was added to a filtrates. After adding 30% H_2O_2 (half the amount of soil) to filtrates and standing for 3 hours because of organic matter decomposition, 3 M NH_3 (0.15 times amount of soil) were added and stood for 3 hours to precipitate metal impurity as hydroxide. After filtration, the filtrates were concentrated to about 10 mL by hot plate at 80°C.

Concentrated solutions were acidified by 13 M HNO_3 and excess 0.3 M $AgNO_3$ were added. After

centrifugation (2000 rpm, 15 minutes), supernatants were removed and precipitates were dissolved in 3 M NH_3 (2 mL). 0.05 M Na_2CO_3 (2 mL) and then saturated $Ba(NO_3)_2$ (1 mL) were added in the solutions and $BaCO_3$ and $BaSO_4$ were coprecipitated and filtered through a 0.2 μm filter. Such $BaCO_3$ method, named by Tamari [2], enables effective removal of SO_4^- by coprecipitating in $[Ba^{2+}]/[CO_3^{2-}]$=2.5–7.0. In this work, the $BaCO_3$ method was repeated three times although only 0.05 M Na_2CO_3 were added at the second and the third time (respectively 1.4 mL and 0.9 mL) using remains of Ba^{2+} at the first time. After reprecipitation of AgCl by adding 13 M HNO_3 and excess 0.3 M $AgNO_3$, AgCl were redissolved by 3 M NH_3 (2 mL) and 0.05 M Na_2CO_3 (2 mL) in order to remove Ba^{2+} as an interference element of ionization at MC-SNICS (Multi Cathode-Source of Negative Ions by Cesium Sputtering). After filtering through a 0.2 μm filter, AgCl was reprecipitated and washed for three times with ultrapure water and twice with 99.5% C_2H_5OH. After drying at 110°C, the AgCl sample was used for AMS measurement of ^{36}Cl.

Measurement results of ^{36}Cl are summarized in Table 1. Before FDNPP accident, $^{36}Cl/Cl$ ratios varied in the range 0.09–1.14 ($\times 10^{-12}$) and the mean value was 0.46×10^{-12} around FDNPP [5]. However, extremely higher $^{36}Cl/Cl$ ratios are observed at NM-7 and NM-15. Furthermore, ^{36}Cl inventory at NM-17 is as large as those of NM-7 and NM-15. Consequently, the release of ^{36}Cl in FDNPP accident is evident and influence of the accident is recognized at 3 locations as far as 8 km away from FDNPP. At other locations of 8-28 km from FDNPP, there was little influence of FDNPP accident. The release of ^{36}Cl seems noticeable only around FDNPP. Further investigation is required to discuss the details.

Table 1. Summary of ^{36}Cl measurement results

Sampling spot	Cl_{inorg} concentration (ppm)	$^{36}Cl/Cl$ ratio ($\times 10^{-12}$)	^{36}Cl activity (nBq/g)	^{36}Cl inventory (mBq/m^2)	Distance from the FDNPP (km)
NM-1	14.8	1.63±0.02	29.6±0.4	1.04±0.02	28.77
NM-2	8.39	2.69±0.04	27.5±0.4	0.781±0.012	25.39
NM-5	5.59	1.49±0.02	10.2±0.1	0.389±0.005	13.36
NM-7	15.6	6.65±0.07	127±1	3.96±0.05	7.92
NM-9	16.7	0.138±0.007	2.81±0.14	0.132±0.006	8.07
NM-10	32.6	0.438±0.007	17.4±0.3	0.642±0.011	9.43
NM-11	16.9	0.964±0.014	19.9±0.3	0.810±0.012	10.94
NM-13	26.7	1.10±0.01	35.7±0.4	1.39±0.02	8.35
NM-15	8.10	6.86±0.07	67.8±0.6	2.93±0.03	7.56
NM-17	42.7	1.92±0.01	99.8±0.7	3.52±0.02	8.12

References

[1] Y. Miyake et al., Nucl. Instr. Meth. Phys. Res. B 361 (2015) 627.

[2] M. Tamari, Master's thesis, University of Tsukuba 2009 (in Japanese).

[3] T. Amano, Master's thesis, University of Tsukuba 2011 (in Japanese).

[4] D. Bastviken et al., Geochimica et Cosmochimica Acta 71 (2007) 3182.

[5] R. Seki et al., Nucl. Instr. Meth. Phys. Res. B 259 (2007) 486.

3.4 Determination of I-129 in radioactive particles by AMS

K. Matsuo, K. Sueki, T. Matsunaka, M. Matsumura, K. Sasa, T. Takahashi, S. Hosoya, A. Sakaguchi, M. Honda, R. Inaba, Y. Satou[1]

In March 2011, radioactive particles were emitted into the environment from FDNPP [1]. The particles contain various radionuclides that were produced in nuclear reactors. In this AMS study, we focused on ^{129}I which is a long-lived nuclide ($T_{1/2}$ = 1.57×10^7 years) so that its amount remains effectively unchanged since the accident. The study of ^{129}I should provide information about the behavior of short-lived ^{131}I which is also emitted at that time and is very serious for the environment. We tried to understand how iodine was incorporated into radioactive particles by determining the amount of ^{129}I in the particles.

The four sample particles were picked from the dust which was collected at the site 2 km away to the north-north west from FDNPP. Iodine species were extracted from the particles after the three steps of pretreatment of the samples, as follows.

The first step was to wash the particles by Milli-Q water. One particle with 5 mL of Milli-Q water was put in a centrifugation tube and washed in the ultrasonic cleaner (AS ONE, US-4R) for 30 minutes before the wash liquid was filtrated through 0.2 μm filter.

The second step was extraction by 25% tetramethylammonium hydroxide (TMAH) aqueous solution (TAMACHEMICALS, TAMAPURE-AA). The particle after the first step was put in the vessel for the microwave digestion apparatus (BERGHOF, speedwave4) with 5 mL of TMAH aq. After entering the vessel into the machine, the particle was irradiated by microwaves at 90 W for 3 hours and we took out the solution.

The third step was thermal hydrolysis using the tube furnace. The particle passed through the first and second steps was placed on a ceramic boat. Subsequently, the boat was heated in the tube furnace in which moisture-containing oxygen flowed at 990°C for 30 minutes and a solution for trapping iodine was fitted on the discharge side of the tube with an L-shaped tube at that time. This solution was composed of 6.1 mL of Milli-Q water, 800 μL of 25% TMAH aq. and 100 μL of 2% Na_2SO_3 aq. After finished heating, the whole solution including the wash liquid of the L-shaped tube made to 10 mL. Also, blank samples were made in all the steps.

Each of the first-, second-, and third-step samples were fractionated into a half, 1/10 and 1/100, respectively, and NaI aq. as carrier (2 mg of I) was added to each of these samples. And then, purification of iodine, treatment of AgI, and the AMS measurements were carried out in accordance with the condition by Matsunaka et al. [2, 3] .

The amount of ^{129}I was determined from the result of ^{129}I / ^{127}I by Matsuzaki et al [4]. In the reference document, the amount of ^{127}I in the sample was determined by ICP-MS and is considered when calculating the amount of ^{129}I. However, the density of iodine of the particles was estimated to be

[1] Japan Atomic Energy Agency (JAEA)

under 50 ppm because iodine was undetected by the elemental analysis of BL37XU at SPring-8 [5]. Therefore, the amount of ^{127}I in the particle was neglected since it was much smaller than that in the carrier. The numbers of ^{129}I per one particle was calculated by summing up second and third steps. Finally, we obtained the activity of ^{129}I, the number of atoms, the activity of ^{129}I and the activity ratio of ^{129}I / ^{137}Cs (Bq/Bq) per one particle on March 11, 2011.

The results are shown in Tables 1 and 2. Table 1 shows the numbers of ^{129}I atoms in the samples at each step and Table 2 shows the numbers of ^{129}I atoms, their activity, and ^{129}I / ^{137}Cs (Bq/Bq) per one particle at the time of the occurrence of the accident. It is presumed that some amounts of ^{129}I have come out from the surface of particles by ultrasonic cleaning. The extraction by TMAH aq. seems to be meaningful because 5 – 26% of the whole amounts of ^{129}I were extracted by this step. Furthermore, the average of ^{129}I / ^{137}Cs of the four particles (2.9×10^{-9}) is smaller than that of the sampled soil [$(4.3\pm0.1)\times10^{-7}$] by two orders of magnitude. Therefore, it is presumed that the behavior of I and Cs absorbed into particles is different from that of singly emitted Cs and I.

Table 1. Number of ^{129}I atoms in the samples at each step

Names of particles	Washing by milli-Q	Extraction by 25% TMAH aq.	Thermal hydrolysis
CF-01M02	$5.04\pm0.16\times10^{7}$	$3.33\pm0.07\times10^{8}$ (26%)	$1.24\pm0.06\times10^{9}$ (74%)
CF-01M06	$6.91\pm0.59\times10^{6}$	$1.64\pm0.05\times10^{8}$ (9%)	$1.99\pm0.12\times10^{9}$ (91%)
CF-01M08	$4.11\pm0.13\times10^{7}$	$2.75\pm0.08\times10^{8}$ (23%)	$9.13\pm0.05\times10^{8}$ (77%)
CF-01M15-1	$1.91\pm0.05\times10^{8}$	$5.83\pm0.30\times10^{7}$ (5%)	$1.08\pm0.06\times10^{9}$ (95%)

Table 2. Number of ^{129}I atoms, their activity, and ^{129}I / ^{137}Cs (Bq/Bq) at the time of the accident

Names of particles	Number of atoms	Activity (Bq)	^{129}I / ^{137}Cs (Bq/Bq)
CF-01M02	$1.29\pm0.08\times10^{9}$	$1.80\pm0.11\times10^{-6}$	$5.79\pm0.45\times10^{-9}$
CF-01M06	$1.87\pm0.13\times10^{9}$	$2.61\pm0.18\times10^{-6}$	$3.64\pm0.32\times10^{-9}$
CF-01M08	$1.19\pm0.05\times10^{9}$	$1.66\pm0.08\times10^{-6}$	$1.17\pm0.08\times10^{-9}$
CF-01M15-1	$1.14\pm0.06\times10^{9}$	$1.60\pm0.08\times10^{-6}$	$1.03\pm0.06\times10^{-9}$

References

[1] K. Adachi et al., Sci. Rep. 3 (2013) 2554.

[2] T. Matsunaka et al., Nucl. Instr. Meth. B 361 (2015) 569.

[3] Y. Muramatsu et al., Quat. Geochronol 3 (2008) 291.

[4] H. Matsuzaki et al., Nucl. Instr. and Meth. B 123 (2007) 721.

[5] M. Suzuki et al., SPring-8 Users Info. 16 (2011) 201 (in Japanese).

3.5 Preparation of a ^{129}I standard solution for ICP-MS/MS

M. Honda, K. Sasa, T. Takahashi, T. Matsunaka, S. Hosoya, M. Matsumura, K. Sueki

A large amount of ^{129}I (physical half-life: 15.7 Myr) has been introduced into the terrestrial environment through nuclear weapons' tests, spent nuclear fuel reprocessing operations, and nuclear accidents. The study of anthropogenic ^{129}I is of increasing concern in Japan from the viewpoint of a radiation risk assessment. AMS have been commonly used for the ^{129}I analysis, but the latest triple quadrupole ICP-MS (ICP-MS/MS) is becoming an alternative analysis. ICP-MS/MS provides a high sample throughput and optimum way for the analysis of high-level ^{129}I (^{129}I/^{127}I> 10^{-8}) which is hard to deal with AMS [1]. Absolute ICP-MS/MS measurements require reliable standards for calibration. In this fiscal year, the ^{129}I/^{127}I ratio of a home-made standard solution for ICP-MS/MS was evaluated with 6MV AMS at UTTAC.

The ^{129}I standard solution "tRIC-1" was prepared from a stored ^{129}I solution (^{127}I and ^{129}I concentrations are 1 mg/mL and 0.448 Bq/mL, respectively) with 2% tetramethyl ammonium hydroxide solution (Tama Chemicals). The stable iodine (^{127}I) concentration in tRIC-1 was determined by ICP-MS/MS to be 9.95 ± 0.10 ppm. A portion of 100 mL tRIC-1 was mixed with 698 mg iodine carrier (Orion Ionplus, Thermo scientific, which has ^{129}I/^{127}I = 1.80 × 10^{-13} [2]) and then precipitated as silver iodide (AgI). The precipitated AgI was divided into five batches and the five targets prepared from each batch were measured. The ^{129}I/^{127}I ratios were all normalized using the standard material provided by PRIME Lab. at Purdue University (nominal value is 6.54 × 10^{-12}). In AMS, the charge state of 5+ was chosen for the terminal voltage of 5 MV. The ^{129}I/^{127}I ratio in tRIC-1 was calculated from the AMS and ICP-MS/MS results.

A good reproducibility was obtained in the ^{129}I AMS measurements, as shown in Fig. 1. The ^{129}I/^{127}I ratios of tRIC-1 range from (5.93 ± 0.16) × 10^{-5} to (6.40± 0.05) × 10^{-5}. The ^{129}I/^{127}I ratio is evaluated as the averaged value for the five batches, i.e., (6.20 ± 0.18) ×10^{-5}.

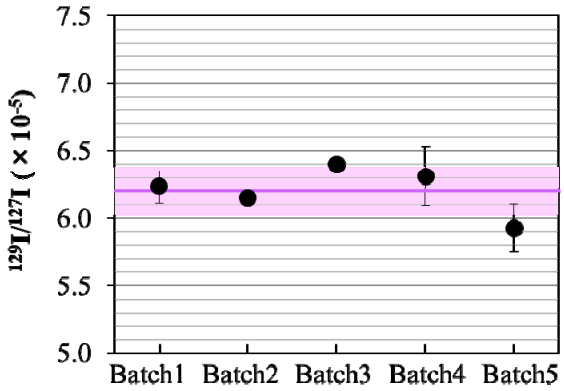

Fig. 1. ^{129}I/^{127}I ratios in a home-made standard solution.

References

[1] T. Ohno andY. Muramatsu, J. Anal. At. Spectrom. 29 (2014) 347.

[2] H. Matsuzaki et al., Nucl. Instr. Meth. B 259 (2007) 721.

3.6 Performance evaluation of the AMS-measurement of iodine-129 by the 6 MV tandem accelerator at University of Tsukuba

M. Matsumura, K. Sasa, T. Matsunaka, T. Takahashi, S. Hosoya, Y. Satou[1], K. Sueki

A multi-nuclide AMS system for ^{10}Be, ^{14}C, ^{26}Al, ^{36}Cl, ^{41}Ca, and ^{129}I is now available at UTTAC [e.g., 1, 2]. This report focuses on the performance of ^{129}I measurement for near-future development of the standard reference materials of ^{129}I. The ^{129}I measurement conditions of the accelerator were as follows; injected ion species of I^-, the terminal voltage of 5.0 MV, and the analyzed ions of 30MeV I^{5+}. Isobutane gas of 19 Torr was used for the gas-ionization detector with an entrance window of a 1.5-μm thick polyester film. The ^{129}I standard reference materials, Z94-0596 and Z94-0597, named Purdue1 and Purdue 2, respectively, were provided by PRIME Lab., Purdue University [3, 4].

The ratios of ^{129}I/^{127}I were measured in the experiments. The measured ratio for Purdue 1 is $(8.29 \pm 0.08) \times 10^{-12}$ against the consensus ratio of 8.38×10^{-12} with a precision error of 1.1% , while for Purdue 2 the measured ratio is $(6.54 \pm 0.03) \times 10^{-11}$ against the consensus ratio of 6.54×10^{-11} with a precision error of 0.5%. These results thus indicate good agreement, including the precision errors, between the measured and consensus values. Figure 1 shows consistency between the two values, which demonstrates that the present experimental setup and the method of analysis are reasonable.

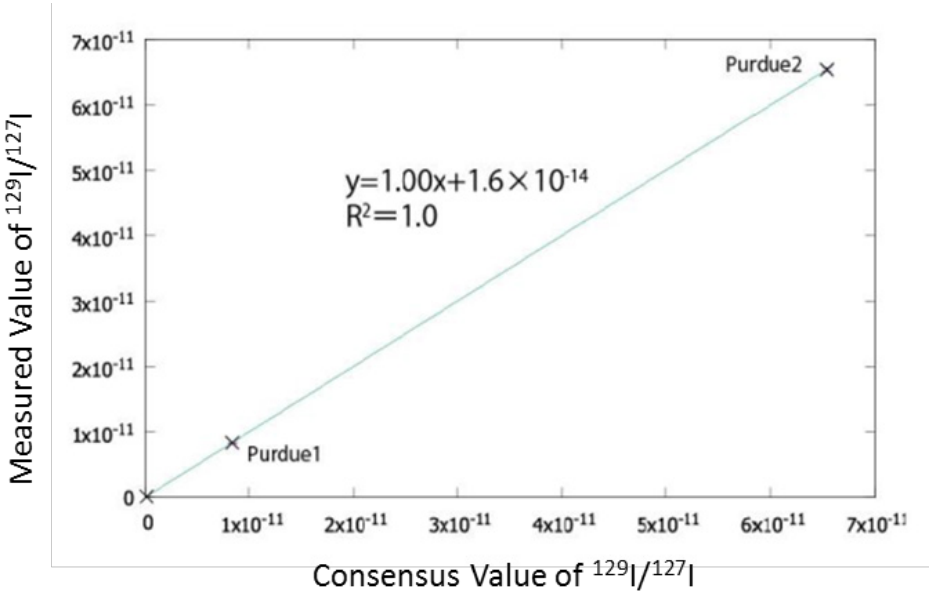

Fig. 1. Comparison between the measured and the consensus ratios of ^{129}I/^{127}I for the ^{129}I standard reference materials.

Figure 2 shows dependence of the beam current and transmission of ^{129}I on the mixing ratio of the Nb-powder to the target AgI of Purdue 2. We see that the maximum beam current, i.e., the optimum mixing ratio is given at Nb:AgI＝4：1, as is generally proposed. Figure 3 shows the results of blank

[1] Japan Atomic Energy Agency

measurements. ”Old Iodine” provided from DeepWater corporation has the extremely low background level of the $^{129}I/^{127}I$ ratio as low as 1×10^{-14}. Therefore, the machine background is estimated to be as low as on the order of 10^{-15} in the value of $^{129}I/^{127}I$.

This work was supported by JSPS KAKENHI Grant Number 15H02340.

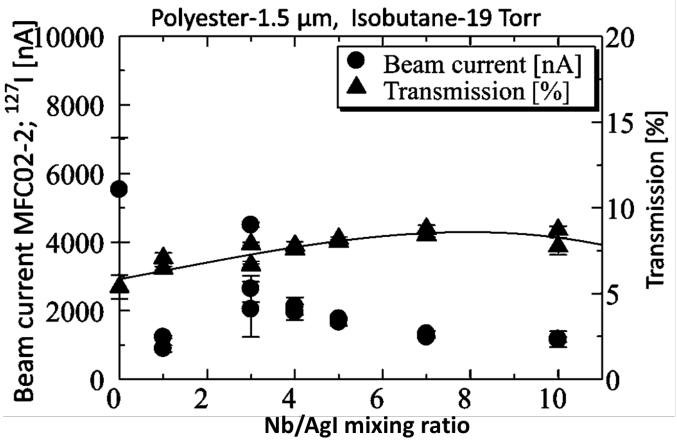

Fig. 2. Dependence of beam current and transmission of ^{129}I standard reference materials on the Nb/AgI mixing ratio.

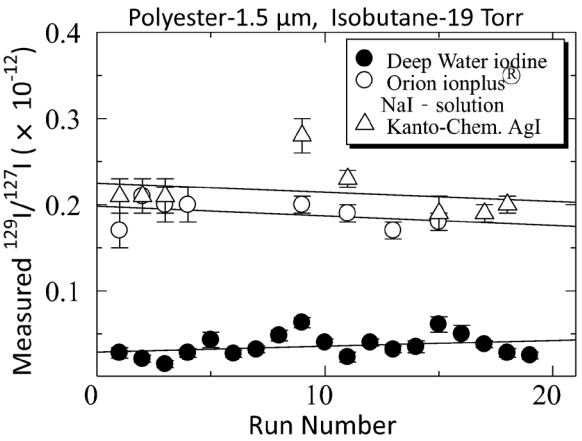

Fig. 3. Measured $^{129}I/^{127}I$ ratios for various blanks.

References

[1] K. Sasa et al., Nucl. Instr. Meth. Phys. Res. B 361 (2015) 124.

[2] S. Hosoya et al., Nucl. Instr. Meth. Phys. Res. B (2017) in press.

[3] P. Sharma, et al., Nucl. Instr. Meth. Phys. Res. B 123 (1997) 347.

[4] H. Matsuzaki, et al., Nucl. Instr. Meth. Phys. Res. B 361 (2015) 63.

3.7 Reconstruction of temporal variation for anthropogenic radionuclides in the Japan Sea using a coral core sample

R. Inaba, A. Sakaguchi, T. Nomura[1], H. Yamano H[2], K. Sasaki K[3], T. Watanabe[4], M. Honda, K. Sasa, T. Matsunaka, S. Hosoya, T. Takahashi, M. Matsumura, K. Sueki

Due to recent improvements in instrumentation and chemical pretreatments, Iodine-129 (^{129}I; $T_{1/2}$=1.57×10^7 y) is increasingly being used as an oceanic circulation tracer instead of the short half-life artificial nuclide, ^{137}Cs. ^{129}I is a long-lived anthropogenic radionuclide that is introduced to the earth surface environment, mainly by atmospheric nuclear tests and/or nuclear-related facilities. However, ^{129}I input history to "the miniature ocean", the Japan Sea, has not been clarified. In this study, the input history of ^{129}I to the surface water of the Japan Sea has been reconstructed through measurement of ^{129}I/^{127}I atom ratios in a coral sample collected from Iki Island; the main entrance of surface water to the Japan Sea.

The coral core sample (*Dipsastraea speciosa*) was collected in November 2012 from a depth of 3 m at Kurosaki, Iki Island (N33° 48'22.5, E129° 40'02.9). The annual growth bands were confirmed by X-ray imaging and Sr/Ca analysis with laser ablation (LA)-ICP-MS for coral slabs, and the coral sections were cut into annual segments in accordance with the X-ray image and the variation of the Sr/Ca ratios. The ^{129}I/^{127}I in each annual ring was measured by AMS after appropriate sample preparation.

The ^{129}I/^{127}I atom ratios were reconstructed over a wide range of (0.145–71.3)×10^{-12}. It was observed that the ratio drastically increased in the early1950s, and has high values even now. It may be presumed that airborne ^{129}I, which is released from nuclear-related facilities, has been constantly absorbed by the surface seawater around this area. The recent atom ratios found in the surface water of the Japan Sea are higher than those of Guam [1], Baler in the Philippines [2]. It was also observed that the reconstructed ^{129}I/^{127}I atom ratios show different variations than for ^{236}U/^{238}U ratios that were constructed from the same coral core sample [3].

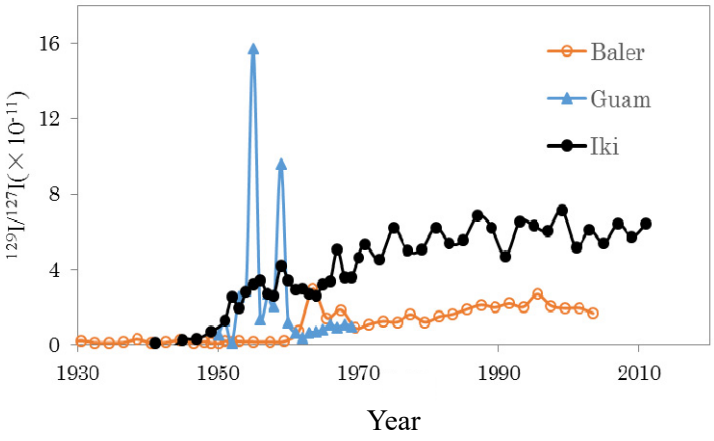

Fig.1. Variations of ^{129}I/^{127}I atom ratios reconstructed from the annual rings in the coral cores from Guam [2], Baler [1] and Iki Island (this study).

References

[1] C. Chang et al., J. Environ. Radioact. 165 (2016) 144.
[2] A. T. Bautisata et al., J. Environ. Radioact. 164 (2016) 174.
[3] A. Sakaguchi et al., J. Geophys. Res. Oceans 121 (2016) 4.

[1] Graduate School of Science, Hiroshima University
[2] National Institute for Environmental Studies
[3] Kanazawa Gakuin University
[4] Faculty of Science, Hokkaido University

3.8 Radiocarbon variations since 1960 in tree rings near the Tokai nuclear facilities in Japan

T. Matsunaka, K. Sasa, T. Takahashi, S. Hosoya, M. Matsumura, K. Sueki, Y. Satou[1]

Tokai area in Ibaraki Prefecture is located 1.8 km south-southwest of the Tokai Nuclear Power Plants (Tokai NPP and Tokai-2 NPP) and 1.4 km North-Northwest of the Tokai Reprocessing Plant (Tokai RP). To evaluate the environmental impact of the atmospheric ^{14}C discharge from the Tokai nuclear facilities, a 80-year-old pine tree grown at Tokai area was cored and ^{14}C in each annual ring was measured using the AMS system at UTTAC. The terminal voltage of 5.0 MV and the charge state of 4+ were chosen for acceleration and detection of ^{14}C. The measurement error of the system was ±0.3% for NIST-4990C (HOx-II), and the blank levels were 0.04–0.09 pMC (55,950–63,300 yrBP) for IAEA-C1 (Marble). The ^{14}C specific activities varied from 232.8 Bq kg^{-1} C to 403.3Bq kg^{-1} C in the tree rings formed during the period 1959–2013. The specific activities in 1967–2010 are significantly elevated compared with the ambient background values, clearly indicating ^{14}C discharges from the Tokai nuclear facilities during their normal operation. The excess ^{14}C activities of 0.48–70 Bq kg^{-1} C in 1965–2011, shown in Fig.1, are positively correlated with the estimated annual ^{14}C discharges of 0.02–2.0 TBq from Tokai NPP (operational period: 1966–1997), Tokai-2 NPP (operational period: 1978–2010) and Tokai RP (operational period: 1977–2007) with R^2 of 0.72 (n = 38), as shown in Fig.2. These activity values of < 70.0 Bq kg^{-1} C are corresponding to an additional annual effective dose of < 3.9 μSv via the food ingestion pathway in the location studied.

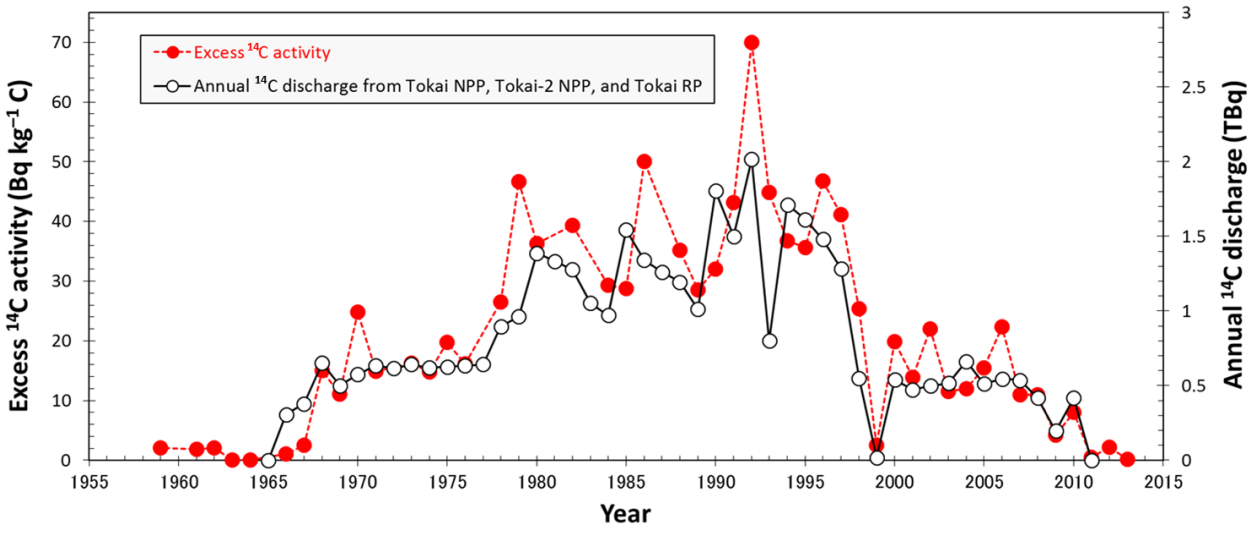

Fig. 1. Red circles: the variations of excess ^{14}C activity in the Tokai tree rings. White circles: estimated annual ^{14}C discharge from Tokai NPP, Tokai-2 NPP, and Tokai RP [1], calculated by multiplying the ^{14}C emission factors for NPP [5.5 TBq W^{-1} for Magnox GCR (Tokai NPP) and 0.51 TBq W^{-1} for BWR (Tokai-2 NPP)] [2, 3] by the annual electrical energy output [4].

[1] Collaborative Laboratories for Advanced Decommissioning Science, JAEA

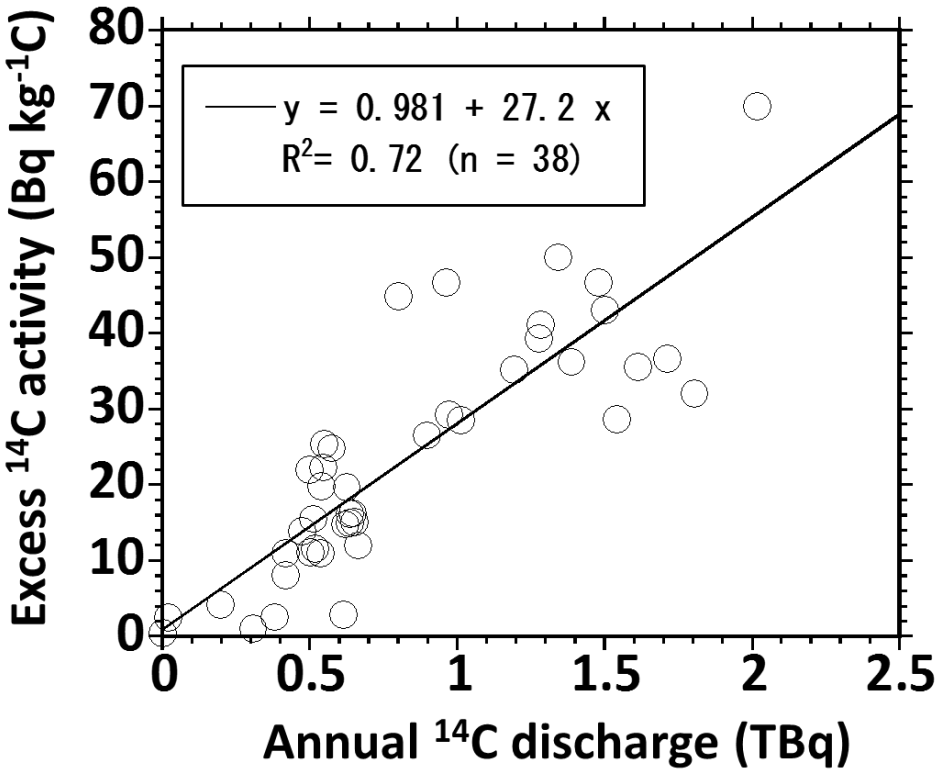

Fig. 2. The correlation between excess ^{14}C activity in the Tokai tree rings and estimated annual ^{14}C discharge from Tokai NPP, Tokai-2 NPP, and Tokai RP. The linear regression line and coefficient of determination (R^2) are shown in the correlation diagram.

References

[1] J. Koarashi et al., J. Nucl. Sci. Technol. 53 (2016) 546.

[2] UNSCEAR, Exposures to the Public from Man-made Sources of Radiation, vol. 1 (2000).

[3] H. D. Graven and N. Gruber, Atmos. Chem. Phys. 11 (2011) 12339.

[4] IAEA (2016), http://www.iaea.org/PRIS/CountryStatistics/CountryStatisticsLandingPage.aspx.

3.9 Trial of determination of ^{41}Ca concentration in iron meteorites by accelerator mass spectrometry

Y. Oura[1], N. Kuroiwa[1], M. Matsumura, S. Hosoya, T. Takahashi, K. Sasa

Cosmogenic radionuclides ^{36}Cl and ^{41}Ca are found in meteorites, which are produced by several nuclear reactions such as proton and secondary-neutron induced spallation reactions and neutron capture reactions. To study irradiation histories of meteorites, accelerator mass spectrometry (AMS) for both of the two radionuclides is required. However, the former AMS system at UTTAC allowed measurements of only ^{36}Cl concentrations [1]. In 2016, UTTAC started operation of the new AMS system for measurements of several radionuclides including ^{41}Ca. We therefore tried to determine ^{41}Ca concentration in iron meteorites by applying the new AMS system.

Using a radiotracer, a chemical separation procedure for Ca in iron meteorites was evaluated especially for a pH condition in separation of Ca from Fe. The evaluation procedure was applied to two iron meteorites, Gibeon and Campo del Cielo meteorites, in which ^{36}Cl concentrations were determined by the former AMS system at UTTAC [1]. Each piece of about 1 g was cut out from the same fragment for previous ^{36}Cl determination. After dissolution in HNO_3 with Ca and Cl carriers (about 4 mg each), $AgNO_3$ was added to precipitate AgCl. Ammonia water was added to the supernatant solution to make pH 5.4 – 5.8, and then $Fe(OH)_3$ was precipitated. Then, CaC_2O_4 was precipitated by adding $(NH_4)_2C_2O_4$ in the supernatant solution followed by dissolution of CaC_2O_4 in 6 mol/L HCl. Remained trace of Fe in this solution was removed by anion exchange method, and then CaF_2 was finally obtained by adding HF to the eluate containing Ca. The AgCl was purified in several steps. Final Ca and Cl fractions were divided into halves, and both half portions were subjected to AMS measurement independently.

In AMS with the terminal voltage of the tandem accelerator set to 6 MV, $^{41}Ca^{7+}$ and $^{40}Ca^{7+}$ in ^{41}Ca standard samples were measured for about 3000 sec (10×300 sec) by a gas ionization detector and a Faraday cup, respectively. The calibration curve obtained, shown in Fig. 1, demonstrates good correlation between ^{41}Ca/^{40}Ca count ratio and certified ^{41}Ca/Ca atomic ratio. According to the calibration curve, down to about 0.5×10^{-13} of ^{41}Ca/Ca are found to be detectable at least under the condition in this study. The results for iron meteorites are tabulated in Table 1. For Campo del Cielo meteorite, in which ^{36}Cl concentration is 2.38 ± 0.01 dpm/kg [1], 30 – 50 counts of ^{41}Ca

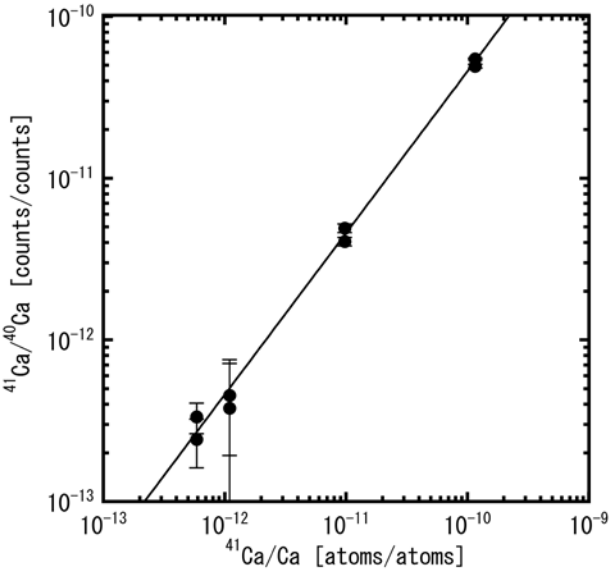

Fig. 1. Calibration curve for ^{41}Ca obtained by measurement of ^{41}Ca standard samples.

[1] Tokyo Metropolitan University

was observed. Although the observed count of ^{41}K was larger than that of ^{41}Ca, ^{41}Ca was sufficiently discriminated from ^{41}K on the two-dimensional spectra. Concentrations of ^{41}Ca for two portions of Campo del Cielo are consistent within their uncertainties. Content of ^{41}Ca was estimated based on the combination of the determined ^{36}Cl concentration and a model calculation by Ammon et al. [2]. The determined ^{41}Ca concentrations in Campo del Cielo were in agreement with a range of estimated concentration, which assures the accuracy of the present ^{41}Ca determination. On the contrary, ^{41}Ca concentration determined for Gibeon meteorite, in which ^{36}Cl concentration determined is 0.019 ± 0.001 dpm/kg [1], is about 10 times larger than the estimated concentration. According to the calibration curve, no count of ^{41}Ca is estimated to be observed for the estimated ^{41}Ca concentration. Thus the observed ^{41}Ca of 2 counts is probably due to ^{41}K. For 1 g of iron meteorite and 2 mg of Ca carrier, the concentration down to about 0.02 dpm/kg is found to be detectable.

Table 1. Results for iron meteorites.

		Measurement time [s]	Count of ^{41}Ca	Atomic ^{41}Ca/Ca [$\times 10^{-12}$]	^{41}Ca [dpm/kg]	Estimated ^{41}Ca [dpm/kg]	Count of ^{41}K
Gibeon	A	2650	2	0.57	0.38 ± 0.30	0.020 - 0.046	337
	B	2469	0	-	-		287
Campo del Cielo	A	2441	47	4.5	3.9 ± 0.6	2.6 - 5.8	350
	B	2072	32	3.4	2.9 ± 0.6		95

References

[1] Y. Oura et al., UTTAC Annual Report 2010 (2012) 42.

[2] K. Ammon et al., Meteoritics and Planetary Science 44 (2009) 485.

4.

BEAM AND ISOTOPE APPLICATIONS

4.1 Probing the effect of point defects on the leakage blocking capability of $Al_{0.1}Ga_{0.9}N$/Si structures using a monoenergetic positron beam

A. Uedono, M. Zhao[1], E. Simoen[1,2]

Vacancy-type defects in $Al_{0.1}Ga_{0.9}N$ were probed using a monoenergetic positron beam. $Al_{0.1}Ga_{0.9}N$ layers with different carbon doping concentrations ([C] = 5 × 10^{17}–8 × 10^{19} cm^{-3}) were grown on Si substrates by metalorganic vapor phase epitaxy. The major defect species in $Al_{0.1}Ga_{0.9}N$ was determined to be a cation vacancy (or cation vacancies) coupled with nitrogen vacancies and/or with carbon atoms at nitrogen sites (C_{NS}). The charge state of the vacancies was positive because of the electron transfer from the defects to C_N-related acceptors. The defect charge state was changed from positive to neutral when the sample was illuminated with photon energy above 1.8 eV, and this energy range agreed with yellow and blue luminescence. For the sample with high [C], the charge transition of the vacancies under illumination was found to be suppressed, which was attributed to the trapping of emitted electrons by C_N-related acceptors. With increasing [C], the breakdown voltage under the reverse bias condition increased. This was explained by the trapping of the injected electrons by the positively charged vacancies and C_N-related acceptors. Results are shown in the following Figs. 1-8 [1].

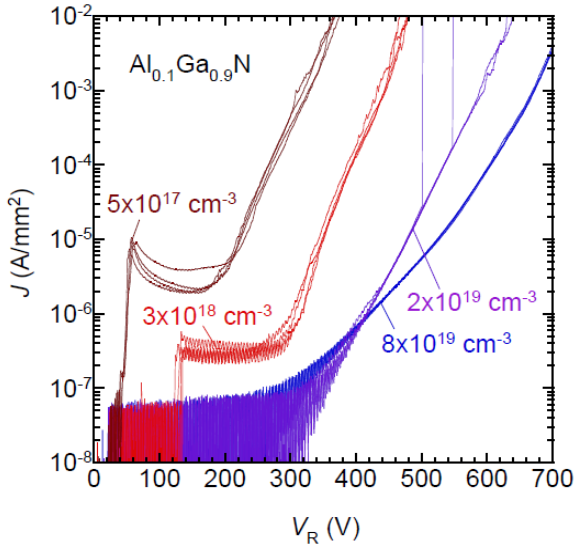

Fig. 1. Current density J and reverse bias voltage V_R characteristics for $Al_{0.1}Ga_{0.9}N$ with different carbon concentrations ([C] = 5 × 10^{17}–8 × 10^{19} cm^{-3}).

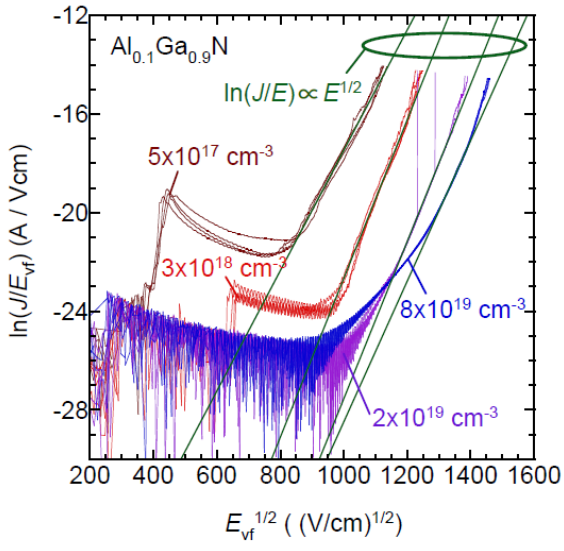

Fig. 2. Relationship between $\ln(J/E_{vf})$ and $E_{vf}^{1/2}$ for $Al_{0.1}Ga_{0.9}N$ with [C] = 5 × 10^{17}–8 × 10^{19} cm^{-3}.

[1] Imec, Leuven, Belgium
[2] Ghent University, Ghent, Belgium

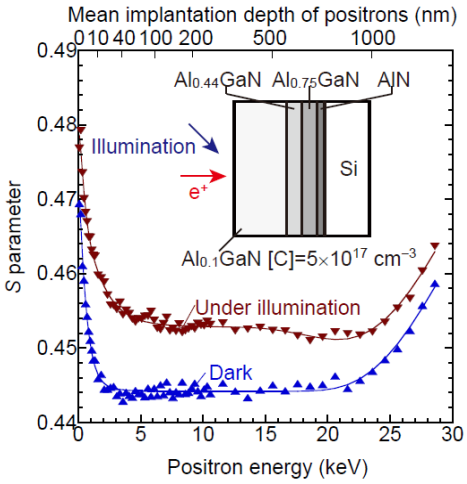

Fig. 3. *S* parameters as a function of incident positron energy *E* for $Al_{0.1}Ga_{0.9}N$ with [C] = 5×10^{17} cm^{-3}. The measurement was done in the dark and under illumination of He-Cd laser light. The inset shows the layer structure of the sample.

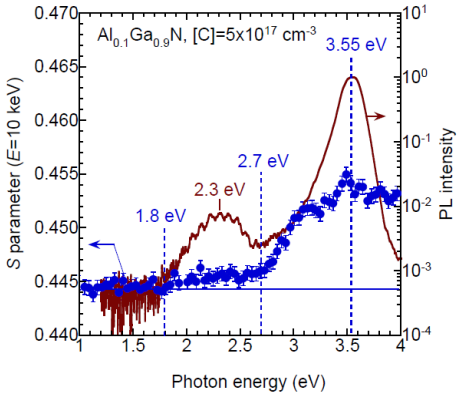

Fig. 5. Relationship between the *S* value and the photon energy for $Al_{0.1}Ga_{0.9}N$ with [C] = 5×10^{17} cm^{-3}. During the measurement, the value of *E* was set to 10 keV. The PL spectrum obtained at room temperature is also shown.

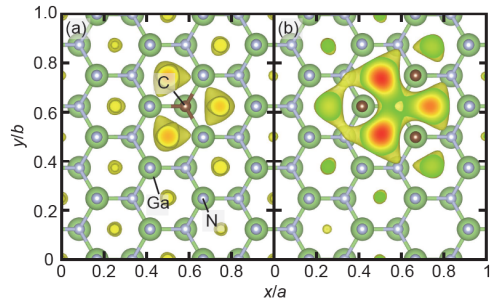

Fig. 7. Distributions of the positron density around (a) C_N and (b) $(C_N)_4$. Green, gray, and brown circles correspond to Ga, N, and C, respectively. The positron density increases following the color scale as "green → yellow → red".

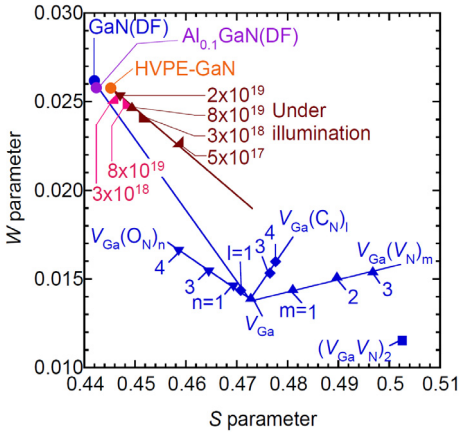

Fig. 4. Relationship between *S* and *W* corresponding to the positron annihilation in $Al_{0.1}Ga_{0.9}N$ measured with and without He-Cd laser illumination. The values of [C] in $Al_{0.1}Ga_{0.9}N$ are shown in the figure. The result for HVPE-GaN is also shown. The simulated (*S*,*W*) values corresponding to the annihilation of positrons in the delocalized state (DF) and those of positrons trapped by vacancy-type defects in GaN are also shown in the same figure.

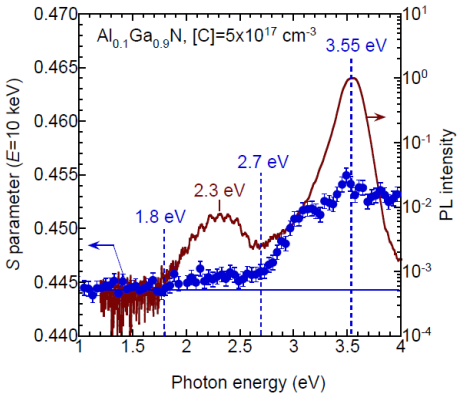

Fig. 6. (a) FWHM values of $Al_{0.1}Ga_{0.9}N$ (002) and (102) peaks obtained from XRD ω-rocking curves, (b) the breakdown voltage under reverse bias, $V_{BD(R)}$, and (c) the *S* values at *E* = 10 keV as a function of [C].

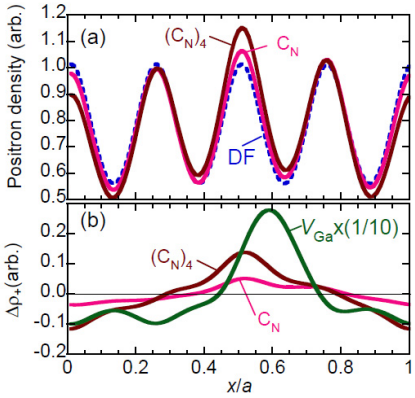

Fig. 8. (a) Planar averaged positron densities for C_N, $(C_N)_4$, and DF-GaN. The differences between the positron densities for C_N-related defects and DF-GaN, $\Delta\rho_+$, are shown in (b), where the results for V_{Ga} (multiplied by 1/10) is also shown.

Reference

[1] A. Uedono et al., J. Appl. Phys. 120 (2016) 215702 (1-7).

4.2 Study of cathode shape effect on the reliability of Δ*E*-*E* telescope ERDA

I. Harayama, Y. Hirose[1], H. Matsuzaki[2], D. Sekiba

The partial replacement of anions in metal oxides has been studied intensively. The continuous control of anion composition, such as the ratio of O/N, enables us to tailor their optical, electronic and structural properties. For these studies, we developed a beam line for Δ*E*-*E* telescope ERDA (elastic recoil detection analysis) to determine the compositional ratio of O/N [1]. The developed beam line worked well to study amorphous ZnO_xN_y films [2] and epitaxial CoO_xN_y films [3]. Our Δ*E*-*E* telescope ERDA consists of a gas ionization chamber, which measures the energy loss of recoiling particles passing through the P10 gas, and a solid state detector (SSD) for measuring their residual energies. The gas ionization chamber has the anode, the Frisch grid and the U-shaped cathode, see Fig. 1 (a), designed by referring to the literature on accelerator mass spectrometry [4]. In this work, we investigated influence of inhomogeneous electric field due to the U-shaped cathode on the reliability of Δ*E*-*E* telescope ERDA.

Ideally, a gas ionization chamber collects all the electrons from the generated ion-electron pairs by applying the sufficient electric field between the cathode and the Frisch grid. However, either weak or too strong electric field can often cause a counting loss of the electrons. This is because the former allows the recombination of the ion-electron pairs, while the latter induces the capture of electrons by the Frisch grid. Figures 1 (a) and (b) show the electrostatic potentials calculated by SIMION. We see in Fig. 1 (a) that the electric field is very weak at the position (B), while it is very strong at the position (C). These heterogeneities of the electric field by the U-shaped cathode might lead to ambiguities of the signal intensity.

To estimate the influence of the cathode shape on the experiments, we adopted the $SrTiO_3$ thick film as a reference sample for Δ*E*-*E* telescope ERDA. The target was irradiated with probe ions of 38.4 MeV $^{35}Cl^{7+}$. The incident angle of the ions was 75° from the surface normal of the target. The recoil angle was 30° from the incident direction of the ions. Figures 2 (a) and (b) show the two-dimensional ERDA histograms taken by the gas ionization chamber with the U-shaped and the planar cathodes, respectively. From Figs. 2 (a) and (b), we see that the Δ*E* intensities of the O and Cl curves measured using the U-shaped cathode are 20% lower than those measured using the planar cathode. In both measurements, the experimental conditions such as the P10 gas pressure and the applied voltages to the electrodes were the same. This result implies that the electrons were partly lost with the U-shaped cathode.

Subsequently, we investigated how such an electron loss affects the quantitative analysis of elemental compositions. If this phenomenon significantly causes the counting loss of the recoiling or scattered particles, a major change in the design of the apparatus is necessary. Figure 3 shows energy spectra of the recoiling O, which is reproduced from Figs. 2 (a) and (b). The data were taken under the same beam dose. In Fig. 3, we see no significant difference between the two spectra within the statistical uncertainty. This implies that the lower Δ*E* for the U-shaped cathode does not result from the counting

[1] Graduate School of Science, The University of Tokyo
[2] School of Engineering, The University of Tokyo

loss of electrons, but probably from the complicated orbitals of electrons induced by the inhomogeneous electric field.

In conclusion, the two types of cathode can be used safely so that we reconfirmed the validity of the data previously taken with the U-shaped cathode [2, 3]. However, we should use the planar cathode to remove the ambiguity in the experimental and analytical procedures.

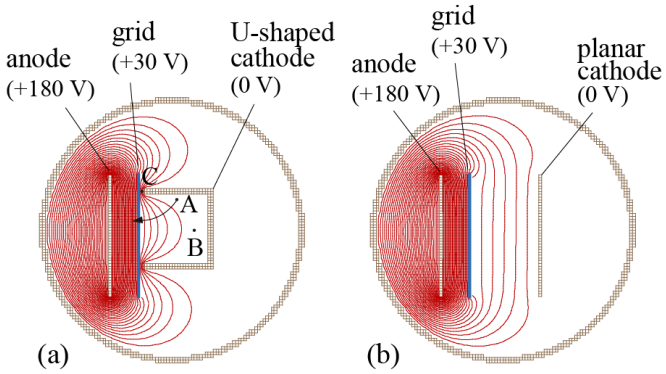

Fig. 1. Calculated electrostatic potentials in the gas ionization chambers with (a) the U-shaped cathode, and (b) the planar cathode. The red lines indicate equipotential lines with an interval of 5V.

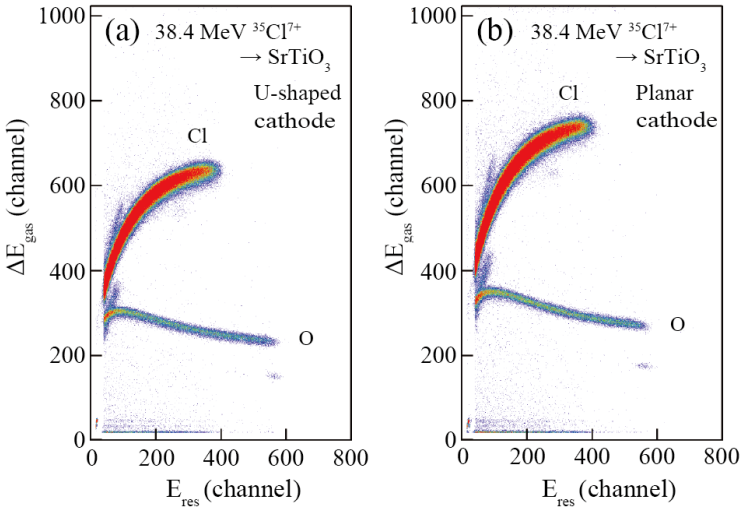

Fig. 2. Two-dimensional ERDA histograms taken by the gas ionization chamber with (a) the U-shaped cathode, and (b) the planar cathode. The target is the $SrTiO_3$ thick film.

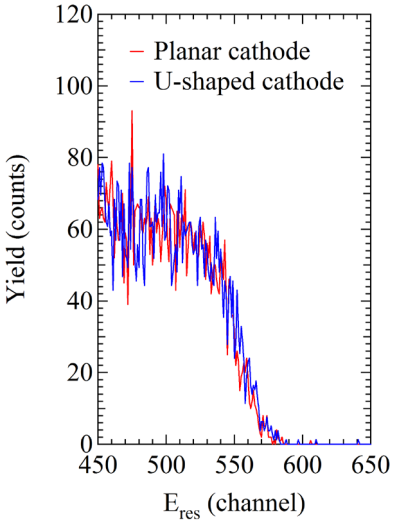

Fig. 3. Energy spectra of recoiling O, reproduced from Fig. 2. The blue and red lines indicate the data taken by the U-shaped cathode and the planar cathode, respectively.

References

[1] I. Harayama et al., Nucl. Instr. Meth. Phys. Res. B 384 (2016) 61.

[2] T. Yamazaki et al., Appl. Phys. Lett. 109 (2016) 262101.

[3] J. Takahashi et al., Appl. Phys. Lett. 107 (2015) 231906.

[4] H. Matsuzaki et al., Nucl. Instr. Meth. Phys. Res. B 172 (2000) 218.

4.3 Trial production of preamplifier for multi-channel SSD

K. Tsujita, Y. Sugisawa, I. Harayama, Y. Watahiki, D. Sekiba

Recently we developed a high-resolution elastic recoil detection analysis (HERDA) system at D-course in 1MV Tandetron accelerator at UTTAC, similar to that made by Kimura's group [1], and determined the detection limit of the system for hydrogen using hydrogenated amorphous carbon films (a-C:H) on Si wafers [2]. The detection limit obtained was ~3.8×10^{20} atoms/cm^3 in a bulk, while ~1.2×10^{13} atoms/cm^2 at an interface. These values are not sensitive enough to investigate hydrogens at an interface between, for example, Si and Si oxides. We have therefore tried to improve the sensitivity of hydrogen detection in thin films or interfaces between semiconductors and their oxides.

The detection limit of such an apparatus is determined by the signal to noise ratio. In our HERDA system, the noises stem mainly from the dark current in the position sensitive detector (PSD) composed of micro-channel plate (MCP) and from the stray particles scattered from the vacuum chamber walls. To distinguish the recoiling hydrogen from the stray particle, we have tried to use PSD composed of solid state detectors (SSD). We used a strip-type passivated implanted planar Si (PIPS) detector with sixteen channels provided by CANBERRA Industries. The width of the one pad of the strip is ~4 mm, so that the total dimension of the detector is ~75 mm.

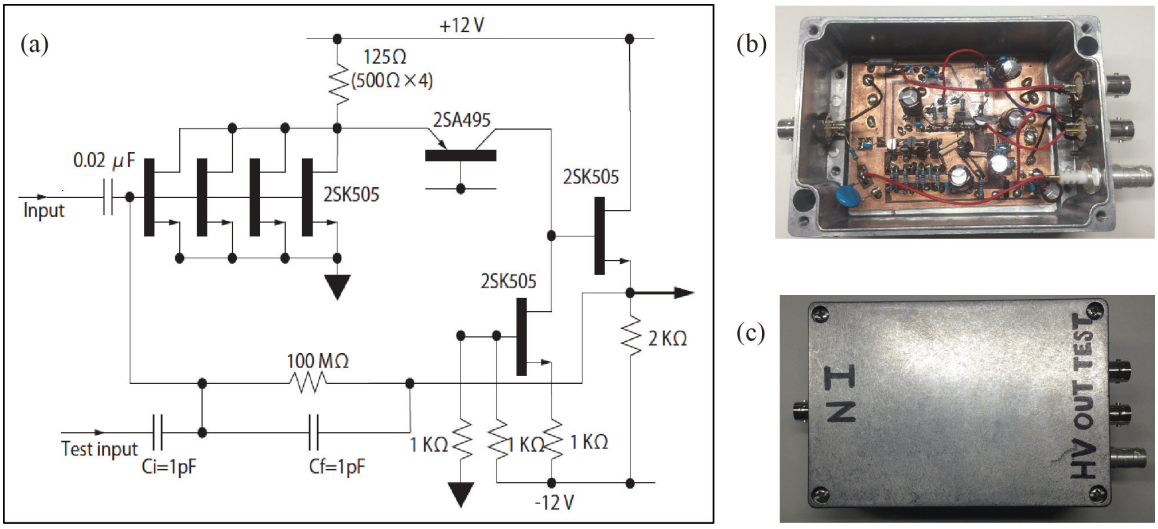

Fig.1. (a) The circuit used in the present work, which is based on Ref. [3]. Some trivial pass-condensers are removed from the schematics. (b) Inside of the trial product. (c) External appearance of the trial preamplifier.

In the current HERDA system, the position signal generated from PSD is inherently the energy signal of the detected particles. By detecting the position and energy signals simultaneously, we can pick up only proper position signals that are in coincidence with the energy signals in a reasonable energy range. To operate this system, we need sixteen preamplifiers. For convenience for the future extension to the increased number of channels, we have manufactured a simple preamplifier by referring to a literature [3].

The test of the trial preamplifier shown in Fig. 1 was performed at D-course of 1 MV Tandetron. The target was an a-C:H film of ~200 nm thickness deposited on the Si(100) substrate by chemical vapor deposition (CVD). The hydrogen concentration in the film was determined as ~23 at% from the conventional ERDA carried out in the same D-course. The probe beam of 1 MeV $^{16}O^{+}$ was shaped to 1 mm × 1 mm by a double slit system. The typical beam current was 10 nA. One of the sixteen channels, called "ch4", around the center of the strip detector was connected to the trial preamplifier and linear amplifier, and other channels were floated. We put a slit-like musk to work "ch4" only. The analyzer magnet for HERDA was fixed at 274 mT to observe the hydrogens recoiling near the sample surface. In this case, the recoil energy is 166 keV. The bias voltage of 20 V was used for the strip PIPS as well as the normal PIPS.

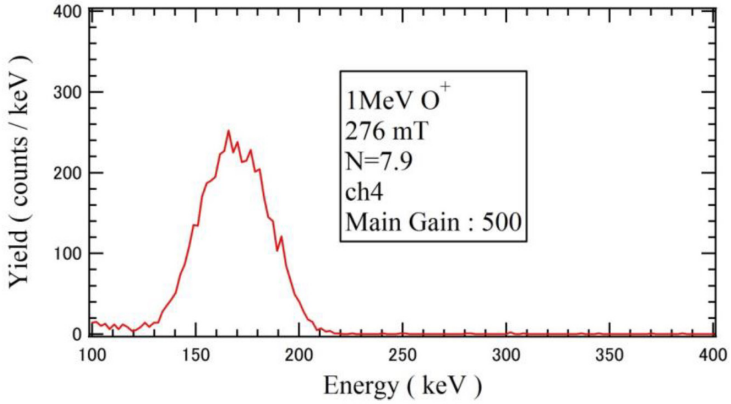

Fig. 2. The signal of recoiling hydrogen detected at "ch4" with the trial preamplifier. The notation "N" is the scale of the linear feed-through to adjust the position of detector. The "Main Gain" signifies the coarse gain of the linear amplifier which follows the preamplifier.

The observed signal is shown in Fig. 2. We see a single peak centered at 166 keV. Even though the energies of the recoiling hydrogen are much smaller than that typically measured with SSD, the peak can be separated from the electrical noises, which allows signal-processing, e.g., by an analog-digital converter. With this preamplifier, we can remove the signals from stray particles, which apparently have too-high or too-low energies (not clearly seen in Fig. 2, but they surely exist). In future works, we will intend to make a lower-noise preamplifier, which can be used for a probe beam of 500 keV $^{16}O^{+}$, and a compact NIM standard module packaging sixteen preamplifiers.

References

[1] K. Kimura et al., Nucl. Instrum. Meth. B 140 (1998) 397.

[2] D. Sekiba et al. , Nucl. Instrum. Meth. B 401 (2017) 29.

[3] Y. Hosono et al., Nucl. Instrum. Meth. A 361 (1995) 554.

4.4 Micro-PIXE analyses of pyrite in sea-floor sediments

M. Kurosawa, K. Hattori, K. Ikehata, K. Sasa, S. Ishii

Pyrite (FeS_2) is a ubiquitous mineral in most hydrothermal ore deposits and can contain high level of trace elements depending on the formation conditions [1-5]. Thus, the trace-element contents have been frequently analyzed to elucidate formation processes of hydrothermal ore deposits and to use for ore exploration [1, 2, 4, 5]. The trace-element analyses have been usually performed by employing electron probe micro analysis (EPMA), particle-induced X-ray emission (PIXE) analysis, and laser-ablation inductively-coupled plasma mass spectrometry (LA–ICP–MS) [1, 2, 4, 5]. In these methods, PIXE has been often used because of the highly-sensitive, non-destructive feature and its potential for trace-element mappings [1, 2, 4]. The common PIXE analyses in geology have focused on only trace heavy-metal elements, while the major components, sulfur and iron, have been paid less attention due to the use of absorbers which selectively absorb intense X-rays from Fe and S [1, 2, 4]. Lattice imperfections or deviation from stoichiometry in pyrite, however, may provide useful information on hydrothermal conditions of the pyrite formation. Thus, simultaneous multi-element PIXE analyses of major to trace elements, reported here, seem to be desirable for studies on chemistries of pyrite. In such a case, intense X-ray peaks of S and Fe, the pile-up and escape peaks possibly cause undesirable influence on the other trace-element detections and the detection limits.

Pyrite crystals were collected from drilling core samples of thick sea-floor clay sediments near an active hydrothermal field at Iheya-North-Knoll in the Okinawa Trough back-arc basin, Japan [6]. The sediments consist mainly of clay minerals including Mg, Na, K, and Ca and contain small amounts of secondary minerals formed by the hydrothermal activities; sphalerite (ZnS), galena (PbS), chalcopyrite ($CuFeS_2$), pyrite, gypsum ($CaSO_4 \cdot 2H_2O$), anhydrite ($CaSO_4$), and barite ($BaSO_4$) [6]. The present pyrite samples are a few millimeter-sized and cubic-shaped crystals with no visible inclusions of their secondary minerals. The sample surfaces were polished and coated with a carbon film to prevent electrostatic charging.

PIXE analyses were performed using 1MV Tandetron at UTTAC. A 0.1-0.3 nA beam of 1.92-MeV protons was focused to a spot size ranging from 26 × 26 μm^2 to 33 × 36 μm^2 on the sample using slits and magnetic lenses. The incident beam was normal to the sample surface, and the X-ray measurement take-off angle was 45˚ [7]. The characteristic X-rays excited by the incident beam were measured with the Si(Li) X-ray-energy detector (Sirius 30+ detector; e2V Scientific Instruments, UK) with a nominal resolution of 137 eV at 5.9 keV. A 55-μm-thick Mylar film was used to attenuate the intense X-rays from the predominant light elements and to prevent the entry into the detector of protons scattered from the samples. The total charge was determined by integrating the target currents, and all samples were analyzed to the total charges of 0.05–0.25 μC. Analytical points were chosen based on optical viewing using a CCD camera mounted on the microscope. Quantification of the PIXE analyses was performed based on the model of Kurosawa et al. [7]. Secondary fluorescence effect was corrected by the method of Reuter et al. [8]. The corrected amounts for most of the elements were less than a few %.

PIXE spectra of the pyrite samples consist mainly of intense K X-ray peaks from S and Fe, and their pile-up and escape peaks, as shown in Fig. 1. There are no significant peak-overlaps between them and L X-ray peaks from important impurities (Ag, Cd, In, Sn, and Sb) in pyrite. Element contents of S and Fe, determined from PIXE, are 46.53–44.57 and 51.45–55.45 wt.%, respectively. This corresponds to their atomic ratios of about 2.00:1.00 (S:Fe), indicating that the hydrothermal activities (<500 °C) do not affect the stoichiometry of pyrite.

A barren-type pyrite, less affected by metal-rich hydrothermal fluids, shows no peaks of metal impurities (Fig. 1, upper spectrum), while fertile-type pyrite, affected by metal-rich hydro-thermal fluids, shows K X-ray peaks from Mn, Cu, Zn, Ga, and As and L X-ray peaks from Ag, Sb, and Pb (Fig. 1, lower spectrum). Thus, these metal impurities in pyrite may be a clue to geochemical exploration of sea-floor hydrothermal ore deposits.

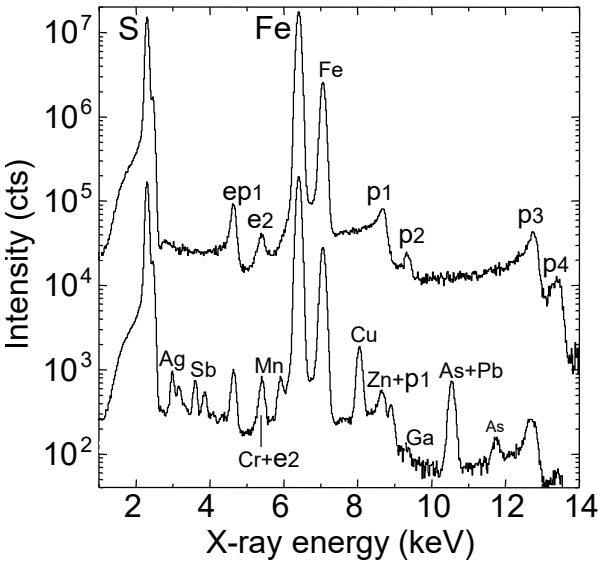

Fig. 1. PIXE spectra of pyrite in sea-floor sediments; the upper spectrum for barren-type pyrite, while the lower spectrum for fertile-type pyrite associated with metal-rich hydrothermal fluids. Escape and pile-up peaks are identified as follows: ep1 (pile-up peak of S K_α+escape peak of Fe K_α), e2 (escape peak of Fe K_β), p1 (pile-up peak of S K_α+Fe K_α), p2 (pile-up peak of S K_α+Fe K_β), p3 (pile-up peak of Fe K_α+Fe K_α), and p4 (pile-up peak of Fe K_α+Fe K_β).

For the fertile-type pyrite, it is important to consider a possibility of invisible solid inclusions buried in pyrite matrix. In fact, X-ray generation depths, the depth above which 99% of the observed X-rays of an element originate at PIXE analyses, shown in Fig. 2, are deeper than those of EPMA. The depths are closely associated with an X-ray self-absorption by sample matrix, thus they depend on the atomic number and on X-ray absorption edges of major elements in a sample matrix.

The self-absorption and the disturbances due to the intense major peaks and their pile-up and escape peaks also may affect the lower detection limits of trace elements in pyrite. In common PIXE analyses, the detection limits for light elements increase with decreasing atomic numbers because of rise of the X-ray absorption coefficients, while those for heavy elements increase with increasing atomic numbers because of decline of ionization cross sections by the incident proton [7]. As a result, the relationship between detection limits and atomic numbers tends to demonstrate a smooth U-shaped curve [7].

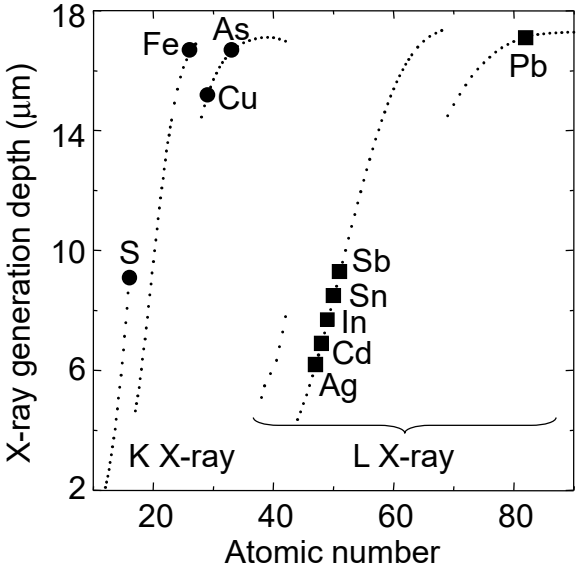

Fig. 2. Representative X-ray generation depths of the present PIXE analyses.

The present relationship, however, is a modified

U-shaped curve as a result of the enhanced detection limits for several elements, as shown in Fig. 3. For K X-rays, transition metal elements with atomic numbers of 21–27 exhibit relatively high detection limits affected by tails and overlaps of intense pile-up and escape peaks of S and Fe. For L X-rays, platinum group elements with atomic numbers of 44–46 display extremely high detection limits affected by X-ray absorption at an absorption edge of S. The enhanced detection limits for elements with atomic numbers of 55–71 (Cs, Ba, and REEs) and 72–80 (e.g., Hf, Ta, and Au) are due to interferences by intense escape and pile-up peaks of Fe.

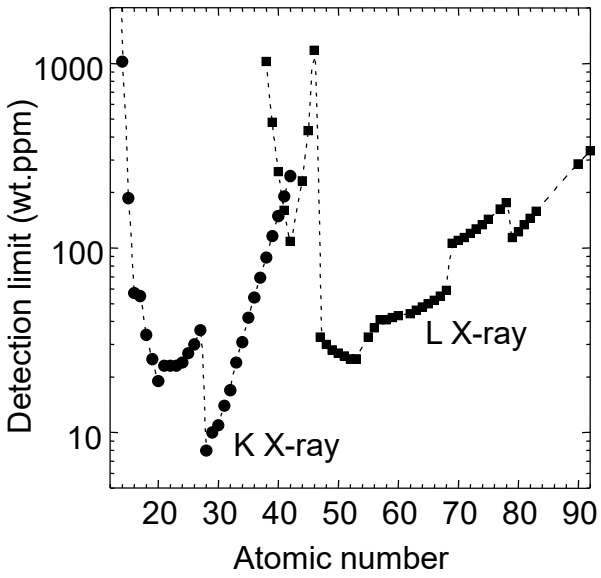

Fig. 3. Detection limits of the present PIXE analyses of pyrite with an integrated charge of 0.25 C. Circles and squares indicate detection limits for measurements of K and L X-rays, respectively.

In summary, the present PIXE analyses demonstrate that the analytical condition using a Mylar filter is effective for sensitive detections of important impurities with atomic numbers of 47–51 (Ag, Cd, In, Sn, and Sb) in pyrite. The analytical condition is also useful to determine precisely sulfur contents required to investigate the stoichiometry of pyrite. In addition, use of an Al filter would be suitable to improve the detection limits for the other elements affected by intense S and Fe and the pile-up peaks.

References

[1] D. Huston et al., Econ. Geol. 90 (1995) 1167.
[2] T. Oberthür et al., Can. Mineral. 35 (1997) 597.
[3] P. Abraitis et al., Int. J. Miner. Process 74 (2004) 41.
[4] A. Agangi et al., Nucl. Instr. and Meth. B348 (2015) 302.
[5] M. Keith et al., Ore Geol. Rev. 72 (2016) 728.
[6] Y. Miyoshi et al., Resour. Geol. 65 (2015) 346.
[7] M. Kurosawa et al., Nucl. Instr. and Meth. B266 (2008) 3633.
[8] W. Reuter et al., J. Appl. Phys. 46 (1975) 3194.

4.5 Mössbauer effect of $CuFe_2O_4$ spinel fine particles under external magnetic field

H. Latiff, M. Kishimoto, S. Sharmin, H. Yanagihara, E. Kita

One of the recent approaches for enhancing magnetic anisotropy of spinel ferrites is the symmetry reduction using lattice distortion. We have observed extraordinarily large PMA (Perpendicular Magnetic Anisotropy) in epitaxially strained Co ferrite (CFO) (001) thin films with K_u exceeding 10 Merg/cm^3 by introducing a tetragonal distortion (c/a<1) in the structure [1, 2], where the lattice distortion results from the lattice mismatch between the substrate (MgO) and the deposited film (CFO). For an application of this approach to the practical bulk production of permanent magnets, development of the material in the form of nanoparticles is required, and a feasible method of introducing lattice distortion to nanoparticles is crucial. We proposed the introduction of lattice distortion via the Jahn-Teller (JT) effect of Cu^{2+} ions in copper substituted Fe_3O_4 particles. We prepared cubic and tetragonal $CuFe_2O_4$ particles and analyzed the crystal structures along with the magnetic properties. Here, we report on the applied field Mössbauer spectroscopy performed to analyze the site distribution of the Fe^{3+} cations in the respective sites.

$CuFe_2O_4$ particles were synthesized by coprecipitation and flux methods. Aqueous solutions containing Cu^{2+} and Fe^{3+} were mixed with NaOH aqueous solution to form precipitates. The precipitates were mixed with KBr flux, and heated at 850℃ for 3 hours. The particles were then rinsed with water to remove the flux. Finally, the particles were annealed at 900°C for 2 hours in air. The XRD patterns of the as-fluxed and heat-treated samples are shown in Fig. 1 (top) and (bottom), respectively. For the as-fluxed particles most of the peaks are of cubic spinel with a slight trace of peaks attributable to CuO. When the as-fluxed particles were heated to 900°C in air, splitted peaks were observed showing the tetragonal spinel phase of $CuFe_2O_4$.

Zero-field and 5T applied-field ^{57}Fe Mössbauer spectra of the tetragonal $CuFe_2O_4$ sample were recorded at room temperature as shown in Fig. 2. The spectra were fitted using the program MossWinn4.0 and the fitting parameters are listed in Table 1. The zero-field (0 T) spectrum was fitted to a combination of two magnetic sextets. The sub-spectrum with higher hyperfine field ($H_{h.f.}$) value originates from the Fe^{3+} in the A sites whereas the other originates from the Fe^{3+} in the B sites. The applied field (5T) spectrum gave a combination of two magnetic quadruplets, due to the reduction of the 2–5 peaks. By applying an external field, these two sub-spectra of the A and B sites are clearly separated, providing more precisely fitted spectra and area ratios of Fe^{3+}. The values of $H_{h.f.}$ for the A and B sites with no applied field are 47.9 and 50.7 T, respectively, whereas the literature values are 48.1 and 50.5 T, correspondingly. Our spectra thus show considerably good agreement with the reported values within experimental errors [3]. The non-zero values of *Q.S.* indicate that the sample contains a non-cubic structure, i.e. a tetragonal structure or local distortion, which agrees with the crystal structure confirmed from the XRD pattern. The values of *I.S.* for the A and B sites' sub-spectra are 0.18 mm/s and 0.29 mm/s respectively, indicating that they originate from Fe^{3+} ions, and not Fe^{2+}. From the fit results of the 5 T spectrum, the area populations of the two types of Fe^{3+} ions distributed in the A and B sites were 46.3 and 53.7%, respectively. The

relative area ratio shows that the concentration of Fe^{3+} ions is higher in the B sites than in the A sites. This suggests that the structure contains anti-site defects where some of the Cu^{2+} from the B sites are exchanged with the Fe^{3+} in the A sites.

The magnetic properties are summarized in Table 2. The M_S for the cubic and tetragonal $CuFe_2O_4$ samples are 25 and 26.9 emu/g, respectively. The values are in good agreement with the calculated values $M_S^{Calc.}$. The slightly higher value of the experimental M_S is possibly due to the presence of anti-site defects, as observed in the Mössbauer study. The coercivities of the cubic and tetragonal $CuFe_2O_4$ is 130 and 870 Oe, respectively. The higher coercivity in the tetragonal sample may be due to the anisotropy induced during the tetragonalization process.

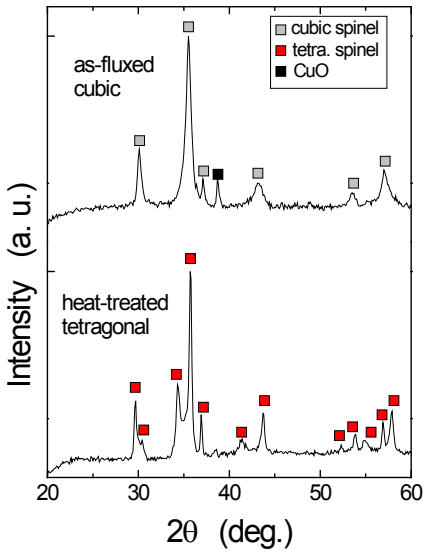

Fig. 1. XRD patterns of as-fluxed (top) and heat-treated (bottom) $CuFe_2O_4$ particles.

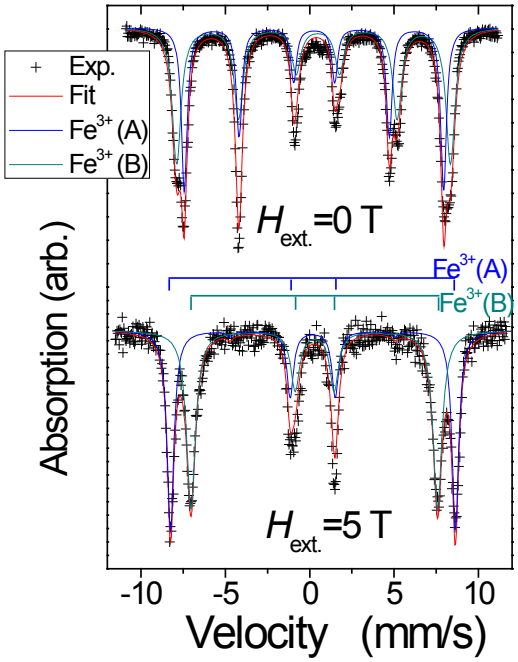

Fig. 2. Room temperature ^{57}Fe Mössbauer spectra of tetragonal $CuFe_2O_4$ particles without external magnetic field (top) and with 5T external magnetic field (bottom).

Table 1. Mössbauer fitting parameters.

H_{ext} (T)	Sub-spectrum	*I.S.* (mm/s)	H_{hf} (T)	*Q.S.* (mm/s)	*L.W.* (mm/s)	Area (%)
0	Fe^{3+}(A)	0.26	47.9	-0.02	0.473	38.1
	Fe^{3+}(B)	0.36	50.7	-0.28	0.412	61.9
5	Fe^{3+}(A)	0.19	52.5	0.01	0.479	46.3
	Fe^{3+}(B)	0.28	45.4	-0.02	0.635	53.7

*Isomer shift with respect to α-Fe

Table 2. Magnetic properties of the cubic and tetragonal $CuFe_2O_4$ particles.

Sample	H_C (Oe)	M_S (emu/g)	$M_s^{calc.}$ (emu/g)
Cubic	133	25	21
Tetra.	869	26.9	

References

[1] H. Yanagihara et al., J. Appl. Phys. 111 (2011) 07C122-1.

[2] T. Niizeki et al., Appl. Phys. Lett. 103 (2013) 162407-1.

[3] B. J. Evans and S. S. Hafner, J. Phys. Chem. Solids 29 (1968) 1573.

4.6 Low temperature Mössbauer study on spherical α”-$Fe_{16}N_2$ core–shell nanoparticles with high magnetic anisotropy

E. Kita, K. Shibata, Y. Sasaki, M. Kishimoto, H. Yanagihara

Fe nitrides have a variety of crystalline structures depending on the concentration of nitrogen. There are a few ferromagnetic nitrides, which have been studied from the practical viewpoint [1]. α”-$Fe_{16}N_2$ has a tetragonally distorted structure from a BCC structure, in which one of the <100> axes is elongated and the nitrogen atoms are ordered. This substance has been studied by many people for its high saturation magnetization; the compound also exhibits a uniaxial magnetic anisotropy due to the distorted structure, showing promise for use in applications such as high-performance magnetic data recording tapes [2] with core–shell type spherical nanoparticles (NPs) [3]. Recently, new permanent magnet materials that do not require rare elements have been highly sought and α”-$Fe_{16}N_2$ is a good candidate, as it has high saturation moments and a large anisotropy constant (K_u).

The amplitude of K_u is an important parameter not only for bulk applications but also for the realization of perpendicular magnetic thin films. We have reported that K_u of the core–shell α”-$Fe_{16}N_2$ NP, estimated from typical torque measurements and room temperature Mössbauer measurement, is 4.4×10^6 erg/cm^3 [4]. In order to evaluate the precise amplitude of K_u, the portion of α”-$Fe_{16}N_2$ in NP should be carefully analyzed. We performed detailed torque measurements and re-analyzed the low-temperature Mössbauer spectrum [5].

The core–shell α”-$Fe_{16}N_2$ NPs were prepared using NH_3 nitrification. First, Fe_3O_4 particles with a diameter of 18 nm underwent hydrogen reduction. Succeeding nitrification was carried out in an atmosphere of H_2 and NH_3 [3]. Magnetically aligned samples were prepared by drying the organic solvent of particles on the polymer films in a magnetic field parallel to the films.

Figure 1 shows the Mössbauer spectrum of α”-$Fe_{16}N_2$ NPs recorded at 4.2K. We have already evaluated the portion of the α”-$Fe_{16}N_2$ by using room temperature Mössbauer data, however analysis of data recorded at low temperature is desirable because influence of recoil absorption is less at low temperature. It is noted that the surface oxide was in paramagnetic state at room temperature and became almost ordered at low temperatures.

Data fitting was carried out using a commercially available program, MossWinn 4.0. Obtained Mössbauer parameters are listed in Table1. It was found that a paramagnetic part seen at room temperature [4] changes into a magnetic sextet with large internal field of 486 kOe. From the amplitudes of the hyperfine field and the *I.S.*, the part was concluded to be mainly the Fe oxide composed of Fe^{3+} ions. Resulted portion of the α”-$Fe_{16}N_2$ phase was 54.4 %, slightly less than that at room temperature, 56.2% [4]. It can be elucidated by the fact that the lower Debye temperature for the oxide shell part resulted in the decrease in the observed oxide volume at room temperatures. The magnetic anisotropy energy for core–shell α”-$Fe_{16}N_2$ NPs was evaluated by the rotational hysteresis loss obtained from torque measurements. The saturation magnetization and anisotropy constant were deduced to be 234 emu/cm^3 and 6.9×10^6 erg/cm^3, respectively [5]. These values are more precise than the previous data [4] because the accurate

volume fraction was determined by using the low temperature Mössbauer data.

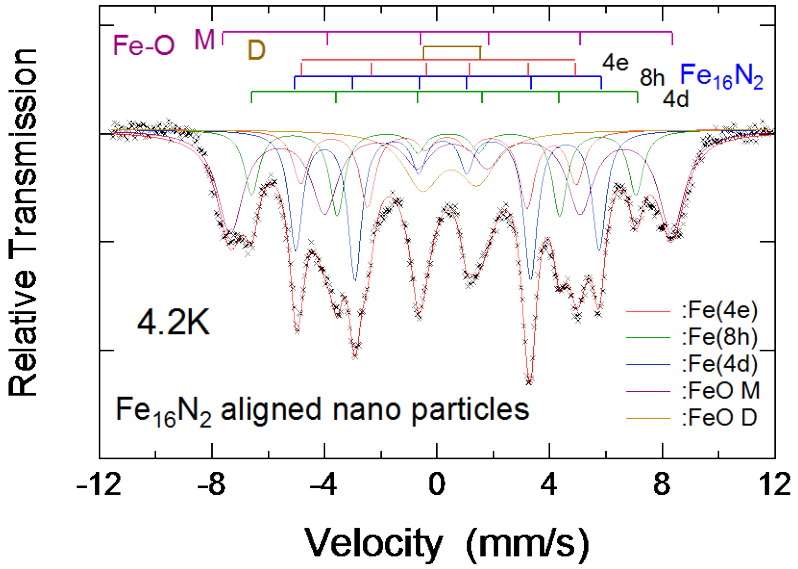

Fig. 1 Mössbauer spectrum for the α"-$Fe_{16}N_2$ aligned sample recorded at 4.2K. Solid lines show the results of the fit, which are summarized in Table 1. Corresponding peak positions of sub-spectra are indicated by three bars for magnetic sub-spectra of the α"-$Fe_{16}N_2$ core and two bars, magnetic sextet (M), and paramagnetic doublet (D), for the outer shell of Fe oxides (Fe-O) [5].

Table 1. Mössbauer parameters: hyperfine field (H_{hf}), isomer shift (*I.S.*), quadrupole split (*Q.S.*), and area ratio for α"-$Fe_{16}N_2$ aligned nanoparticles at 4.2K [5] .

Phase	Site	H_{hf} (kOe)	*I.S.*(mm/s)[a]	*Q.S.* (mm/s)	*Area* (%)
$Fe_{16}N_2$	4e	304	0.200	–0.313	13.8
	8h	334	0.28	0.166	25.4
	4d	423	0.315	–0.162	15.2
Fe-O	D	–	0.448	1.97	11.6
	M	486	0.513	–0.05	34.0

[a]Relative to room temperature α-Fe.

References

[1] J. M. D. Coey and P. A. I. Smith, J. Magn. Magn. Mater. 200 (1999) 405.

[2] Y. Sasaki et al., IEEE Trans. Magn. 41 (2005) 3241.

[3] K. Shibata et al., J. Magn. Soc. Jpn. 30 (2006) 501.

[4] E. Kita et al., J. Magn. Magn. Mater. 310 (2007) 2411.

[5] E. Kita et al., AIP Advances **7** (2017) 056212.

4.7 Characterization of oxide thin films with RBS technique

R. Patel, Y. Ikeda, Y. Hisamatsu, S. Sharmin, H. Yanagihara

Barium hexaferrite ($BaFe_{12}O_{19}$; BaM) is a magnetic oxide with the magnetoplumbite structure which has a hexagonal close packed (HCP) oxygen frame-work structure [1]. BaM has unique magnetic properties such as high uniaxial magnetic anisotropy, moderate saturation magnetization, and high Curie temperature [2-3]. Previous studies showed that the BaM films grown by various different methods such as, pulsed laser deposition, liquid phase epitaxy, and radio frequency sputtering have lower saturation magnetization and squareness ratio, compared with the bulk [4-8]. The reason for this is not well understood until now. For applied purposes, the high quality thin film growth technique is required to achieve large magnetization comparable to the bulk. Nevertheless to say, fundamental physical properties of a film are strongly dependent on chemical composition if the film is alloy or compound. Thus, the purpose of this research is to understand the effect of composition on the magnetic behavior of the barium hexaferrite (0001) thin films.

The epitaxial growth of BaM (0001) thin films was performed on an α-Al_2O_3 (0001) substrate via radio frequency (RF) magnetron sputtering. Stoichiometric ($BaFe_{12}O_{19}$) target with a diameter of 68 mm was used. The flow rate of Ar was 10 sccm; total pressure inside the sputtering chamber was maintained at 0.57 Pa. Prior to the deposition, the substrates were annealed under vacuum at the growth temperature of 800°C for 1 hour. The RF power of the sputtering process was set at either 50 or 100 W. The BaM (0001) thin films of 101 nm thickness were deposited. The BaM (0001) thin films were post-annealed in atmosphere at 1000 °C for 10 minutes. Compositional characterization by Rutherford backscattering spectroscopy (RBS) was carried out using 1MV Tandetron at UTTAC.

The RBS spectra of BaM (0001) thin films for RF power of 50 and 100 W are shown in Fig 1. The experimentally obtained composition ratios of Ba to Fe in BaM (0001) thin films are shown in Table 1. The evaluated off-stoichiometric ratio of Ba:Fe was 1:9 (for the growth at 100 W), suggesting that some defects exist in the hexaferrite films obtained. The crystal structure of barium hexaferrite is close-packed layers form with four fundamental blocks, S, S*, R and R*. The S* and R* blocks can be obtained simply through the rotation of the S and R blocks, respectively, by 180° with respect to the c-axis. A pair of either S and R or S* and R* conserves charge neutrality and Ba ions occupy the R (or R*) block. Therefore, an off-stoichiometric M-type hexaferrite may involve the other oxide block such as T-block. The estimated concentration of T-block is about 23%, which affects neither magnetization nor magnetic anisotropy because the T-block is composed of Ba^{2+}, Fe^{3+} and O^{2-} ions and is magnetically compensated. The rest of S R S* R* block influences M_s and K_u(eff.), which are 292 emu/cm^3 and 2.46 Merg/cm^3, respectively, and they are close to the experimental values. Therefore, such reduction of M_s and K_u(eff.) in BaM (0001) thin films could be explained by the existence of the T-block.

In summary, the BaM (0001) thin films were deposited on α-Al_2O_3 (0001) substrates by RF magnetron sputtering. The composition study revealed that the barium to iron ratio in the deposited thin film is variable. The effect of RF power on the composition helps us to understand the reason for the lower

saturation magnetization.

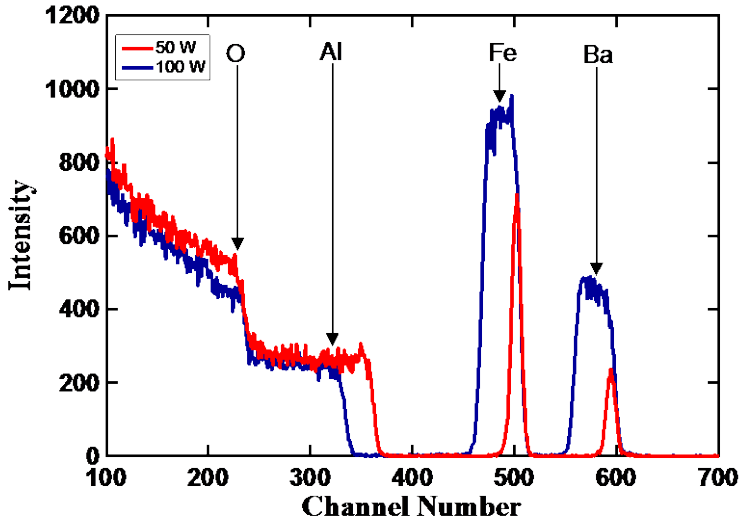

Fig. 1. The RBS spectra of BaM (0001) thin film with RF power of 50 W and 100 W.

Table 1. The composition ratios of Ba to Fe determined from RBS spectra.

Target	RF Power (W)	Ba_x	Fe_{13-x}
$BaFe_{12}O_{19}$	50	0.84	12.16
$BaFe_{12}O_{19}$	100	1.31	11.69

References

1. R. O. Handley, Modern Magnetic Materials (Wiley, New York, 2000).
2. B. T. Shirk et al., J. Appl. Phys. 40 (1969) 3.
3. B. D. Cullity and C. D. Graham, Introduction to Magnetic Materials (Wiley, New York, 2009).
4. H. J. Masterson et al., J. Appl. Phys. 73 (1993) 8.
5. S. A. Oliver et al., J. Magn. Magn. Mater. 213 (2000) 326.
6. A. Lisfi et al., Appl. Phys. Lett. 83 (2003) 4.
7. S. D. Yoon et al., J. Appl. Phys. 4 (2004) 96.
8. H. Xu et al., Appl. Surf. Sci. 257 (2011) 2689.

4.8 Low temperature synthesis of highly oriented $Si_{1-x}Ge_x$ (x: 0–1) on an insulator by Al-induced layer exchange

K. Toko, T. Suemasu

A composition tunable $Si_{1-x}Ge_x$ alloy has a wide range of applications, especially to electronic and photonic devices. We investigate the Al-induced layer exchange (ALILE) growth of amorphous $Si_{1-x}Ge_x$ on an insulator (SGOI). Figure 1 presents a schematic of the sample preparation process. Preparation of the Al and amorphous (a-) $Si_{1-x}Ge_x$ layers (each 50 nm thick) on a SiO_2 glass substrate was performed at room temperature using radio frequency (RF) magnetron sputtering (base pressure: 3.0×10^{-4} Pa) with Ar plasma. The RF power was set to 50 W for all of the $Si_{1-x}Ge_x$ targets. The Ge composition x in the prepared a-$Si_{1-x}Ge_x$ layers was determined to be 0, 0.15, 0.3, 0.6, and 1 by Rutherford backscattering spectrometry (RBS) employing 2.0MeV ^{4}He ions from 1MV Tandetron at UTTAC. Between the two deposition cycles, the Al film was exposed to air for 30 min to form a native Al oxide layer as a diffusion-limiting layer [1]. The samples were then annealed at 340–450°C in a N_2 ambient chamber with an in-situ optical microscope observation system until the layer exchange was finished. The Al and AlO_x layers were then etched away with HF solution (HF: 1.5%) for 1 min.

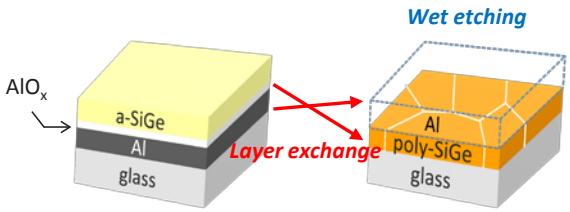

Fig. 1. Schematic image of the sample preparation procedure.

The nucleation rate n and lateral growth velocity v_g of the samples were calculated from the slopes of the time dependent nuclei density and domain size. Figure 2(a) shows that there is no clear dependence of the Ge fraction on n. This result suggests that n is determined by the diffusion-limiting AlO_x layer whose thickness strongly depends on the humidity during Al air exposure. Figure 2(b) shows that v_g increases with increasing Ge fraction, which is the same behavior as the crystallization of the a-$Si_{1-x}Ge_x$ layers. We note that the ALILE provides a v_g two orders of magnitude higher than that of the solid phase crystallization (SPC) of a-$Si_{1-x}Ge_x$ [2] which leads to large domain growth.

From the Arrhenius equation and the results from Figs. 2(a) and 2(b), we

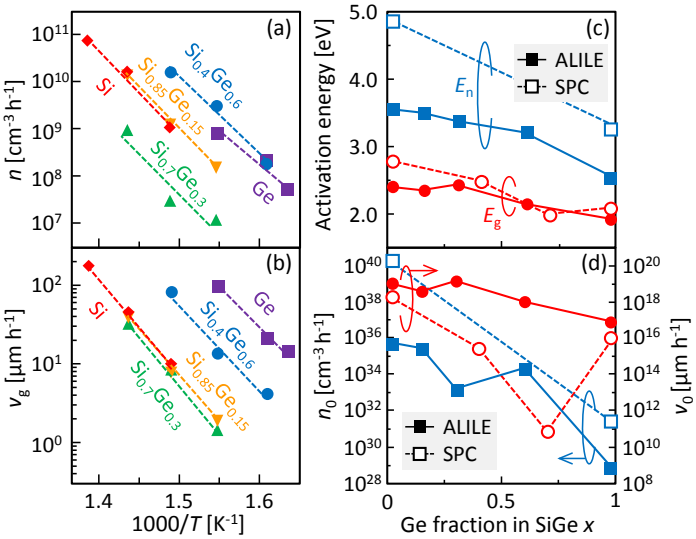

Fig. 2. Growth properties of the $Si_{1-x}Ge_x$ (x: 0, 0.15, 0.3, 0.6, and 1) samples. Arrhenius plots of the (a) nucleation rate n and (b) lateral growth velocity v_g. (c) Ge fraction dependence of the activation energies of nucleation E_n and lateral growth E_g. (d) Ge fraction dependence of the frequency factors of nucleation n_0 and lateral growth v_0. For comparison, the data of SPC regarding the nucleation of Si[3] and Ge[4] and the lateral growth of SiGe[2] are shown in (c) and (d).

determined the activation energies of nucleation E_n and lateral growth E_g and the frequency factors of nucleation n_0 and lateral growth v_0. Figures 2(c) and 2(d) show that both the activation energies and frequency factors decrease with increasing Ge fraction x. These facts indicate that the lowering of the growth temperature with increasing x arises from the reduction of the activation energies. Therefore, we compared the growth characteristics between ALILE and SPC as follows. Figure 2(c) shows that ALILE exhibits a lower E_n than SPC [3, 4]. This is because, with ALILE, SiGe nucleates in the Al grain boundaries at a lower interfacial energy compared with SPC, where SiGe nucleates in the amorphous SiGe layer. Figure 2(c) also shows that E_g is almost the same for ALILE and SPC [2]. This is reasonable considering that E_g corresponds to the energy required for SiGe atoms to adhere to crystalline SiGe. Figure 2(d) shows that ALILE exhibits a lower n_0 than SPC [3,4]. This can be explained by the lower density of SiGe atoms in Al for ALILE than that of amorphous SiGe for SPC. Figure 2(d) also shows that ALILE exhibits a higher v_0 than SPC [2]. This is because the SiGe atoms migrate faster in Al for ALILE than in amorphous SiGe for SPC. The above discussion accounts for why ALILE can provide larger SiGe grains at lower temperature compared with SPC.

The crystal orientation and actual grain size of the $Si_{1-x}Ge_x$ layers formed at low temperatures ($\leq$ 400°C) were evaluated using electron backscatter diffraction (EBSD). The $Si_{1-x}Ge_x$ layers were highly (111)-oriented in the entire SiGe composition range. The (111) orientation can be explained from the perspective of the appearance of the energetically stable plane [1]. The $Si_{1-x}Ge_x$ layers had grains with diameters of several tens of μm. These actual grain sizes are smaller than the domain size observed from optical microscopy because the domains are divided into several grains. The (111) fraction and grain size did not depend on the SiGe composition, but correlate roughly with the growth rate. These results show that slow annealing is a key to fabricate a highly oriented, large-grained SiGe layer regardless of the composition. Thus, we have demonstrated SiGe layers on an insulator with a (111) orientation fraction of over 95% and a grain size over 50 μm over the entire SiGe composition range. These values are the highest among the low temperature synthesized SGOIs.

In conclusion, we have achieved ALILE growth of a-$Si_{1-x}Ge_x$ on insulators at low temperatures ($\leq$ 400°C) over the entire composition range. The ALILE provided a low nucleation frequency and high lateral growth velocity, resulting in large $Si_{1-x}Ge_x$ grains with diameters of no less than 50 μm. The area fractions of the (111) orientation were more than 95%. The SGOI fabricated in this study is useful as virtual substrates allowing advanced materials to be integrated on three-dimensional LSIs, glass, and even a plastic substrate.

The authors are grateful to Dr. D. Sekiba of UTTAC for RBS analyses.

References

[1] K. Toko et al., Appl. Phys. Lett. 104 (2014) 022106.
[2] K. Toko et al., Appl. Phys. Lett. 94 (2009) 192106.
[3] K. Zellama et al., J. Appl. Phys. 50 (1979) 6995.
[4] P. Germain et al., J. Appl. Phys. 50 (1979) 6986.

4.9 Quantitative analysis of light elements in mixed-anion compound thin films

D. Kutsuzawa[1], Y. Hirose[1], D. Sekiba

Recently, oxyhydrides have been intensively studied because of their unique physical and/or chemical properties. For example, hydride (H^-) ions in perovskite-type $ATiO_xH_y$ (A = Ca, Sr, Ba) are highly labile, which enables low-temperature anion exchange reaction, such as H^-/D^-, H^-/O^{2-}, H^-/N^{3-}, etc. These oxyhydrides are also expected as catalysts for synthesis of NH_3 [1]. A significant issue in studies on oxyhydrides is a quantitative analysis of hydrogen amount. However, conventional techniques such as secondary ion mass spectrometry [2], thermal desorption spectrometry [2] and Rietveld refinement of neutron diffraction [3] have relatively low accuracy due to matrix effect, interference from coexisting impurities, and so on. In order to resolve this problem, we focused on elastic recoil detection analysis (ERDA), by which absolute amount of hydrogen in a film can be determined without a standard sample. In this study, we investigated chemical composition of $SrTiO_xH_y$ thin films by combination of ERDA and Rutherford backscattering spectrometry (RBS) analysis [3].

$SrTiO_xH_y$ thin films were prepared by a topotactic reaction reported previously [2]: First, precursor $SrTiO_3$ epitaxial thin films were grown on $(LaAlO_3)_{0.3}(SrAl_{0.5}Ta_{0.5}O_3)_{0.3}$ (100) substrate (LSAT) by pulsed laser deposition method. Then, the obtained $SrTiO_3$ films were sealed in an evacuated silica tube with CaH_2 powder, and reacted at 500°C for 24 hours in an electric furnace. The composition of the films before and after the reaction was evaluated by ERDA and RBS with a 2.5 MeV ^{4}He beam. The incident angle of ^{4}He was 15° from the sample surface and the detection angle for ERDA and RBS measurements were 30° and 150°, respectively. Intensity of the spectra were normalized by dose amount of ^{4}He particles calculated from output current of a beam chopper located upstream of the beam path.

Figure 1 shows out-of-plane $2\theta/\theta$ X-ray diffraction patterns of STO/LSAT(100) epitaxial films before and after CaH_2 treatment. 200 diffraction peak of STO was shifted to higher angle after the reaction, which means out-of-plane lattice constant was shrunk by the reaction. This result suggests successful substitution of H^- for O^{2-} in the perovskite lattice [2].

Figure 2 shows RBS spectra of the STO film after CaH_2 treatment. It was difficult to determine the cation ratio of the film (Sr/Ti) from the spectrum, because Sr peak from the film located at around 820 channel was unclear due to overlap of Sr, La and Ta peaks from the substrate. Another substrate is needed to evaluate the cation composition precisely.

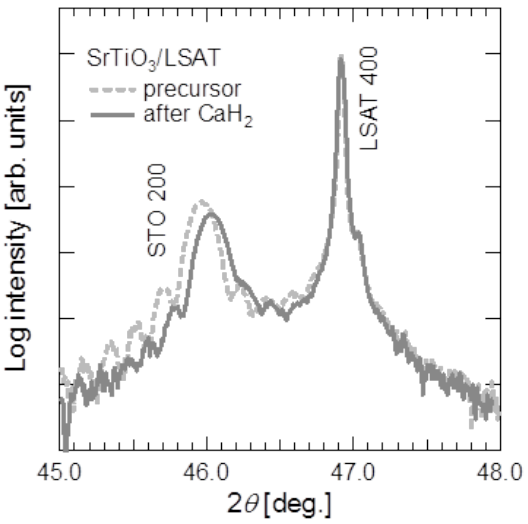

Fig. 1. $2\theta/\theta$ XRD patterns of STO/LSAT(100) epitaxial film before and after CaH_2 treatment

[1] The University of Tokyo

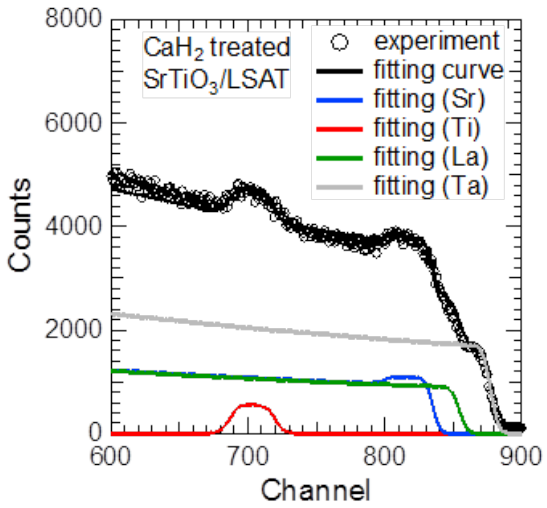

Fig. 2. RBS spectra of CaH_2 treated STO/LSAT(100) epitaxial film. Black circle is experimental data and black, blue, red, green and gray lines are fitting lines of total, Sr, Ti, La and Ta, respectively.

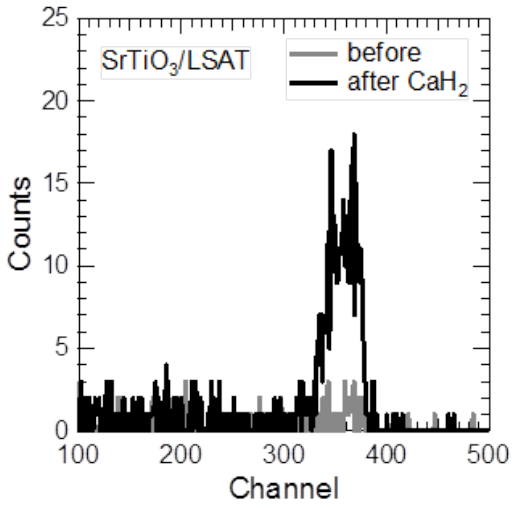

Fig. 3. ERDA spectra of STO/LSAT(100) epitaxial film before (gray) and after (black) CaH_2 treatment.

Figure 3 shows ERDA spectra of the films before and after CaH_2 treatment. A clear peak of recoiled hydrogen was observed for the CaH_2-treated film, while there is no such peak for the precursor film. Then, hydrogen to titanium ratio, N_H/N_{Ti}, of the film were determined from the peak area considering recoil cross section of each element and solid angles of the detectors for ERDA and RBS systems. The determined N_H/N_{Ti} value is 0.22, which agrees reasonably with the value reported previously ($SrTiO_{2.75}H_{0.25}$, CaH_2 treatment at 530°C for 24 hours) [2].

In conclusion, we succeeded in evaluating hydrogen amount in a $SrTiO_xH_y$/LSAT(100) epitaxial film by ERDA/RBS analysis. Our results demonstrated that these techniques are useful for composition analysis of oxyhydrides.

References

[1] 内田他、日本セラミックス協会秋季シンポジウム 2F02 (2015).

[2] G. Bouilly et al., Chem. Mater. 27 (2015) 6354.

[3] Y. Kobayashi et al., Nat. Mater. 11 (2012) 507.

4.10 Oxygen reduction reaction catalytic site analysis by Mössbauer spectroscopy

S. Yasuda[1], R. Osaka[1], Y. Uchibori[1]

Iron-nitrogen-carbon (Fe-N-C) catalyst has been drawing attention as one of alternatives to costly and limited resources such as Pt-based catalysts for oxygen reduction reaction (ORR) on cathodes of polymer electrolyte membrane fuel cells. Fe-N-C catalyst possesses ORR catalytic structures where a metal iron atom is coordinated to nitrogen functionalized graphitic carbon, and the catalytic sites are supported on conductive carbon materials. Recently, Fe-N-C coated on carbon nanotube (Fe-N-C/VA-CNT) catalyst was produced by employing vertically aligned carbon nanotubes (VA-CNT) with a high specific surface area (~1100 m^2/g). Pyrolyzing iron(II) phthalocyanine (FePc) molecules and VA-CNT mixed composite easily transformed the adsorbed FePc molecules into a large number of Fe-N-C structures on the individual VA-CNT surfaces [1]. Although the Fe-N-C/VA-CNT catalyst exhibited a high ORR activity, there are few studies on the Fe-N-C catalytic structure on CNT. In this study, Mössbauer spectroscopy was employed to assess the Fe-N-C catalytic structure, and investigated the pyrolysis dependence of the Fe-N-C catalytic structures.

Figures 1(a) and (b) show deconvoluted Mössbauer spectra of the Fe-N-C/VA-CNT catalysts prepared by 5 and 60 min pyrolysis time, respectively. Here, we remember previous Mössbauer studies assigned to three Fe-N-C catalytic structures which consist of a Fe-ion coordinated by four nitrogen groups connected to graphene structure (FeN4). They are a ferrous low-spin FeN4 site (Doublet 1), a ferrous intermediate spin FeN4 site (Doublet 2) and ferrous high spin FeN4 site (Doublet 3), Fig. 1(c) shows bar graphs of the five components of Fe species obtained from the peak deconvolution results. We see that the fraction of iron carbide increases with increasing the pyrolysis time, while the fraction of the doublets decreases. The results indicate that long pyrolysis promote decomposition of the Fe-N-C catalytic structure, resulting in production of the iron carbide nanoparticles.

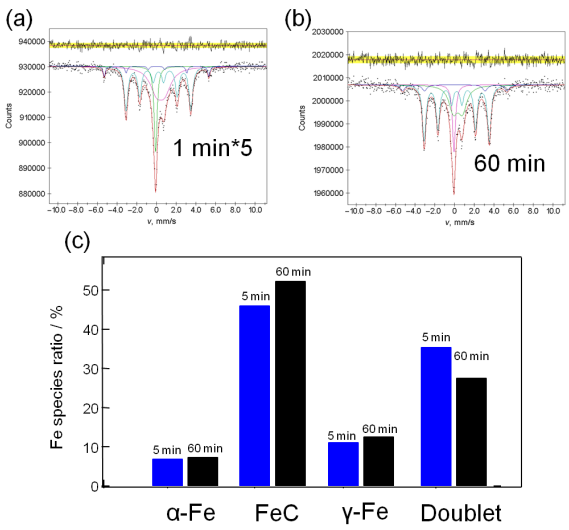

Fig. 1. Deconvoluted Mössbauer spectra of the Fe-N-C/VA-CNT catalysts prepared by (a) 5min and (b) 60 min pyrolysis time, respectively, and (c) Bar graphs of Fe species.

References

[1] S. Yasuda et al., Advanced Functional Materials 26 (2016) 738.

[1] Hokkaido University, Sapporo, 060-0810, Japan

4.11 Sputtering loss of Zn nanoparticles in SiO_2 induced by MeV C_{60}^+ ion irradiation

H. Amekura[1]

Intending shape and/or size control of nanoparticles (NPs) embedded in dielectrics, Zn NPs embedded in silica glass (SiO_2) were irradiated with C_{60}^+ ions of 2, 4, and 6 MeV in Takasaki Advanced Radiation Research Institute, National Institute for Quantum and Radiological Science and Technology (QST). However, we have observed highly serious sputtering loss of the NPs. The energy losses of C_n cluster ions are often estimated under the approximation of independent n monomers with the same velocity with the incident cluster ion; i.e.,

$$S_i(E, C_{60}) = 60\, S_i(E/60, C_1) \qquad (1)$$

where i represents e (electronic) or n (nuclear) [1]. This formula indicates that the energy loss of C_{60} ion with the energy E is equivalent to 60 times the energy loss of C monomer with the energy of E/60. While we used C_{60} ions of 2–6 MeV, the corresponding monomer with the same velocity has the energy E/60 = 33–100 keV. At the beginning of this study, we expected the collisional mechanism for sputtering under 33-100 keV C monomer ion irradiation, because of the low energies. Consequently, the same were

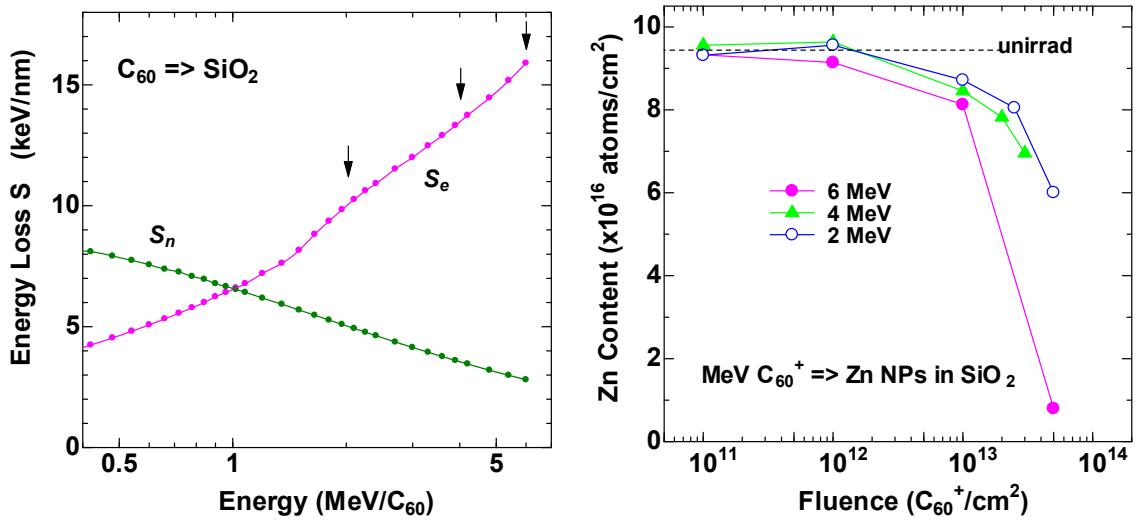

Fig. 1(Left). Energy dependences of electronic and nuclear energy losses (S_e, S_n) of C_{60} ion in crystalline SiO_2 were estimated from those of C monomer ion under the approximation of independent C monomers with the same velocity. The energy losses of the C monomer were derived from SRIM 2013 code. The irradiation experiments were carried out at the energies indicated by arrows.

Fig. 1(Right). Fluence dependences of Zn content in the amorphous SiO_2 samples including Zn nanoparticles. The samples were irradiated with C_{60}^+ ions of 2, 4, and 6 MeV. The Zn contents were determined by RBS.

[1] National Institute for Materials Science (NIMS)

expected for 2-6 MeV C_{60} irradiation, because of the same velocities. Figure 1 shows the energy dependences of the electronic and nuclear energy losses, which were calculated under the approximation of the independent monomers with the same velocity as the incident cluster ion. Although the electronic loss S_e is predominant over the nuclear loss S_n at the energies where the experiments were carried out as indicated by arrows, the contributions of S_n cannot be neglected.

While S_e increases with increasing the energy, S_n decreases. If the sputtering efficiency increases (decreases) with increasing the energy, the predominant mechanism of the sputtering by C_{60} ions in the energy range of 2–6 MeV is determined as the electronic (nuclear) origin. To experimentally determine the energy dependence of the sputtering induced by C_{60} ions, the fluence dependence of the Zn content of the samples was determined by Rutherford backscattering spectrometry (RBS). Since the Zn NPs were formed by 60 keV Zn^+ ion implantation, they were formed only near the surface shallower than 70 nm. They can act as sputtering markers.

A He^+ ion beam of 1.6 MeV from the 1 MV Tandetron at UTTAC was used. The beam size was 1 mm × 1 mm. The scattering angle and the solid angle of the surface barrier detector were 150° and 0.00785 sr, respectively. The surface normal of the sample was tilted 5° off from the beam axis towards the backscattering direction, following the IBM geometry [2]. Each sample was irradiated to the He^+ dose of 420 nC. The data were analyzed using RUMP code [3] and the Zn content was determined.

The fluence dependence of the Zn content for the irradiation of 2, 4, and 6 MeV C_{60}^+ ions is shown in Fig. 1(Reft). Although the nominal Zn content is 1.0×10^{17} atoms/cm^2, an unirradiated value estimated is 9.44×10^{16} atoms/cm^2. Clear losses were observed at the fluence of 1×10^{13} C_{60}^+/cm^2 or higher. The loss was higher for higher ion energy, indicating that the electronic energy loss is the predominant process of the sputtering induced by C_{60} ions of 2–6 MeV in Zn NPs embedded in SiO_2.

References

[1] S. Bouneau, et al., Phys. Rev. B 65 (2002) 144106.

[2] M. Mayer, Rutherford Backscattering Spectrometry (RBS), Lecture note (2003). http://users.ictp.it/~pub_off/lectures/lns022/Mayer_1/Mayer_1.pdf.

[3] L.R. Doolittle, Nucl. Instrum. Methods Phys. Res. B 15 (1986) 227.

4.12 HR-RBS study of the rutile TiO_2(110) surface

N. Nagatsuka [1], K. Fukutani [1], E. Noguchi, I. Harayama, D. Sekiba

Titanium dioxide (TiO_2) is a model system of transition metal oxides, and its surface has received much attention in application to a photocatalyst and a transparent conductive film. However, the surface electronic states of TiO_2 are yet to be elucidated due to strong electron correlation and electron-phonon interaction. It has been reported that structural defects dope excess electrons in TiO_2 exerting strong effects on the conductivity and catalytic activity of the surface. It is also reported that the excess electrons doped by the defects form polaronic states at the rutile (110) surface with substantial deformation of the lattice [1]. There are three types of defects: an oxygen vacancy at the topmost surface, an oxygen vacancy in the subsurface region and a titanium interstitial. Theoretical calculations have indicated that these defects cause different electronic states and lattice structures [2,3]. Although a lot of efforts have been made to clarify the electronic states associated with these defects, few experimental studies on the lattice structure have been reported. Since the lattice structure is closely related to the electronic state, information of the lattice deformation induced by defects is of crucial importance.

In the present study, we investigated the lattice structure of the rutile TiO_2(110) surface with high-resolution Rutherford backscattering spectroscopy (HR-RBS). The TiO_2(110) surface was prepared by repeated cycles of Ar ion sputtering and annealing in an ultra-high vacuum, and oxygen vacancies were created by irradiation of electrons at 500 eV. HR-RBS measurements were performed with He^+ ions at 400 keV and the scattered ions were analyzed by a high-resolution magnetic spectrometer.

Figure 1 shows two-dimensional channel maps for clean and electron-irradiated (ESD) surfaces of TiO_2 (110) around the [100] axis on the (010) plane. Channeling dips are clearly observed along with the surface peaks for both surfaces. The channeling profile looks asymmetric, which is caused by the structural asymmetry. Furthermore, the channeling dip of the ESD surface at the surface peak of Ti is slightly narrower than that of the clean surface suggesting a slight displacement of Ti.

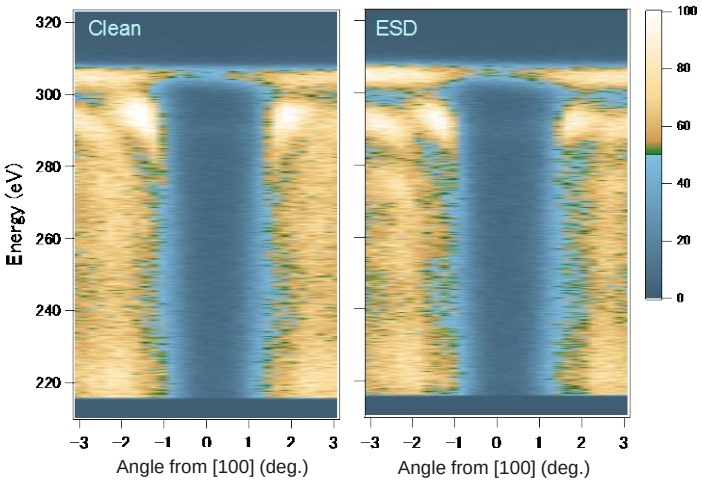

Fig. 1 2D-channel maps for clean and electron-irradiated surfaces of rutile TiO_2(110) around [100].

References

[1] M Setvin et al, Phys. Rev. Lett. 113 (2014) 086402.

[2] E Finazzi et al, J. Phys. Chem. C 113 (2009) 3382.

[3] B. J. Morgan et al, J. Phys. Chem. C 113 (2009) 7322.

[1] Institute of Industrial Science, University of Tokyo

4.13 Profiling of hydrogen in thick films employing transmission ERDA technique

H. Naramoto, M. Sataka, H. Kudo, K. Yamazaki, K. Sasa, H. Oshima

In metallic materials, diffusional behaviors of hydrogen as mobile interstitials are sensitively influenced by atomic disorders, which results in the serious deterioration of structural and/or transport properties. In order to understand the relevant mechanisms, it is indispensable to know the spatial distribution and the microstructure of hydrogen-disorder aggregates. There have been developed various kinds of hydrogen detection methods employing nuclear collision processes [1]. They are mostly suitable for the detailed depth-profiling but some additional improvements are required to obtain the hydrogen-profile deep inside the samples.

As the first step of this study, the recoil cross sections of ^{4}He ions with ^{1}H were surveyed in the wide energy range. Figure 1 shows the evaluated differential cross sections of the hydrogen recoil process as a function of incident $^{4}He^{2+}$ energy E for 8 different recoil angles φ [2]. One can see the broad resonance nature of recoil cross sections at the ^{4}He ion energy E~9 MeV, which is due to the nuclear elastic scattering of the non-Rutherford type. Also, the cross sections become higher for smaller φ. These are of remarkable difference from the dependences on E and φ in the Rutherford case. At E≅10 MeV, for example, the recoil cross sections are as large as 350 times those in the Rutherford case, so that the detection sensitivity of hydrogen is extremely enhanced. Such advantage probably allows 2-demensional hydrogen mapping by the transmission elastic recoil detection analysis (transmission ERDA [3]) combined with the micro-beam scanning system on the beam line of the 6MV tandem accelerator at UTTAC [4].

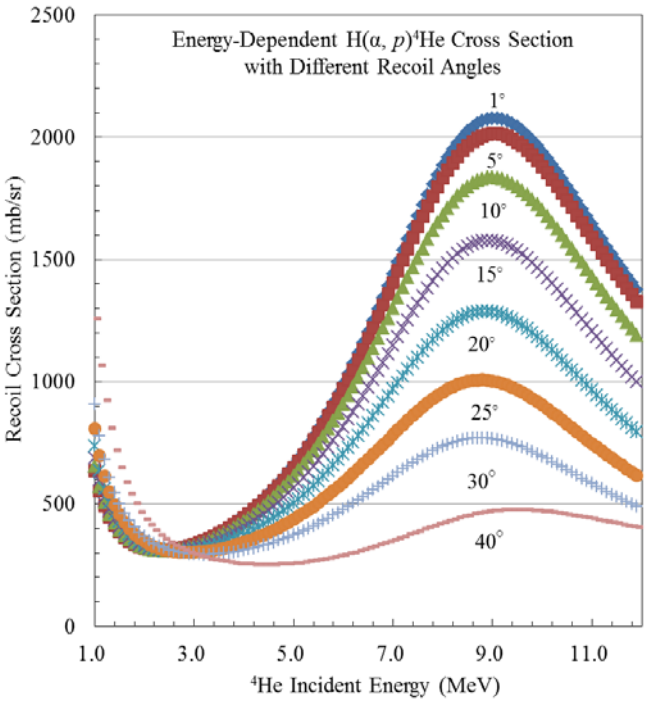

Fig. 1. Evaluated energy dependence of H(α, p)^{4}He recoil cross sections for 8 different recoil angles φ.

In the experiments, 10 MeV $^{4}He^{2+}$ was employed to perform transmission ERDA for an Al film of thickness t=170 μm, which satisfies the condition for the incident $^{4}He^{2+}$ beam to be stopped within the film. The surface barrier detector (SBD) was placed at φ=0°, which covers a fixed solid angle of 1.28 msr. The estimated hydrogen-probing depth is around 40 μm from the Al surface. Figure 2 shows the transmission ERDA spectrum of recoiled hydrogen from the hydrogen-containing standard sample of Kapton (t=7.5 μm)/H-charged Al (t=170 μm), which was measured at φ=0° under the normal incidence of 10 MeV $^{4}He^{2+}$. The observed peak is reasonably in the estimated range between 3.239 and 3.688 MeV, corresponding to

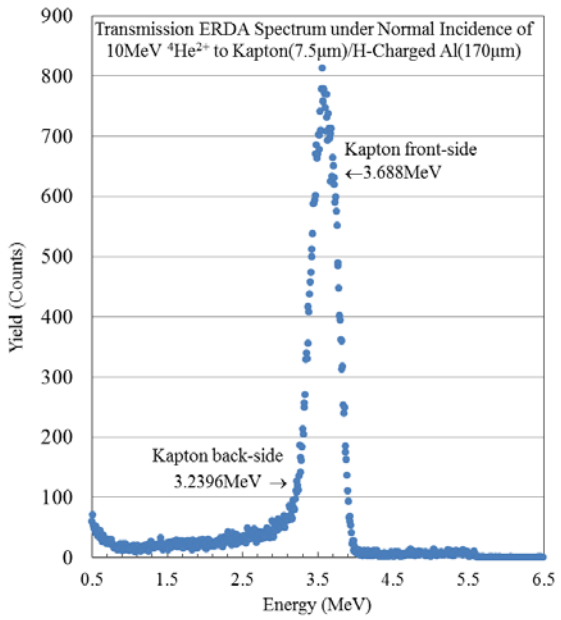

Fig. 2. Transmission ERDA spectrum under the normal incidence of 10 MeV $^{4}He^{2+}$ to Kapton (t=7.5μm) /H-charged Al (t=170μm).

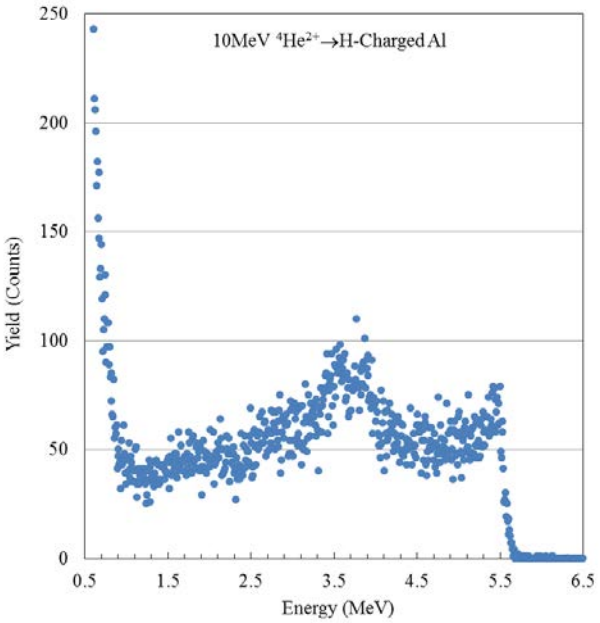

Fig. 3. Transmission ERDA spectrum under the normal incidence of 10 MeV $^{4}He^{2+}$ to H-charged Al (t=170 μm).

the back- and front-side of the Kapton film on H-charged Al, respectively. The step around 5.6 MeV is due to the detectable limit of SBD with the depletion layer of 300 μm thickness. The signal/noise ratio at the hydrogen peak amounts to ~160 and, accordingly, sensitive detection of hydrogen can be expected in the present measurement system. The asymmetric hydrogen peak is attributed to the energy struggling of recoiled hydrogens in the outgoing paths and also to the energy dependence of the recoil cross section. There still remains some background, probably resulting from the nuclear reactions of $^{4}He^{2+}$ with ^{27}Al. For low-noise 2D-profiling, the hydrogen signals should be collected over a larger solid angle.

Figure 3 shows the spectrum from H-charged Al (t=170 μm) film measured under the same conditions as those shown in Fig. 2. The step at 5.6 MeV is already noted earlier, while a sharp hump around 3.8 MeV is attributed to the charged hydrogens which possibly exist as blisters near the surface of the sample [5]. Reproducibility of the results was confirmed from the spectra measured for 7, 8 and 9 MeV $^{4}He^{2+}$. For more detailed analysis, influence of possible nuclear reactions should be investigated.

The authors are indebted to Prof. G. Itoh (Ibaraki University) for providing us hydrogen-charged pure Al films.

References

[1] For example, K. Umezawa et al., Nucl. Instr. Meth. B33 (1988) 634.

[2] IBANDL (Ion Beam Analysis Nuclear Data Library); https://www-nds.iaea.org/exfor/ibandl.htm

[3] J. Tiria et al., Nucl. Instr. Meth. B45 (1990) 147.

[4] A. Yamazaki et al., Nucl. Instr. Meth. B (2017) in press.

[5] T. Manaka et al., Materials Science Forum 879 (2017) 1220.

4.14 Heterogeneous carboxy group distribution across a polyamide active layer of a ESPA2 thin-film composite reverse osmosis membrane

R. Tanaka[1], T. Suzuki[1], M. Niinae[1]

State-of-the-art thin-film composite reverse osmosis (RO) membranes have a composite structure consisting of a nonwoven polyester layer (~50-150 μm) that backs an intermediate layer of polysulfone (~20-50 μm), which in turn supports an active layer of polyamide (< 100 nm) [1]. Among these three layers, the performance of the membrane was mainly determined by a polyamide active layer [2]. However, due to its thin thickness and high surface roughness, it is not easy to obtain information on the physicochemical properties of a polyamide active layer and accordingly, limited information has been reported in the literature about the depth heterogeneity [3]. Therefore, the objective of this study is to measure the concentration of deprotonated carboxy group ($R\text{-}COO^-$) of a polyamide active layer of ESPA2 RO membrane (Nitto Denko Corp.) by probing $R\text{-}COO^-$ with Ag^+. This can actually be performed by quantifying Ag in the sample using X-ray photoelectron spectroscopy (XPS) for very surface of the polyamide and Rutherford backscattering spectrometry (RBS) for average across the polyamide.

All solutions were prepared using distilled deionized water with resistivity greater than 18 MΩ·cm (WA200, Yamato Scientific Co., Ltd., Tokyo, Japan). All reagents were purchased at guaranteed reagent grade quality from Nacalai Tesque, Inc. (Kyoto, Japan) or Wako Pure Chemical Industries, Ltd. (Osaka, Japan) and used without further purification. Saturation of $R\text{-}COO^-$ with Ag^+ was performed according to the procedures reported in the literature [3]. The elemental composition of the polyamide back surface was measured using a K-Alpha™⁺ XPS system (Thermo Fisher

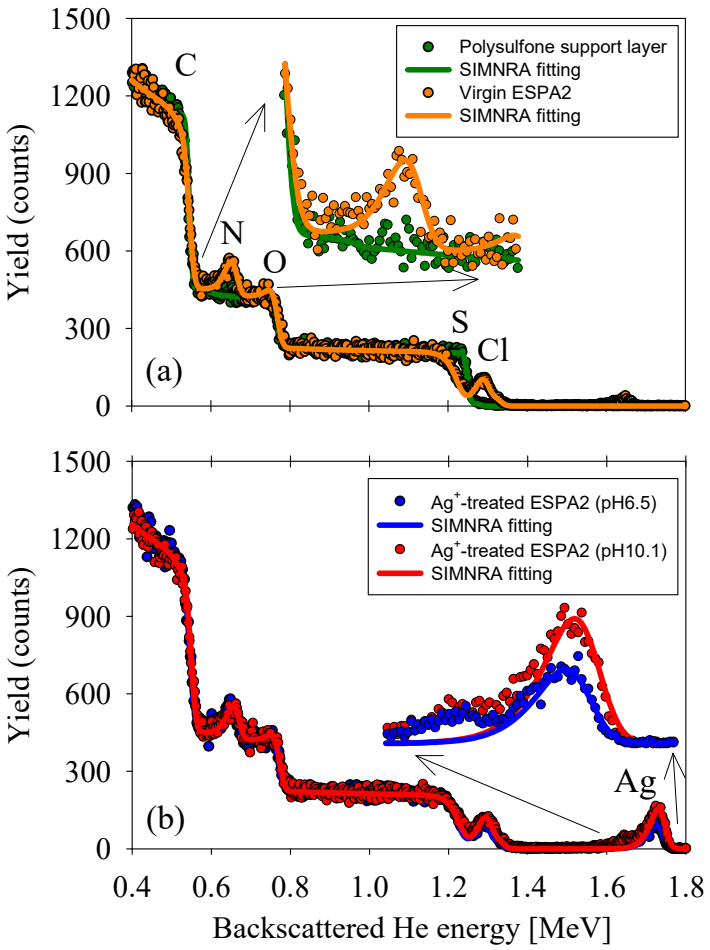

Fig. 1. RBS spectra obtained for (a) polysulfone support and virgin ESPA2 membranes, and (b) Ag^+-treated ESPA2 membranes at pH6.5 and pH10.1. The average and standard deviation in Gamma distribution of active layer thickness were determined from the nitrogen peak, oxygen peak, and the energy shift of the frontal peak for sulfur.

[1] Yamaguchi University

Scientific Inc., Waltham, MA), whereas those for the polyamide entire layer were measured by RBS using 2MeV $^{4}He^{2+}$ from 1MV Tandetron at University of Tsukuba.

RBS spectra obtained for (a) polysulfone support and virgin ESPA2 membranes, and (c) Ag^{+}-treated ESPA2 membranes at pH6.5 and pH10.1 are shown in Fig. 1. As shown in Fig. 1, the peak intensity of Ag is higher at pH10.1 than that at pH6.5, which means more fraction of R-COOH was deprotonated at higher pH. The RBS spectra were analyzed using the software SIMNRA to obtain elemental compositions and other physicochemical properties of active layers. The concentrations of deprotonated carboxy group ($R\text{-}COO^{-}$) in the polyamide active layers of ESPA2 membrane as a function of aqueous pH was summarized in Fig. 2. The comparison of Ag profiles measured by these two analytical methods revealed that the concentration of $R\text{-}COO^{-}$ at the surface is higher than the average value across polyamide. This result can be interpreted that the concentration of $R\text{-}COO^{-}$ in polyamide active layer is highest at the surface, and gradually decreases with distance from the surface.

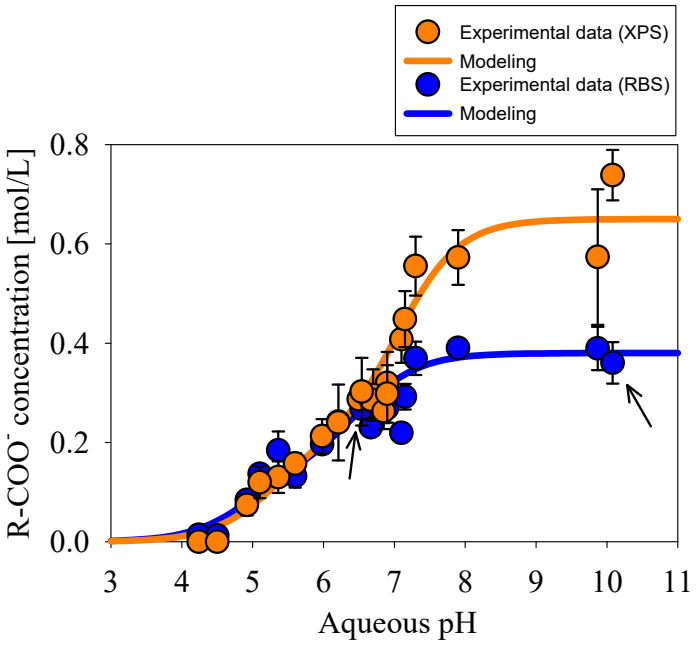

Fig. 2. Concentrations of deprotonated carboxy group ($R\text{-}COO^{-}$) in the polyamide active layers of ESPA2 membrane as a function of aqueous pH. Orange circles represent $R\text{-}COO^{-}$ concentrations near the active layer surface measured by XPS, and blue circles represent average $R\text{-}COO^{-}$ concentrations in the active layer measured by RBS. Error bars indicate standard deviation of triplicate. Continuous lines represent the modeling results. The RBS spectra for samples indicated by arrows are shown in Fig. 1.

References

[1] T. Suzuki et al., Water Res. 100 (2016) 326.

[2] R. J. Petersen, J. Membr. Sci. 83 (1993) 81.

[3] O. Coronell et al., Environ. Sci. Technol. 45 (2011) 4513.

4.15 Relationship between the abrasion of DLC coated layer and its hydrogen content

Y. Yoshida[1], S. Kunitsugu[2]

In the automobile industry, improvement of fuel consumption has become an urgent matter from the viewpoint of the demand for reduction of global greenhouse gas emission. For improvement of fuel consumption, it is necessary to improve such items as the heat efficiency of engine and drive wheels, or the vehicle body weight. Above all, friction due to sliding between car parts occupies a large proportion of energy loss, and therefore, reducing friction loss is one of the important items for improving fuel consumption.

There are two approaches to reduce the friction loss of the sliding parts. One is to lower the stirring resistance with low-viscosity car oils, and another is to improve the wear resistance of car parts by applying coatings that reduce their friction coefficients. Actually, automobile industries have attempted to reduce friction by the above two approaches, especially employing the diamond-like carbon (DLC) coating. DLC is an amorphous carbon film with different fractions of sp^3 and sp^2 bonds, and is applied to molds and mechanical parts because it has low friction and wear resistance.

DLC should wear when car parts slide with each other, however until now, there has been no detailed report on the relationship between the wear and the hydrogen (H) concentration in DLC. Among the DLC deposition methods, the cathodic arc (CA) deposition method can deposit DLC with the H concentration of 5% or less. Furthermore, if a gas containing H is used as the plasma source, it is possible to control the H concentration. In this work, we prepared DLC with different H-adding acetylene (C_2H_2) gases using cathodic arc method and investigated their wear characteristics.

Hydrogen free DLC (ta-C; tetrahedral amorphous carbon) coatings were made on the steel disk by means of CA method using single gas of argon (Ar) as a plasma source, as illustrated in Fig. 1. Next, in order to make a hydrogenated DLC (ta-C:H; Hydrogenated tetrahedral amorphous carbon), we also used a mixture gas of Ar / C_2H_2 as a plasma source. The pressure in the chamber was fixed at 0.2 Pa and the C_2H_2 gas flow was varied as 0, 10, 60 sccm.

The hydrogen concentrations in the DLC coating films were determined by Elastic Recoil Detection Analysis (ERDA) and Rutherford Backscattering Spectrometry (RBS), using 2.5 MeV $^4He^{2+}$ obtained from the Tandetron accelerator at UTTAC. For friction and wear tests, a SRV test system (SRV IV, Optimol instruments) was used with a reciprocating ball-on-disk configuration, shown in Fig. 2. We dropped car oil on the steel disk coated with DLC. A reciprocating frequency of 50.0 Hz and a sliding distance of 180 m were chosen for the test condition.

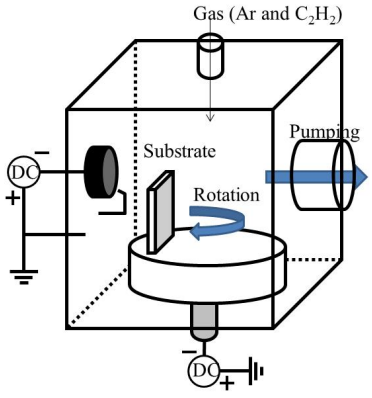

Fig. 1. Schematic diagram of cathodic arc deposition system.

[1] TOYO advanced technologies Co., Ltd.
[2] Industrial Technology Center of Okayama Prefecture

Figures 3 and 4 show the ERDA spectrum of DLC and the correlation of H concentration with C_2H_2 flow rate, respectively. When single Ar gas was used for arc discharge, the H concentration in DLC was 0.3 %. Even when DLC was deposited using a mixed gas in which C_2H_2 was added to Ar at 10 sccm, the H concentration remained at 0.3%. When the flow rate of C_2H_2 was increased to 60 sccm, the yield of ERDA spectrum increased remarkably and in this case the H concentration was as high as 3.0%.

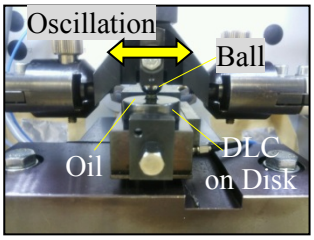

Fig. 2. Schematic diagram of the SRV test system.

The friction and abrasion test was carried out for these DLC samples. Figure 5 shows optical microscopic image of worn surface on DLC. Figure 6 shows the correlation between hydrogen concentration and wear coefficient. The measured values of wear coefficient for the DLC samples are 6.6×10^{-12} and 2.8×10^{-11} $mm^3/(N\times mm)$ for H concentration of 0.3%, while it is 5.7×10^{-11} $mm^3/(N\times mm)$ for H concentration of 3.0%.

In this study, the abrasion effect of H concentrations of only 3% or less was investigated. We will further investigate the abrasion process by increasing the H concentration in DLC.

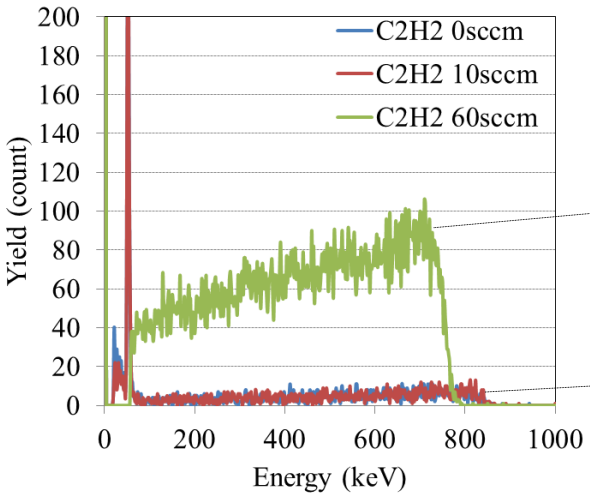

Fig. 3. ERDA spectrum of DLC.

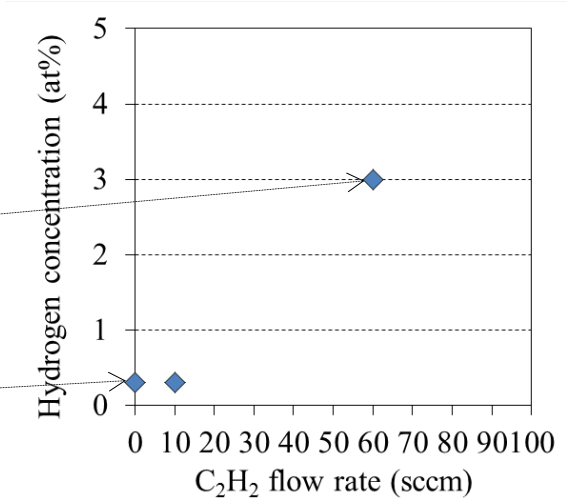

Fig. 4. Correlation between hydrogen content and C_2H_2 flow rate.

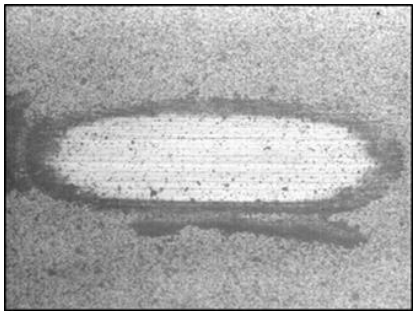
Fig. 5. Optical microscopic image of worn surface on DLC.

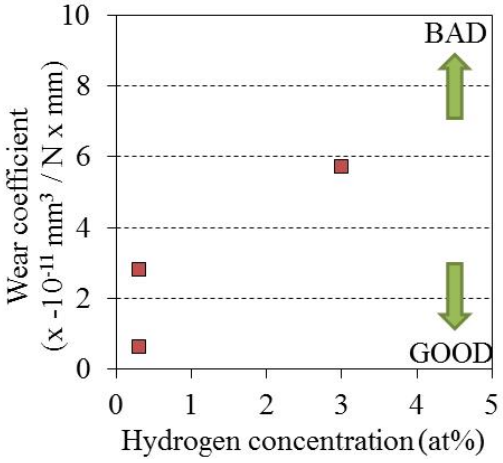

Fig. 6. correlation between hydrogen content and wear coefficient.

4.16 Measurement of hydrogen content in DLC films

T. Imai[1], T. Harigai[1], H. Takikawa[1]

Diamond-like carbon (DLC) films have amorphous structure composed of sp^2 hybridized and sp^3 hybridized bonds. DLC films have been used widely for applications in industry because DLC films have excellent properties such as high mechanical hardness and chemical inertness. DLC films can be classified into four groups depending on the combinations between bonding nature and hydrogen contents: 1) tetrahedral amorphous carbon (ta-C) films with dominant sp^3 bonds and less hydrogen, 2) amorphous carbon (a-C) films with dominant sp^2 bonds and less hydrogen, 3) hydrogenated tetrahedral amorphous carbon (ta-C:H) films, and 4) hydrogenated amorphous carbon (a-C:H) films.

Currently, the standardization on DLC films have been actively discussed, and "Carbon based films -Classification and designation" has been proposed to the TC107 secretariat [1]. In the project proposal, DLC films are classified by using the sp^3 bond fraction ($sp^3/[sp^3+sp^2]$) and the hydrogen content obtained from the NEXAFS and the RBS/ERDA measurements, respectively. However, it is difficult to introduce these measurement methods as the DLC film analysis at the actual product due to high cost. Therefore, the classification method based on optical constants measured by spectroscopic ellipsometry has been proposed as a simpler and cheaper method [2]. In this experiment, the hydrogen content in DLC films prepared using the T-shape filtered arc deposition (T-FAD) system is evaluated quantitatively for verification of the classification by optical constants and other classification methods.

DLC films were fabricated on Si substrates by the T-FAD. Graphite was used as a cathode. The species and the flow rate of introduction gas (hydrogen, ethylene, and acetylene) to a chamber and the applied bias voltage to the substrate were changed systematically. The contents of hydrogen and carbon were analyzed using elastic recoil detection analysis（ERDA）at a recoil angle of 30° and Rutherford backscattering spectrometry (RBS) at a scattering angle of 150°, respectively. 2.5 MeV $^4He^{2+}$ obtained from 1MV Tandetron at UTTAC was used for RBS/ERDA.

Figure 1 shows RBS and ERDA spectra for a DLC (ta-C) film prepared without gas introduction. Those for a DLC (a-C:H) film prepared with ethylene gas introduced at 20 sccm are shown in Fig. 2. In both cases, similar RBS spectra are observed. On the other hand, ERDA spectra are different. ERDA spectrum in Fig. 1 shows negligible hydrogen signals at 430–460 channels which are attributed to hydrogen components of water molecules adsorbed on the surface. In contrast, hydrogen signals are observed definitely in Fig. 2. The hydrogen content in the DLC film was determined using simulation software SIMNRA. It was found that the hydrogen content increased with the flow rate increase of the hydrocarbon gas. This is because the number of hydrogen atoms contributing to the film growth increase with increasing the flow rate of the introduced gases. However, when the substrate bias voltage was applied, the hydrogen content in the films decreased with the introduction of ethylene and acetylene gas, and the hydrogen content increased with the introduction of hydrogen gas. The decrease of hydrogen content with the introduction of ethylene and acetylene gas would be associated with the hydrogen-bond

[1] Toyohashi University of Technology

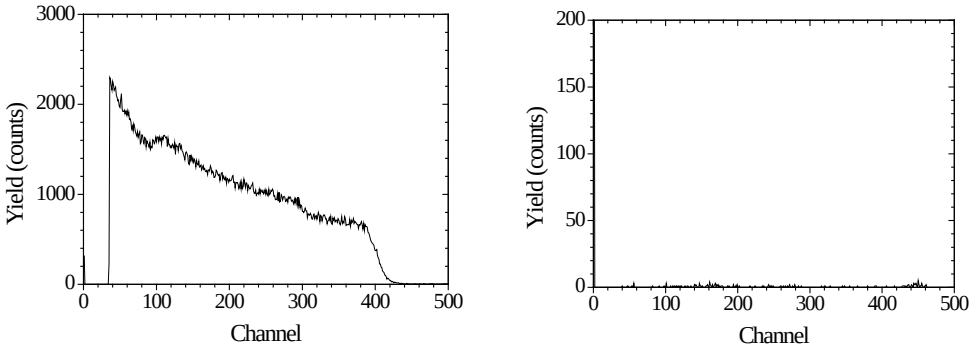

Fig. 1. RBS (left) and ERDA (right) spectra of hydrogen-free DLC film formed without gas introduction.

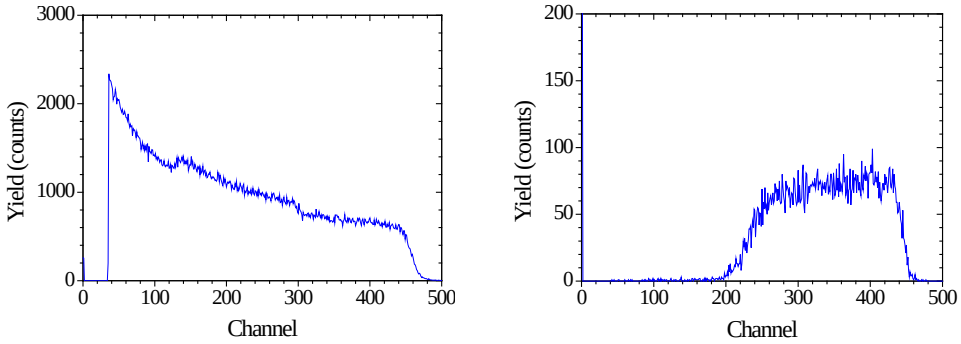

Fig. 2. RBS (left) and ERDA (right) spectra of hydrogenated DLC film formed by introducing 20 sccm of ethylene.

release by the bombardments of carbon ions and hydrocarbon ions in the near surface region under the applied bias voltage. In the hydrogen gas introduction, it can be considered that hydrogen desorption by ion bombardment effect was small because the average ion size was small in the chamber atmosphere.

On the proposed classification method, the films with the hydrogen content more than 5 at.% are classified into hydrogenated DLC films (ta-C:H or a-C:H), and the films with the hydrogen content less than 5 at % are classified into hydrogen-free DLC films (ta-C or a-C). From this experiment, we have found that ta-C or a-C films can be formed by the hydrogen-gas introduction at a flow rate of less than 30 sccm, and that ta-C or a-C films are obtained by acetylene- or ethylene-gas introduction at a flow rate of more than 30 sccm.

Finally, it is concluded that the hydrogen content of hydrogen-free DLC films and hydrogenated DLC films prepared using a T-FAD method can be determined quantitatively by RBS/REDA measurement. Based on these results, we will evaluate the classification method of DLC films by optical constants, and will also propose other classification methods.

References

[1] A. Tanaka, N. Ohtake, NEW DIAMOND, 32(4) (2016) 3, in Japanese.

[2] M. Hiratsuka et al., J. Sol. Mech. Mater. Eng. 7 (2013) 187.

5.

BEAM IRRADIATION EFFECT

5.1 Tolerance evaluation on single event of COTS-GNSS receivers

M. Komatsu[1]

For launch of space rocket in Japan, the Global Navigation Satellite System (GNSS) receiver currently plays an important role [1, 2]. On the other hand, to respond to the market needs of reducing costs of space launchers, it is urgent to develop compact, lightweight, and inexpensive space GNSS receivers. Currently, R&D dept. of JAXA aims to construct low-cost and high-accuracy GNSS positioning system for space launchers, utilizing COTS (Commercial off-the-shelf)-GNSS receivers.

In this research, the SEE (Single Event Effect) immunity was evaluated for three different COTS-GNSS receivers (A, B, C). Figure 1 shows an example of plots of linear energy transfer (LET) vs. cross section of SEFI (Single Event Function Interrupt). The experiment was performed for three different LETs, and the cross sections were calculated from the total fluence and the endurance time, from test start to SEE detection. During this evaluation, a GNSS signal player GSS6425 was used to generate and input GNSS signal for these receivers (Fig. 2), and they were kept functioning – i.e., 3D positioning state.

The form of single event varied depending on the device of GNSS receivers. It was confirmed that Receiver A was particularly vulnerable to SEFI. Since SEFI occurred at a high frequency, the single event upset (SEU) cross section is unable to evaluate accurately, but it is considered that the probability of its occurrence is lower than that of SEFI. For Receiver B, it was found that SEFI and SEU occurred with about the same probability. For receiver C, SEU occurred frequently, while SEFI did not. The single event latch up (SEL) did not occur for any receiver. In the actual receiver system designing, information on the form of SEE generated in each device determines the design policy in terms of what kind of backup / redundant system is to be constructed.

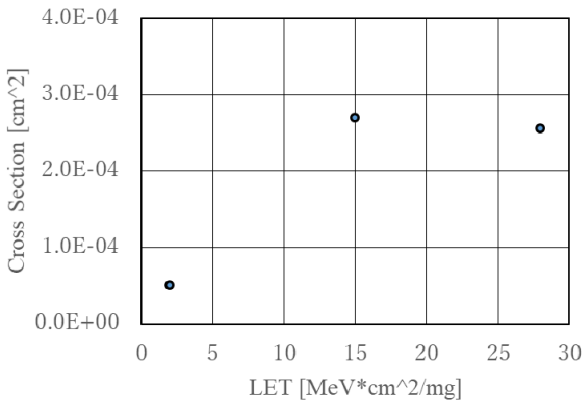

Fig. 1. LET vs. SEFI Cross Section of Receiver A.

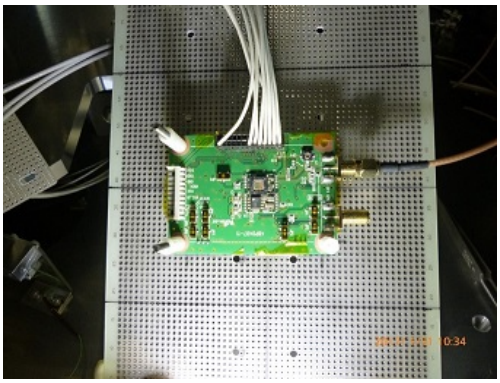

Fig. 2. Test configuration of GNSS Receiver A.

References

[1] Pratap Misra and Per Enge, “Global Positioning System”, 2nd Edition, 2006.

[2] S. Yamazaki et al., “New Effective Multipath Mitigation and Initial Assessment of the Radio and Inertial Navigation Sensor ("RINA")”, Proceedings of the 29th ION GNSS, Sept. 12-16, 2016.

[1] Japan Aerospace Exploration Agency

5.2 Preliminary evaluation of single event testing for regular use of the 6 MV tandem accelerator at University of Tsukuba

A.Maru[1], H. Shindou[1], K. Suzuki[1], M. Sataka, K. Sasa

For electronic devices used in space, it is of technical importance to evaluate their radiation tolerance. Influence of radiation on semiconductor devices is mainly categorized into either “single event effect” or “total dose effect”. Tolerance of the electronic devices against these two effects must be evaluated before using them in space. While the total dose test is generally performed by using gamma rays from radioisotope sources, the single event test is performed by using energetic heavy ions which are obtained from particle accelerators. In the latter case, several kinds of heavy ions having various energies and enough projected ranges are needed because the electronic devices in space are exposed to many kinds of energetic heavy ions.

Soon after the 6 MV Pelletron tandem accelerator was installed at University of Tsukuba in 2014, UTTAC built the beam line with the 1-m diameter vacuum chamber, as shown in Fig. 1, for dedicated use for beam irradiation experiments not only by internal, but also by external users. With such improved experimental environment, JAXA has started preliminary evaluation to use this beam line for single event testing. Figure 2 shows the species and energies of ions available at the UTTAC 6 MV tandem accelerator [1], which allows selection of the heavy ions used for the single event testing. Before the testing, we evaluated effective LET (Liner Energy Transfer) and projected ranges of heavy ions inside the semiconductor devices by using SRIM (The Stopping and Range of Ions in Matter) code [2]. Under the collaboration of JAXA and UTTAC, we introduced the beam scattering foil to form a uniformly distributed ion beam and also installed the equipment characterizing the ion current distribution and ion energy distribution for an accurate evaluation.

Fig. 1. The beam irradiation system at UTTAC.

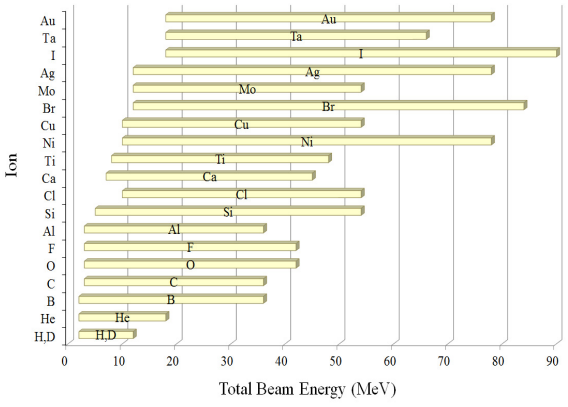

Fig. 2. Species and energies of ions available at UTTAC, reproduced from Ref. 1.

In the present work at UTTAC, the irradiation test for the device of simple 8k bit latch memory circuits was performed using 42 MeV Si ions and 36 MeV O ions. The results can be compared directly

[1] Japan Aerospace Exploration Agency (JAXA)

with those for the same device, obtained previously at Takasaki Ion Accelerators for Advanced Radiation Application (TIARA) facility. Figure 3 shows comparison of the single event upset (SEU) cross sections as a function of linear energy transfer (LET), together with the Weibull fitting curve. This demonstrates that the data taken at the two facilities are consistent and, accordingly, assures that reliable radiation tolerance tests for electronic devices used in space can be extended at UTTAC.

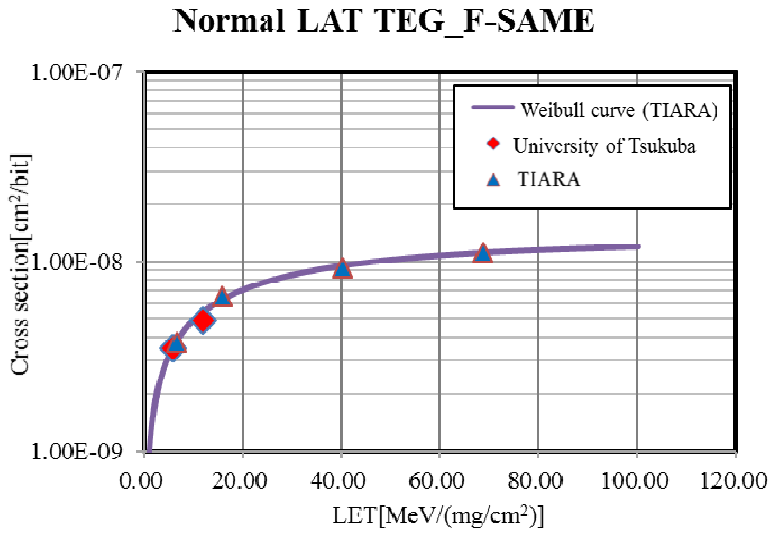

Fig. 3. SEU cross sections as a function of LET, determined from the experiments at UTTAC and TIARA. Also shown is the Weibull fitting curve.

References

[1] 2016 version of the brochure of University of Tsukuba Tandem Accelerator Complex, http://web2.tac.tsukuba.ac.jp/uttac/6MV-tandem

[2] J. F. Ziegler, SRIM (The Stopping and Range of Ions in Matter) simulator, http://www.srim.org/

5.3 Effect of helium irradiation on tritium permeability of erbium oxide

W. Mao[1], N.Breton[1], H. Matsuzaki[1], T. Terai[1]

To limit tritium leakages in a breeding blanket of fusion reactor, a tritium permeation barrier can be used. Erbium oxide was selected as a promising candidate with a low tritium permeability. Thus, the purpose of this study is to understand the irradiation effect of helium ions, originating from fission of lithium exposed to fusion-induced neutrons in the blanket, on the tritium permeability of erbium oxide [1].

To meet this objective, an erbium oxide of approximately 600 nm thickness was deposited on the substrate with the same quality as blanket materials. After division into subsamples, halves were irradiated to 1–3 displacement per atom (dpa) with 0.4 MeV $^4He^+$ from the 1MV Cockcroft-Walton accelerator at UTTAC. The irradiation conditions are chosen so as to meet mathematical models of lithium blanket, in which the stopping and ranges of ions in matters (SRIM) was used for the irradiation damage calculation. The samples were annealed at 773-973 K under hydrogen atmosphere (0.4 bar), as a safe substitute of tritium exposure. Through the nuclear reaction analysis of hydrogen, we will be able to obtain the depth profile of diffused hydrogen during the annealing period, from which information on the permeability for different samples is obtainable. Influence of irradiation on the hydrogen permeation reduction capacities of erbium oxide could be quantified for non-irradiated and irradiated samples, as shown in Figure 1. Future experiments and analysis are now under way.

In conclusion, the rise of permeability due to the irradiation seems serious in blanket operation. In the next stage, the permeation study will be required using tritium itself to assert the promising nature of erbium oxide, together with the structural analysis of irradiated erbium oxide.

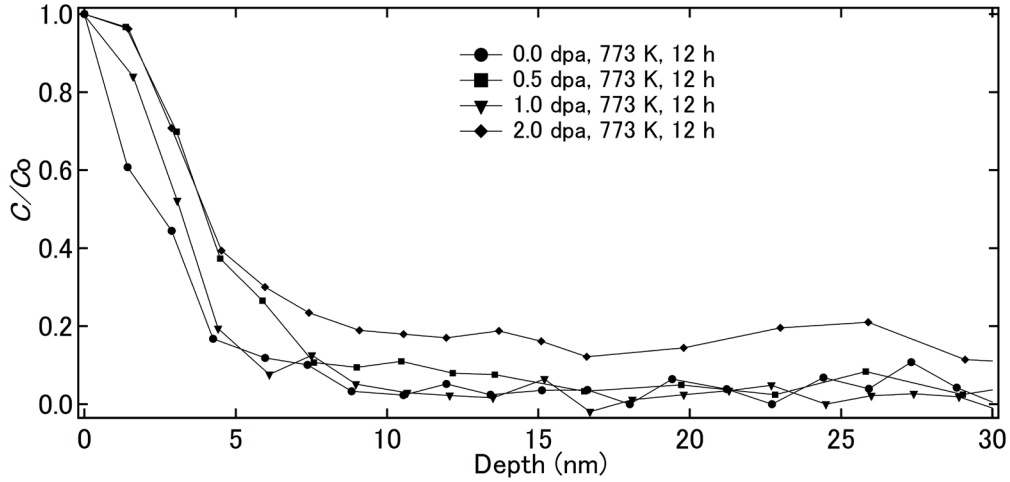

Fig. 1. Irradiation dose dependence of normalized hydrogen concentration profile (C) for samples annealed at 773 K for 12h. C_o is the surface concentration of hydrogen.

Reference

[1] A. Raffray et al., J. Nucl. Mater. 307 (2002) 21.

[1] The University of Tokyo

6.

PUBLICATIONS

6.1 Journals

ACCELERATOR AND RELATED FACILITIES

1. A. Yamazaki, K. Sasa, S. Ishii, M. Kurosawa, S. Tomita, Y. Shiina, S. Shiki, G. Fujii, M. Ukibe, M. Ohkubo, A. Uedono, E. Kita, Development of a microbeam PIXE system for additive light elements in structural materials, Nuclear Instruments and Methods in Physics Research B404 (2017) 92-95.

NUCLEAR AND ATOMIC PHYSICS

1. R. Knobel, M. Diwisch, F. Bosch, D. Boutin, L. Chen, C. Dimopoulou, A. Dolinskii, B. Franczak, B. Franzke, H. Geissel, M. Hausmann, C. Kozhuharov, J. Kurcewicz, S.A. Litvinov, G. Martinez-Pinedo, M. Matos, M. Mazzocco, G. Munzenberg, S. Nakajima, C. Nociforo, F. Nolden, T. Ohtsubo, A. Ozawa, Z. Patyk, W.R. Plaß, C. Scheidenberger, J. Stadlmann, M. Steck, B. Sun, T. Suzuki, P.M. Walker, H. Weick, M.-R. Wu, M. Winkler, T. Yamaguchi, First direct mass measurements of stored neutron-rich ^{129,130,131}Cd isotopes with FRS-ESR, Physics Letters B 754 (2016) 288–293.

2. A. Kusoglu, G. Georgiev, C. Sotty, D. L. Balabanski, A. Goasduff, Y. Ishii, Y. Abe, K. Asahi, M. Bostan, R. Chevrier, M. Chikamori, J. M. Daugas, T. Furukawa, H. Nishibata, Y. Ichikawa, Y. Ishibashi, R. Lozeva, H. Miyatake, D. Nagae, T. Nanao, M. Niikura, T. Niwa, S. Okada, A. Ozawa, Y. Saito, H. Shirai, H. Ueno, D. T. Yordanov, and N. Yoshida, Magnetic moment of the 13/2+ isomeric state in ^{69}Cu: Spin alignment in theone-nucleon removal reaction, Physical Review C 93, 054313 (2016).

3. R. Knobel, M. Diwisch, H. Geissel, Yu.A. Litvinov, Z. Patyk, W.R. Plaß, C. Scheidenberger, B. Sun, H. Weick, F. Bosch, D. Boutin, L. Chen, C. Dimopoulou, A. Dolinskii, B. Franczak, B. Franzke, M. Hausmann, C. Kozhuharov, J. Kurcewicz, S.A. Litvinov, M. Matos, M. Mazzocco, G. Munzenberg, S. Nakajima, C. Nociforo, F. Nolden, T. Ohtsubo, A. Ozawa, J. Stadlmann, M. Steck, T. Suzuki, P.M. Walker, M. Winkler, and T. Yamaguchi, New results from isochronous mass measurements of neutron-rich uranium fission fragments with the FRS-ESR-facility at GSI, Eur. Phys. J. A (2016) 52: 138 (11 page).

4. D. Q. Fang, Y. G. Ma, X. Y. Sun, P. Zhou, Y. Togano, N. Aoi, H. Baba, X. Z. Cai, X. G. Cao, J. G. Chen, Y. Fu, W. Guo, Y. Hara, T. Honda, Z. G. Hu, K. Ieki, Y. Ishibashi, Y. Ito, N. Iwasa, S. Kanno, T. Kawabata, H. Kimura, Y. Kondo, K. Kurita, M. Kurokawa, T. Moriguchi, H. Murakami, H. Ooishi, K. Okada, S. Ota, A. Ozawa, H. Sakurai, S. Shimoura, R. Shioda, E. Takeshita, S. Takeuchi, W. D. Tian, H. W. Wang, J. S. Wang, M. Wang, K. Yamada, Y. Yamada, Y. Yasuda, K. Yoneda, G. Q. Zhang, and T. Motobayashi, Proton-proton correlations in distinguishing the two-proton emission mechanism of ^{23}Al and ^{22}Mg, Physical Review C 94, 044621 (2016).

5. X. Xu, P. Zhang, P. Shuai, R. J. Chen, X. L. Yan, Y. H. Zhang, M. Wang, Yu. A. Litvinov, H. S. Xu, T. Bao, X. C. Chen, H. Chen, C. Y. Fu, S. Kubono, Y. H. Lam, D. W. Liu, R. S. Mao, X. W. Ma, M. Z. Sun, X. L. Tu, Y. M. Xing, J. C. Yang, Y. J. Yuan, Q. Zeng, X. Zhou, X. H. Zhou, W. L. Zhan, S. Litvinov, K. Blaum, G. Audi, T. Uesaka, Y. Yamaguchi, T. Yamaguchi, A. Ozawa, B. H. Sun, Y. Sun, A. C. Dai, and F. R. Xu, Identification of the Lowest T = 2, Jπ = 0+ Isobaric Analog State in ^{52}Co and Its Impact on the Understanding of β-Decay Properties of ^{52}Ni, Physical Review Letters, 117, 182503 (2016).

6. D. T. Tran, H. J. Ong, T. T. Nguyen, I. Tanihata, N. Aoi, Y. Ayyad, P. Y. Chan, M. Fukuda, T. Hashimoto, T. H. Hoang, E. Ideguchi, A. Inoue, T. Kawabata, L. H. Khiem, W. P. Lin, K. Matsuta, M. Mihara, S. Momota, D. Nagae, N. D. Nguyen, D. Nishimura, A. Ozawa, P. P. Ren, H. Sakaguchi, J. Tanaka, M. Takechi, S. Terashima, R. Wada, and T. Yamamoto, Charge-changing cross-section measurements of $^{12–16}$C at around 45A MeV and development of a Glauber model for incident energies 10 A–2100 A MeV, Physical Review C 94, 064604 (2016).

7. S. Kimura, H. Ishiyama, H. Miyatake, Y. Hirayama, Y.X. Watanabe, H.S. Jung, M. Oyaizu, M. Mukai, S.C. Jeong, A. Ozawa, Development of the detector system for β-decay spectroscopy at the KEK Isotope Separation System, Nuclear Instruments and Methods in Physics Research B 376 (2016) 338–340.

8. P. Schury, M. Wada, Y. Ito, D. Kaji, F. Arai, M. MacCormick, I. Murray, H. Haba, S. Jeong, S. Kimura, H. Koura, H. Miyatake, K. Morimoto, K. Morita, A. Ozawa, M. Rosenbusch, M. Reponen, P.-A. Soderstrom, A. Takamine, T. Tanaka, and H. Wollnik, First online multireflection time-of-flight mass measurements of isobar chains produced by fusion-evaporation reactions: Toward identification of superheavy elements via mass spectroscopy, Physical Review C 95, 011305(R) (2017).

9. K. Sawahata, A. Ozawa, Y. Saito, Y. Abe, Y. Ichikawa, N. Inaba, Y. Ishibashi, A. Kitagawa, S. Matsunaga, T. Moriguchi, D. Nagae, S. Okada, S. Sato, S. Suzuki, T. Suzuki, Y. Takeuchi, T. Yamaguchi, J. Zenihiro, Investigations of charge-changing processes for light proton-rich nuclei on carbon and solid-hydrogen targets, Nuclear Physics A 961 (2017) 142–153.

10. M. Mukai, Y. Hirayama, H. Ishiyama, H. S. Jung, H. Miyatake, M. Oyaizu, Y. X. Watanabe, S. Kimura, A. Ozawa, S. C. Jeong, T. Sonoda, Search for efficient laser resonance ionization schemes of tantalum using a newly developed time-of-flight mass-spectrometer in KISS, Nuclear Instruments and Methods in Physics Research B 376 (2016) 73-76.

ACCELERATOR MASS SPECTROMETRY

1. Yukihiko Satou, Keisuke Sueki, Kimikazu Sasa, Kouji Adachi, Yasuhito Igarashi, First successful isolation of radioactive particles from soil near the Fukushima Daiichi Nuclear Power Plant, Anthropocene, 14 (2016) 71-76. DOI:10.1016/j.ancene.2016.05.01

2. Kenji Kawamura, Ayako Abe-Ouchi, Hideaki Motoyama, Yutaka Ageta, Shuji Aoki, Nobuhiko Azuma, Yoshiyuki Fujii, Koji Fujita, Shuji Fujita, Kotaro Fukui, Teruo Furukawa, Atsushi Furusaki, Kumiko Goto-Azuma, Ralf Greve, Motohiro Hirabayashi, Takeo Hondoh, Akira Hori, Shinichiro Horikawa, Kazuho Horiuchi, Makoto Igarashi, Yoshinori Iizuka, Takao Kameda, Kokichi Kamiyama, Hiroshi Kanda, Mika Kohno, Takayuki Kuramoto, Yuki Matsushi, Morihiro Miyahara, Takayuki Miyake, Atsushi Miyamoto, Yasuo Nagashima, Yoshiki Nakayama, Takakiyo Nakazawa, Fumio Nakazawa, Fumihiko Nishio, Ichio Obinata, Rumi Ohgaito, Akira Oka, Jun'ichi Okuno, Junichi Okuyama, Ikumi Oyabu, Frédéric Parrenin, Frank Pattyn, Fuyuki Saito, Takashi Saito, Takeshi Saito, Toshimitsu Sakurai, Kimikazu Sasa, Hakime Seddik, Yasuyuki Shibata, Kunio Shinbori, Keisuke Suzuki, Toshitaka Suzuki, Akiyoshi Takahashi, Kunio Takahashi, Shuhei Takahashi, Morimasa Takata, Yoichi Tanaka, Ryu Uemura, Genta Watanabe, Okitsugu Watanabe, Tetsuhide Yamasaki, Kotaro Yokoyama, Masakazu Yoshimori, Takayasu Yoshimoto, State dependence of climatic instability over the past 720,000 years from Antarctic ice cores and climate modelling, Science Advances, 08 Feb 2017, Vol. 3, no. 2, e1600446. DOI: 10.1126/sciadv.1600446

3. Seiji Hosoya, Kimikazu Sasa, Tetsuya Matsunaka, Tsutomu Takahashi, Masumi Matsumura, Hiroshi Matsumura, Mark Sundquist, Mark Stodola, Keisuke Sueki, Optimization of a ΔE − E detector for ^{41}Ca AMS, Nuclear Instruments and Methods in Physics Research B, 406 (2017) 268-271.

BEAM AND ISOTOPE APPLICATIONS

1. Masanori Kurosawa, Kimikazu Sasa, Ki-Choel Shin, Satoshi Ishii, Trace-element compositions and Br/Cl ratios of fluid inclusions in the Tsushima granite, Japan: Significance for formation of granite-derived fluids, Geochimica et Cosmochimica Acta, 182 (2016) 216–239. doi:10.1016/j.gca.2016.03.015

2. A. Uedono, M. Zhao, and E. Simoen, Probing the effect of point defects on the leakage blocking capability of Al0.1Ga0.9N/Si structures using a monoenergetic positron beam, J. Appl. Phys. 120, 215702(1-7) (2016). [DOI: 10.1063/1.4970984]

3. A. Uedono, M. Malinverni, D. Martin, H. Okumura, S. Ishibashi, and N. Grandjean, Vacancy-type defects in Mg-doped GaN grown by ammonia-based molecular beam epitaxy probed using a monoenergetic positron beam, J. Appl. Phys. 119, 245702(1-6) (2016). [DOI: 10.1063/1.4954288]

4. A. Uedono, Y. Tsukada, Y. Mikawa, T. Mochizuki, H. Fujisawa, H. Ikeda, K. Kurihara, K. Fujito, S. Terada, S. Ishibashi, and S. F. Chichibu, Vacancies and electron trapping centers in acidic ammonothermal GaN probed by a monoenergetic positron beam, J. Cryst. Growth 448, 117-121 (2016). [DOI: 10.1016/j.jcrysgro.2016.05.015]

5. W. Zhu, B. Mitchell, D. Timmerman, A. Uedono, A. Koizumi, and Y. Fujiwara, Enhanced photo/electroluminescence properties of Eu-doped GaN through optimization of the growth temperature and Eu related defect environment, APL Mater. 4, 056103(1-7) (2016). [doi: http://dx.doi.org/10.1063/1.4950826]

6. S. Hooda, S. A. Khan, B. Satpati, A. Uedono, S. Sellaiyan, K. Asokan, D. Kanjilal, D. Kabiraj, Nanopores formation and shape evolution in Ge during intense ionizing irradiation, Microporous and Mesoporous Mat. 225, 323-330 (2016). [doi:10.1016/j.micromeso.2016.01.006]

7. A. Uedono, M. M. Islam, T. Sakurai, C. Hugenschmidt, W. Egger, R. Scheer, R. Krause-Rehberg, K. Akimoto, Vacancy behavior in Cu(In1−xGax)Se2 layers grown by a three-stage coevaporation process probed by monoenergetic positron beams, Thin Solid Films 603, 418-423 (2016). [DOI: 10.1016/j.tsf.2016.02.057]

8. K. Kojima, Y. Tsukada, E. Furukawa, M. Saito, Y. Mikawa, S. Kubo, H. Ikeda, K. Fujito, A. Uedono, and S. F. Chichibu, Electronic and optical characteristics of an m-plane GaN single crystal grown by hydride vapor phase epitaxy on a GaN seed synthesized by the ammonothermal method using an acidic mineralizer, Jpn. J. Appl. Phys. 55, 05FA03(1-4) (2016). [DOI: 10.7567/JJAP.55.05FA03]

9. A. Uedono, S. Armini, Y. Zhang, T. Kakizaki, R. Krause-Rehberg, W. Anwand, A. Wagner, Surface sealing using self-assembled monolayers and its effect on metal diffusion in porous low-k dielectrics studied using monoenergetic positron beams, Appl. Surf. Sci. 368, 272-276 (2016). [DOI:10.1016/j.apsusc.2016.01.267]

10. S. F. Chichibu, K. Kojima, Y. Yamazaki, K. Furusawa, and A. Uedono, “Controlling the carrier lifetime of nearly threading-dislocation-free ZnO homoepitaxial films by 3d transition-metal doping”, Appl. Phys. Lett. 108, 021904 (2016).

11. T. Yamazaki, K. Shigematsu, Y. Hirose, S. Nakao, I. Harayama, D. Sekiba, T. Hasegawa, Amorphous ZnO_xN_y thin films with high electron Hall mobility exceeding 200 $cm^2 V^{-1} s^{-1}$, Appl. Phys. Lett., 109, 262101 (2016).

12. I. Harayama, K. Nagashima, Y. Hirose, H. Matsuzaki, D. Sekiba, Development of dE-E telescope ERDA with 40 MeV $^{35}Cl^{7+}$ beam in MALT in the University of Tokyo optimized for analysis of

metal oxynitride thin films, Nuclear Instruments and Methods in Physics Research Section B: Beam Interactions with Materials and Atoms, Volume 384 (2016) 61-67.

13. T. Onozuka, A. Chikamatsu, T. Katayama, Y. Hirose, I. Harayama, D. Sekiba, E. Ikenaga, M. Minohara, H. Kumigashira, T. Hasegawa, Reversible resistance modulation induced by fluorine substitution in perovskitenickelate $NdNiO_2$ thin films, ACS Appl. Mater. Interfaces, 9, 10882-10887 (2017).

14. K. Kawahara, A. Chikamatsu*, T. Katayama, T. Onozuka, D. Ogawa, K.Morikawa, E. Ikenaga, Y. Hirose, I. Harayama, D. Sekiba, T. Fukumura, T. Hasegawa, Topotactic fluorination of perovskite strontium ruthenate thin films using polyvinylidene fluoride CrystEngComm, 19 (2017) 313-317.

15. D. Sekiba, K. Chito, I. Harayama, Y. Watahiki, S. Ishii, K. Ozeki, Installation of high-resolution ERDA in UTTAC at the University of Tukuba: Determination of the energy resolution and the detection limit for hydrogen, Nuclear Instruments and Methods in Physics Research Section B: Beam Interactions with Materials and Atoms, Volume 401 (2017) 29-32.

16. Eiji Kita, Kenichi Shibata, Yuji Sasaki, Mikio Kishimoto, and Hideto Yanagihara, Magnetic anisotropy in spherical Fe16N2 core–shell nanoparticles determined by torque measurements, AIP Advaces, 7, 056212 (5 pages) (2017). doi.org/10.1063/1.4974276

17. H. Latiff, M. Kishimoto, S. Sharmin, E. Kita, H. Yanagihara, Effect of Copper Substitution on Fe_3O_4 Particles Prepared via Coprecipitation and Flux Methods, IEEE TransMAG, 53 No. 1 (2017) 9400104 (4pages). DOI: 10.1109/TMAG.2016.2596291

6.2 Reviews and books

1. 笹 公和、入門講座　精密同位体分析「加速器質量分析装置の原理」、日本分析化学会学会誌「ぶんせき」2016 年 6 月号（2016）196-202.

2. S. F. Chichibu, H. Miyake, K. Hiramatsu, and A. Uedono, “Impacts of Dislocations and Point Defects on the Internal Quantum Efficiency of the Near-Band-Edge Emission in AlGaN-Based DUV Light-Emitting Materials”, III-Nitride Ultraviolet Emitters: Technology and Applications, Springer Series in Materials Science **227**, 115-136 (2016). [10.1007/978-3-319-24100-5_5]

6.3 Proceedings

1. S. Ishibashi and A. Uedono, “Computational studies of positron states and annihilation parameters in semiconductors – vacancy-type defects in group-III nitrides –”, J. Phys.: Conf. Ser. **674**, 012020(1-10) (2016). [doi:10.1088/1742-6596/674/1/012020]

6.4 Poster or oral presentations at academic meetings

1. S. Suzuki, “Development of time-of-flight detector for mass measurements of short-lived nuclei with the rare-RI ring", International Symposium on Neutron Star Matter (NSMAT2016), 21-24 November 2016. (Poster)

2. 森口哲朗、”筑波大学 12UD ペレトロンタンデム加速器の廃止措置”、第 29 回タンデム加速器及びその周辺技術の研究会、筑波大学、2016/06/30-07/01.（口頭発表）

3. T.Moriguchi, “Density Distributions of 11Li Deduced from Reaction Cross Section Measurements”, The International Nuclear Physics Conference(INPC)2016, Adelaide Convention Centre, Australia, 2016/09/11-16. (Poster)

4. T.Moriguchi, “Density distribution of 14Be from reaction cross-section measurements”., Nuclear chemistry 2016, Hilton San Antonio Airport, San Antonio, Texas, USA, 2016/12/08-09. (Invited, Oral presentation)

5. 木村創大、“Precision mass measurements of proton-rich nuclei in A～60−80 region with the multireflection time-of-flight mass spectrometer”第 9 回 停止・低速不安定核ビームを用いた核分光研究会（2017 年 3 月、原子力機構）.（口頭発表）

6. S. Suzuki, “Development of Secondary Electron Time Detector for Ion Beams”, International Nuclear Physics Conference (INPC2016), Adelaide Convention Center, Australia, 11-26 September 2016. (Oral presentation)

7. 向井もも、 “Development of low-background gas-counter for the beta spectroscopy at KISS”第9回 停止・低速不安定核ビームを用いた核分光研究会（2017 年 3 月、原子力機構）.（口頭発表）

8. T. MATSUNAKA, K. SASA, T. TAKAHASHI, M. MATSUMURA, K. SUEKI, A. GOTO, T. WATANABE, Y. TUCHIYA, N. HIRANO, M. KURI, M. TAKAHASHI, K. KAZAHAYA, I. MIYAGI AND H. MATSUZAKI, Decrease of iodine isotope ratio observed in crater lake and geothermal area at Zao volcano, Japan, Goldschmidt2016, Pacifico Yokohama, Yokohama, 26 June-1 July, 2016.

9. Y. SATOU, K. SUEKI, K. SASA, I. NAKAI, Y. ABE, Y. IIZAWA, T. ONO, K. ADACHI AND Y. IGARASHI, Overview of the radioactive particles in the Fukushima accident, Goldschmidt2016, Pacifico Yokohama, Yokohama, 26 June-1 July, 2016.

10. M. HONDA, K. SUEKI, R. TOMITA, A. SAKAGUCHI, K. SASA, Analysis for chlorine and iodine in natural samples by SEC coupled with ICP-QQQ, Goldschmidt2016, Pacifico Yokohama, Yokohama, 26 June-1 July, 2016.

11. Kimikazu Sasa, Tsutomu Takahashi, Tetsuya Matsunaka, Masumi Matsumura, Seiji Hosoya, Maki Honda, Keisuke Sueki, Mark Stodola, Mark Sundquist, Isobar separation performance of the Tsukuba 6 MV AMS system, 12th European Conference on Accelerators in Applied Research and Technology (ECAART12) , Jyväskylä, Finland on 3 - 8 July 2016.

12. Seiji Hosoya, Kimikazu Sasa, Tetsuya Matsunaka, Masumi Matsumura, Tsutomu Takahashi, Mark Sundquist, Mark Stodola, Keisuke Sueki, Optimization of ΔE -E detector for ^{41}Ca AMS measurement using PHITS code simulation, 12th European Conference on Accelerators in Applied Research and Technology (ECAART12) , Jyväskylä, Finland on 3 - 8 July 2016.

13. A. Yamazaki, K. Sasa, S. Ishii, M. Kurosawa, S. Tomita, S. Shiki, G. Fujii, M. Ukibe, M. Ohkubo, A. Uedono, E. Kita, Development of the microbeam PIXE system for additive light elements in structural materials, 15th International Conference on Nuclear Microprobe Technology and Applications (ICNMTA) (IMP-CAS Lanzhou, China), 31July－5August, 2016.

14. Kimikazu Sasa, Akiyoshi Yamazaki, Shigeo Tomita, Masanori Kurosawa, Satoshi Ishii, Hiroshi Naramoto, Masao Sataka, Hiroshi Kudo, Eiji Kita, Akira Uedono, Construction of an Ion Beam Analysis Facility for Structural Materials at the University of Tsukuba, 2nd International Symposium for Innovative Measurement and Analysis for Structural Materials (SIP-IMASM2016), AIST Tsukuba Campus, Japan, 27-28 Sep., 2016.

15. A. Yamazaki, K. Sasa, S. Ishii, M. Kurosawa, S. Tomita, S. Shiki, G. Fujii, M. Ukibe, M. Ohkubo, A. Uedono, E. Kita, Present Status of Development of the Ion Microbeam System for Additive Light Elements in Structural Materials at the University of Tsukuba, 2nd International Symposium for Innovative Measurement and Analysis for Structural Materials (SIP-IMASM2016), AIST Tsukuba Campus, Japan, 27-28 Sep., 2016.

16. 松中哲也, 笹公和, 高橋努, 松村万寿美, 末木啓介, 富田涼平, 恩田裕一, 石丸隆, 谷口圭輔, 脇山義史, 松崎浩之「福島の河川と沿岸海洋環境における $^{129}I/^{137}Cs$ 比から推察される放射性のヨウ素とセシウムの挙動」平成 28 年度北関東支部「若手研究者発表会」, 東海, 2016.4.15.

17. 松中哲也、笹公和、高橋努、松村万寿美、末木啓介、富田涼平、恩田裕一、石丸隆、谷口圭輔、脇山義史、松崎浩之, 「福島の土壌圏・水圏における $^{129}I/^{137}Cs$ 分布から推測される放射性ヨウ素と放射性セシウムの挙動 」、第 53 回アイソトープ・放射線研究発表会、2016 年 7 月 6 日(水)～7 月 8 日(金)、東京大学弥生講堂（東京都文京区弥生 1-1-1）

18. 笹 公和, 石井 聰, 大島弘行, 高橋 努, 田島義一, 大和良広, 関場大一郎, 森口哲朗, 左高正雄, 楢本 洋, 工藤 博, 松村万寿美, 山崎明義, 松中哲也, 喜多英治, 上殿明良, 筑波大学タンデム加速器施設 UTTAC の現状（2015 年度）, －稼働を開始した 6 MV タンデム加速器によるイオンビーム利用研究の展望－, 「第 29 回タンデム加速器及びその周辺技術の研究会」, 2016 年 6 月 30 日（木）～7 月 1 日（金）, 筑波大学 大学会館

19. 森口 哲朗, 笹 公和, 大島弘行, 石井 聰, 高橋 努, 田島義一, 大和良広, 関場大一郎, 喜多英治, 上殿明良筑波大学 12UD ペレトロンタンデム加速器の廃止措置, 「第 29 回タンデム加速器及びその周辺技術の研究会」, 2016 年 6 月 30 日（木）～7 月 1 日（金）, 筑波大学 大学会館

20. 山崎 明義, 笹 公和, 石井 聰, 黒澤正紀, 冨田成夫, 上殿明良, 筑波大学 6MV タンデム加速器マイクロビームラインの整備状況, 「第 29 回タンデム加速器及びその周辺技術の研究会」, 2016 年 6 月 30 日（木）～7 月 1 日（金）, 筑波大学 大学会館

21. 松村 万寿美, 笹 公和, 松中哲也, 高橋 努, 細谷青児, 末木啓介, 筑波大学 6MV タンデム加速器による I-129 測定の性能評価－TSUKUBA_I-129 STD 作製に向けて－, 「第 29 回タンデム加速器及びその周辺技術の研究会」, 2016 年 6 月 30 日（木）～7 月 1 日（金）, 筑波大学 大学会館

22. 細谷 青児, 笹 公和, 高橋 努, 松中哲也, 松村万寿美, 末木啓介, ^{36}Cl-AMS 測定に向けた, 妨害核種 ^{36}S 除去の検討, 「第 29 回タンデム加速器及びその周辺技術の研究会」, 2016 年 6 月 30 日（木）～7 月 1 日（金）, 筑波大学 大学会館

23. 松中 哲也, 笹 公和, 細谷青児, 高橋 努, 松村万寿美, 末木啓介, ガスイオン源を用いた迅速 14C 測定法の検討, 「第 29 回タンデム加速器及びその周辺技術の研究会」, 2016 年 6 月 30 日（木）～7 月 1 日（金）, 筑波大学 大学会館

24. 椎名 陽子, 木下 亮, 松田 誠, 今井 誠, 川面 澄, 左高正雄, 笹 公和, 冨田成夫, 高速クラスター照射におけるコンボイ電子収量の標的膜厚依存性, 「第 29 回タンデム加速器及びその周辺技術の研究会」, 2016 年 6 月 30 日（木）～7 月 1 日（金）, 筑波大学 大学会館

25. 笹 公和, 石井 聰, 大島 弘行, 高橋 努, 田島 義一, 大和 良広, 関場 大一郎, 森口 哲朗, 喜多 英治, 上殿 明良, 筑波大学複合タンデム加速器施設の現状報告, 第 13 回日本加速器学会年会, 2016 年 8 月 8 日(月) ～ 10 日(水), 幕張メッセ国際会議場

26. 笹 公和, Stodola Mark, Sundquist Mark, 複合イオンビーム利用研究の展開を目指した 6 MV タンデム型静電加速器の開発, 第 13 回日本加速器学会年会, 2016 年 8 月 8 日(月) ～ 10 日(水), 幕張メッセ国際会議場

27. 黒尾奈未, 笹公和, 細谷青児, 松中哲也, 6MV タンデム型静電加速器におけるビーム輸送設定条件の検討, 第 13 回日本加速器学会年会, 2016 年 8 月 8 日(月) ～ 10 日(水), 幕張メッセ国際会議場

28. 椎名陽子, 木下亮, 松田誠, 今井誠, 川面澄, 左高正雄, 笹公和, 冨田成夫, 炭素薄膜への高速クラスターイオン照射における 0 度電子分光 I, 日本物理学会 2016 年秋季大会, 2016 年 9 月 13-16 日, 金沢大学

29. 佐藤志彦, 末木啓介, 笹公和, 福島第一原発北西部における放射性物質と放射性粒子の関係, 2016 日本放射化学会年会・第 60 回放射化学討論会, 2016 年 9 月 10 日～12 日, 新潟大学五十嵐キャンパス

30. 松中 哲也, 笹 公和, 細谷 青児, 高橋 努, 松村 万寿美, 末木 啓介, CO_2 ガスイオン源を用いた迅速 ^{14}C-AMS の開発, 2016 日本放射化学会年会・第 60 回放射化学討論会, 2016 年 9 月 10 日（土）～12 日（月）, 新潟大学五十嵐キャンパス

31. 富田涼平, 松中哲也, 本多真紀, 佐藤志彦, 松村万寿美, 高橋努, 坂口綾, 松崎浩之, 笹公和, 末木啓介, 福島原発事故以降の 河川 における溶存態と底質土のセシウム同位体比変化, 2016 日本放射化学会年会・第 60 回放射化学討論会, 2016 年 9 月 10 日～12 日, 新潟大学五十嵐キャンパス

32. 黒澤正紀, 笹公和, 石井聰, 対馬花崗岩の流体包有物中のチタン濃度, 日本鉱物科学会年会, 2016 年 9 月 23 日～25 日, 金沢大学

33. 池端 慶，服部浩一，黒澤 正紀，小室光世，笹 公和，石井 聰，三好陽子，島田和彦，戸塚修平，石橋純一郎，中部沖縄トラフ伊平屋北海丘熱水域に産する黄鉄鉱の 微 量元素組成の特徴，日本火山学会 2016 年度秋季大会学術講演会，2016 年 10 月 13 日～15 日，富士吉田市民会館富士山ホール（山梨県富士吉田市）

34. 笹 公和，左高 正雄，楢本 洋，工藤 博，低 LET 加速粒子による放射線耐性試験のための宇宙用素子照射装置の開発，日本原子力学会 2016 年秋の大会，2016 年 9 月 7 日～9 日，福岡県久留米シティプラザ

35. 細谷 青児，笹 公和，高橋 努，松中 哲也，松村 宏，松村 万寿美，末木 啓介，難測定核種 ^{41}Ca の加速器質量分析法による超高感度測定 ，日本原子力学会 2016 年秋の大会，2016 年 9 月 7 日～9 日，福岡県久留米シティプラザ

36. 末木 啓介，佐藤 志彦，笹 公和，福島第一原発から北西地域における放射性核種と放射性粒子，日本放射線安全管理学会 第 15 回学術大会，2016 年 11 月 30 日～12 月 2 日，岡山大学

37. 松村万寿美，笹 公和，松中 哲也，末木 啓介，高橋 努，渡邊 雅也，松崎 浩之，福島第一原子力発電所事故前後における降水中のヨウ素 129 濃度の推移，日本放射線安全管理学会第 15 回学術大会，2016 年 11 月 30 日～12 月 2 日，岡山大学

38. 村上道夫，韮澤貴夫，吉兼隆生，末木啓介，笹公和，芳村圭，仮想的な原子力発電所事故における飲食物由来の被ばく量と希釈率の推定，2016 年度第 29 回日本リスク研究学会年次大会，2016 年 11 月 25～27 日，大分市　ホルトホール大分

39. 笹 公和，宇宙線生成核種の超高感度検出を実現する 6 MV タンデム加速器質量分析装置，第 2 回 TIA 光・量子計測シンポジウム-　光・量子が繋ぐ TIA 計測連携　~新しい科学と産業の創製をめざして~，2016 年 11 月 10 日，つくば国際会議場 2F 中会議室　201B 202

40. 山崎明義，笹公和，石井聰，黒澤正紀，冨田成夫，椎名陽子，楢本洋，左高正雄，工藤博，志岐成友，藤井剛，浮辺雅宏，大久保雅隆，上殿明良，喜多英治，筑波大学 6MV タンデム加速器イオンマイクロビームシステムの整備状況，第 2 回 TIA 光・量子計測シンポジウム -　光・量子が繋ぐ TIA 計測連携　~新しい科学と産業の創製をめざして~，2016 年 11 月 10 日，つくば国際会議場 2F 中会議室　201B 202　（ポスター）

41. 中本尚樹，新田紀子，土田秀次，冨田成夫，笹　公和，平田浩一，平野貴美，山田圭介，千葉敦也，斎藤勇一，鳴海一雅，高速 C_{60} フラーレンイオンビーム照射による GaSb 表面改質，高知工科大学 総合研究所ナノテク研シンポジウム 2016，2016 年 11 月 12 日，高知工科大学 永国寺キャンパス

42. Y. Shiina, R. Kinoshita, M. Matsuda, M. Imai, K. Kawatsura, M. Sataka, K. Sasa1, and S. Tomita, Target thickness dependence of convoy electron yield observed in fast cluster ion bombardment on thin foils, 第17回「イオンビームによる表面・界面」特別研究会，2016年１２月３日~４日 京都府立大学

43. 笹　公和,「最新の加速器質量分析装置が拓く多核種 AMS による高精度年代測定の展望」(招待講演), 「高精度年代測定の地平–AMS と樹木年輪–」第 19 回日本 AMS シンポジウム（JAMS-19）・2016 年度「樹木年輪」研究会 共同開催シンポジウム、2016 年 12 月 17－18 日，国立歴史民俗博物館　講堂

44. 細谷青児，笹公和，高橋努，松中哲也，松村万寿美，末木啓介，41Ca-AMS の実用化に向けた技術開発と測定評価，第 19 回日本 AMS シンポジウム（JAMS-19），2016 年 12 月 17－18 日，国立歴史民俗博物館　講堂

45. 本多真紀，高久雄一郎，大野剛，角田伸一郎，鹿籠康行，松崎浩之，坂口綾，笹公和，高橋努，松中哲也，松村万寿美，細谷青児，末木啓介，AMS とコリジョン/リアクションセル ICP-MS による環境試料中の ^{129}I の分析, 第 19 回日本 AMS シンポジウム（JAMS-19），2016 年 12 月 17－18 日，国立歴史民俗博物館　講堂

46. 稲葉留衣，坂口綾，野村知哉，山川茜，山野博哉，佐々木圭一，渡邊剛，Peter Steier，本多真紀，笹公和，松中哲也，細谷青児，高橋努，松村万寿美，末木啓介，サンゴコア分析による長寿命人工放射性核種の日本海導入履歴復元の試み, 第 19 回日本 AMS シンポジウム（JAMS-19），2016 年 12 月 17－18 日，国立歴史民俗博物館　講堂

47. 松村万寿美，笹公和，松中哲也，高橋努，細谷青児，末木啓介，筑波大学におけるヨウ素 129 標準試料作製計画，第 19 回日本 AMS シンポジウム（JAMS-19），2016 年 12 月 17－18 日，国立歴史民俗博物館　講堂

48. Hongtao Shen, Jiang Shan, Kimikazu Sasa, Masumi Matsumura, Tetsuya Matsunaka, Tsutomu Takahashi, Seiji Hosoya, Keisuke Sueki, Study on ^{36}Cl-AMS for Exposure Age Dating of Guangxi Tiankeng, 第 19 回日本 AMS シンポジウム（JAMS-19）, 2016 年 12 月 17－18 日，国立歴史民俗博物館　講堂

49. 松中哲也，笹公和，高橋努，細谷青児，松村万寿美，末木啓介，佐藤志彦，東日本原子力施設周辺の年輪内における 1960 年以降の炭素 14 濃度変動，第 19 回日本 AMS シンポジウム（JAMS-19），2016 年 12 月 17－18 日，国立歴史民俗博物館　講堂

50. 末木啓介，松尾一樹，太田裕貴，本多真紀，坂口綾，笹公和，松中哲也，高橋努，細谷青児, 松村万寿美, 佐藤志彦, 福島事故由来の放射性物質における長寿命核種の AMS 測定,

第 19 回日本 AMS シンポジウム（JAMS-19），2016 年 12 月 17－18 日，国立歴史民俗博物館　講堂

51. 松中 哲也，笹 公和，高橋 努，細谷 青児，松村 万寿美，末木 啓介，佐藤 志彦，東海原子力施設の稼働状況に応答した樹木年輪内の炭素 14 濃度変動，第 18 回「環境放射能」研究会，2017 年 3 月 14～ 3 月 16 日

52. 細谷青児, 笹公和, 松中哲也, 高橋努, 松村万寿美, Hongtao Shen, 末木啓介「長寿命放射性核種 36Cl の加速器質量分析法による超高感度測定」，第 18 回「環境放射能」研究会, つくば, 2017.3.14-16.

53. 笹 公和，加速器質量分析法による長寿命放射性核種の超高感度検出技術の進展とその応用（招待講演），第 18 回「環境放射能」研究会, つくば, 2017.3.14-16.

54. 新田紀子, 中本尚樹, 土田秀次, 冨田成夫, 笹　公和，平田浩一, 平野貴美, 山田圭介, 千葉敦也, 斎藤勇一, 鳴海一雅，高速 C_{60} フラーレンイオンビーム照射による GaSb への照射効果，日本金属学会、2017 年春期(第 160 回)講演大会，首都大学東京南大沢キャンパス，2017 年 3 月 15 日(水)～3 月 17 日(金)

55. 細谷青児, 笹公和, 高橋努, 松中哲也, 松村万寿美, Hongtao Shen, 末木啓介, 加速器質量分析法における ^{10}Be, ^{36}Cl の高感度測定のための同重体分離手法の検討とその測定性能評価，日本原子力学会 2017 年春の年会，東海大学湘南キャンパス, 2017. 3. 27-29.

56. 笹 公和，山崎明義，石井 聰，黒澤正紀，冨田成夫，左高正雄，楢本 洋，工藤 博，構造材料計測用イオンビーム分析装置の開発，日本原子力学会 2017 年春の年会，東海大学湘南キャンパス, 2017. 3. 27-29.

57. Hawa Latiff, M. Kishimoto, S. Sharmin, H. Yanagihara, E. Kita
"Synthesis and physical properties of single phase cubic and tetragonal $CuFe_2O_4$ particles", International Conference on Fine Particle Magnetism(ICFPM) 2016, Washington DC, USA, June 13-17, 2016

58. E. Kita, Y. Sasaki, M. Kishimoto and H. Yanagihara,
"Magnetic Anisotropy in spherical Fe16N2 core-shell nanoparticles determined by torque measurements", 61st Annual Conference on Magnetism and Magnetic Materials (MMM2016), New Orleans, Louisiana, October 31 – November 4, 2016,

6.5 UTTAC seminars

2016

May 26 Measurement of 1st, 2nd and 3rd azimuthal anisotropy in Cu+Au collisions, *Hiroshi Nakagomi (University of Tsukuba)*

2017

Jan 13 Direct photon - hadron azimuthal correlation in 7 TeV pp collisions at LHC-ALICE experiment, *Kyoichiro Ito (University of Tsukuba)*

High pT hadron measurement with SVTX in 200 GeV 3He+Au collisions at RHIC-PHENIX experiment, *Sakiko Kudo (University of Tsukuba)*

Pi0 measurement with EMcal in 5.02 TeV pp collisions at LHC-ALICE experiment, *Ryohei Koyama (University of Tsukuba)*

Multiplicity dependence of long-range azimuthal correlation in 510 GeV pp collisions at RHIC-PHENIX experiment, *Yusuke Fukuda (University of Tsukuba)*

Performance of EMcal for pi0 measurement in 5.02 TeV Pb+Pb collisions at LHC-ALICE experiment, *Kazunari Matsunaga (University of Tsukuba)*

Jet measurement with EMcal in 5.02 TeV Pb+Pb collisions at LHC-ALICE experiment, Byung Chul Kim *(University of Tsukuba)*

Jan 16 New aspects of nuclear physics probed by reaction cross sections, *Mitsunori Fukuda (Osaka University)*

Mar 16 Lecture on high energy ion microbeams, *Dr. Geoffrey Grime (Senior Researcher, The Surrey Ion Beam Centre, University of Surrey, United Kingdom)*

6.6 Symposium

The 29th Community Meeting on the Electrostatic Particle Accelerators and Their Related Technologies

30 Jun – 1 July 2016

University Hall, University of Tsukuba

1. Welcome address : *Akira Uedono (University of Tsukuba)*
2. Welcome address : *Kimikazu Sasa (University of Tsukuba)*
3. Status Report of the Tandem Accelerator Facility at the University of Tsukuba (FY 2015) - Future Prospects of Ion Beam Applications on the Newly Started 6 MV Tandem Accelerator - : *Kimikazu Sasa (University of Tsukuba)*
4. Status report of the NIES-TERRA : *Toshiyuki Kobayashi (Center for Environmental Measurement and Analysis, NIES)*
5. Current status of MALT, The University of Tokyo : *Chuichiro Nakano (The University Museum, The University of Tokyo)*
6. Current status of Compact AMS at UMUT (2015-16) : *Hiromasa Ozaki (The University Museum, The University of Tokyo)*
7. Current status of the Single Stage AMS at AORI, The University of Tokyo : *Takahiro Aze (Atmosphere and Ocean Research Institute, The University of Tokyo)*
8. Induction microtorn for semi-relativistic large cluster ions: *Ken Takayama (High Energy Accelerator Research Organization)*
9. Present status of the tandem accelerator facility at Kyushu University-- Decommissioning of Hakozaki facility and construction of Ito facility -- : *Tetsuo Noro (Faculty of Science, Kyushu University)*
10. Decommissioning of the 12UD Pelletron tandem accelerator : *Tetsuaki Moriguchi (University of Tsukuba)*
11. A report of measurement of neutron emission in electrostatic accelerator facilities : *Kazuyoshi Masumoto (High Energy Accelerator Research Organization)*
12. Present status of the tandem accelerator at the JAEA-AMS-TONO (2015) : *Natsuko Fujiata (Tono Geoscience Center, JAEA)*
13. Present status of JAEA-Tokai tandem accelerator facility : *Kenichi Kutsukake (Tandem Accelerator Section, Department of Research Reactor and Tandem Accelerator, Nuclear Science Research Institute, Japan Atomic Energy Agency)*
14. Current status of the compact-AMS system at Paleo Labo Co., Ltd.(2016) : *Shigeru Itoh (AMS Dating Facility, Paleo Labo Co., Ltd.)*
15. Progress report of NIRS electrostatic accelerator facility (PASTA & SPICE) : *Masakazu Oikawa (National Institute of Radiological Science, National Institute for Quantum and Radiological Science and Technology)*
16. Present Conditions of Tandem Accelerator in Kobe University 2016 : *Akira Taniike (Graduate School of Maritime Sciences, Accelerator Division of Center for Supports to Research and Education Activities,*

Kobe University)

17. Present Status of Tohoku Microbeam System : *Shigeo Matsuyama (Tohoku University)*
18. Status of Tohoku University Dynamitoron Accelerator : *Misako Miwa (Tohoku University)*
19. Present status of YU-AMS 2015-2016 : *Toru Moriya (Center for Accelerator Mass Spectrometry, Yamagata Univ.)*
20. Construction and trial operation of the Ion Microbeam System on the 6 MV Tandem Accelerator at the University of Tsukuba : *Akiyoshi Yamazaki (Faculty of Pure and Applied Sciences, University of Tsukuba)*
21. Current status of tandem accelerator ion analyzing equipment at NIFS : *Akimitsu Nishizawa (Pesco Co. Ltd.)*
22. Present status and application studies with AMS ^{14}C system at Nagoya University (2016) : *Toshio Nakamura (Institute for Space-Earth Environmental Research, Nagoya University)*
23. Progress report of tandem accelerator in NWU : *Jyunya Karimata (Research Cooperation Division, Nara Women's University)*
24. Status report of the accelerator facility at the Department of Nuclear Engineering, Kyoto University (FY 2015) : *Yoshitaka Sasaki (Department of Nuclear Engineering, Kyoto University)*
25. Current status of the accelerator facility at The Wakasa Wan Energy Research Center : *Satoshi Hatori (The Wakasa Wan Energy Research Center)*
26. Development of the electric charge conversion model negative ion source : *Hiroaki Yamada (The Wakasa Wan Energy Research Center)*
27. SF_6 gas recovery system that adds a Low-temperature adsorption : *Tetsuya Odagiri (The Wakasa Wan Energy Research Center)*
28. Development of a C_{60} fullerene ion source using sublimation and electron-capture ionization : *Koshiro Nakamura (Tokyo Institute of Technology)*
29. Startup Status of the 1.7MV Tandem Pelletron Accelerator at Tokyo City University : *Naoto Hagura (Atomic Energy Research Laboratory / Tokyo City University)*
30. Present status of the Neutron exposure accelerator for biological effects : *Noriyoshi Suya (National Institutesfor Quantum and Radiological Science and Technology NIRS)*
31. Construction of an AMS beam line at the Kyushu University tandem accelerator facility : *Toshiya Hataguchi (Faculty of Sciences, Kyushu University)*
32. Conditioning of the 5-MV Electrostatic Accelerator in the JAEA-AMS-TONO : *Akihiro. Matsubara (PESCO CO., Ltd.)*
33. Current status of CAMS system at NIES : *Yumi Osonoi (Center for Global Environmental Research, NIES)*
34. Current status of electrostatic accelerators at TIARA : *Yoshimi Hirano (Takasaki Advanced Radiation Research Institute, QST)*
35. Current Intensification of Fullerene Ion Beam : *Atsuya Chiba (Takasaki Advanced Radiation Research Institute, QST)*
36. The performance evaluation of the measurement of iodine-129 by the 6 MV Tandem Accelerator at the University of Tsukuba‐Looking forward to preparation of TSUKUBA_I-129

standards for AMS－ : *Masumi Matsumura (Accelerator Mass Spectrometry Group , University of Tsukuba)*

37. Study of interference nuclide ^{36}S removal for ^{36}Cl-AMS measurement : *Seiji Hosoya (Accelerator Mass Spectrometry Group , University of Tsukuba)*
38. Development of rapid ^{14}C-AMS using CO_2 gas ion source : *Tetsuya Matsunaka (AMS Group, University of Tsukuba)*
39. Target thickness dependence of convoy electron yield observed in fast cluster ion bombardment on thin foils : *Yoko Shiina (University of Tsukuba)*
40. Concluding remarks : *Tetsuaki Moriguchi (University of Tsukuba)*

7.

THESES

Doctor theses

Isao Harayama	Development of an advanced ERDA and PIXE system for analyses of functional films

Master theses

Toaki Kakizaki	Free volume evaluation of epoxy resin for CFRP by positron annihilation method
Shunya Sakai	Construction of light irradiation system by positron annihilation method and characterization of GaN by light irradiation
Takahiro Tamura	Development of dual MCP coincidence system in high-resolution ERDA for sensitive hydrogen analysis
Eri Noguchi	Observation of oxygen vacancies and Ti interstitials on the surface of Rutile-TiO_2(110) by high-resolution RBS

Undergraduate theses

Junichi Kikuda	Observation of He^{2+} channeling for Pd(110) by RBS
Yuki Sugisawa	Development of strip-SSD for high-sensitivity ERDA
Kaoru Sako	Free volume evaluation of resin for CFRP by positron annihilation
Shusuke Hashimoto	Defect evaluation of ion implanted Ge by positron annihilation
Yuya Asai	Development of Time Dependent Doppler Spreading Measurement System and Defect Evaluation of GaN on Si
Rui Inaba	Temporal variation of anthropogenic ^{129}I in the Japan Sea using a coral core sample
Yuki Ota	Quantitative determination of ^{36}Cl from soil near the Fukushima Daiichi Nuclear Power Plant with the use of AMS
Kazuki Matsuo	Characterization of radioactive particles derived from the Fukushima Daiichi Nuclear Power Plant accident
Daiki Kamioka	Developments of time-of-flight detector using secondary electrons from thin foil

8.

LIST OF PERSONNEL

Tandem Accelerator Complex

A. Uedono	Director, Professor
K. Sasa	Associate Professor
D. Sekiba	Lecturer
T. Moriguchi	Assistant Professor
H. Oshima	Electrical Engineer
Y. Tajima	Mechanical Engineer
S. Ishii	Mechanical Engineer
T. Takahashi	Electrical Engineer
Y. Yamato	Electrical Engineer
M. Sataka	Research Fellow
M. Matsumura	Research Supporter
M. Ohyama	Administrative Staff (2016.4.1–2016.6.30)
S. Kuramochi	Administrative Staff (2016.7.1–2017.3.31)
M. Satoh	Administrative Staff
I. Takada	Administrative Staff

Research Members[1]

Division of Physics

A. Ozawa	T. Matsunaka	T. Moriguchi	K. Sasa
S. Suzuki	H. Shen		

Division of Applied Physics

E. Kita	D. Sekiba	S. Sharmin	S. Tomita
A. Uedono	H. Yanagihara		

Division of Geoscience

M. Kurosawa

Division of Chemistry

K. Sueki	A. Sakaguchi

Division of Information and Systems

T. Kameda

[1] The “research members” include the authors and coauthors within 5 years back from this fiscal year, as well as the members of research projects running at UTTAC.

Staff of Open Advanced Facilities Initiative

H. Kudo H. Naramoto M. Sataka

K. Awazu (National Institute of Advanced Industrial Science and Technology [AIST])

S. Aoki (Comprehensive Research Organization for Science and Society [CROSS])

Staff of Joint Research Projects with Other Organizations

A. Yamazaki (Cross-ministerial Strategic Innovation Promotion Program [SIP])[2]

Y. Watahiki (Nanotech Career-up Alliance [CuPAL])

Graduate students

Graduate School of Pure and Applied Sciences

Graduate School of Life and Environmental Sciences

M. Ahmed	F. Arai	S. Fukuoka	I. Harayama
Y. Shiina	S. Kimura	M. Mukai	M. Honda
Y. Liu	R. Patel	H. Latiff	Y. Hisamatsu
M. Matsumoto	E. Noguchi	S. Nomoto	T. Tamura
R. Tomita	T. Tainosho	M. Amano	S. Hosoya
T. Kakizaki	S. Sakai	N. Yamamoto	N. Kuroo
T. Eguchi	Y. Hosoi	H. Onoda	K. Tsujita

Undergraduates

D. Kamioka	K. Sako	K.Nakayama	S. Hashimoto
J. Kikuda	R. Inaba	Y. Ota	K. Hattori
K. Matsuo	Y. Sugisawa	K. Oya	A. Nagata
A. Yasuda	H. Watanabe		

Scientific Guests and Fellows

Y. Tosaki	National Institute of Advanced Industrial Science and Technology (AIST)
H. Matsumura	High Energy Accelerator Research Organization (KEK)
N. Kinoshita	SHIMIZU Corporation
K. Hirata	National Institute of Advanced Industrial Science and Technology (AIST)
T. Omori	The University of Tokyo
R. Katayama	The University of Tokyo
K. Ozeki	Ibaraki University

[2] Also, a staff of *Open Advanced Facilities Initiative*